PROBLEMS IN ANALYSIS AND DESIGN OF SWITCHING REGULATORS

I. POLE PLACEMENT TECHNIQUE FOR DC-TO-DC SWITCHING REGULATORS

II. TRANSFORMER MODELLING

III. CROSS-REGULATION OF THE TWO-OUTPUT ĆUK CONVERTER

Thesis by

Shi-Ping Hsu

In Partial Fulfillment of the Requirements

for the Degree of

Doctor of Philosophy

California Institute of Technology

Pasadena, California

1980

(Submitted September 13, 1979)

獻給我的父母

徐昭懷先生
夫人

Dedicated to my parents

CHU-HWA and TSOU-WHAI HSU

ACKNOWLEDGMENTS

I wish to express my deepest gratitude to my advisors, Professor R. D. Middlebrook and Professor S. Ćuk for their continuing encouragement and guidance throughout the course of this research work. I also appreciate the entire Power Electronics Group who made Caltech a very pleasant and rewarding place to work.

Financial support by way of a Teaching Assistantship from the California Institute of Technology, a Research Assistantship sponsored by the International Business Machines Corporation and by the Naval Ocean Systems Center, and the Li-Ming Fellowship, are gratefully acknowledged.

Special thanks are extended to Mrs. Michelle Schroeder for typing part of the thesis.

Most important, I thank my wife Jin-Chèn, who has been a constant source of love and attention. Without her understanding and patience, this work would not have been possible.

ABSTRACT

Power Electronics is an interdisciplinary field which combines three of the major disciplines of electrical engineering--control, power and electronics. The three topics in this thesis arise from problems encountered in these fields.

Part I is an application of modern control theory to the design of any dc-to-dc switching regulator. By feeding back all the state variables in a regulator, the system closed-loop poles can be placed anywhere desired on the s-plane. This is in contrast to the conventional single-loop design where the closed-loop poles are constrained on the root loci between the open loop poles and zeros. With this total-state feedback technique, the stability margins and transient responses of a switching regulator can be shaped as desired.

Part II is a study of transformer modelling, which is important in the design of power processing circuits. The simple π-model is used to model two-winding, three-winding and under some special cases, four-winding transformers. In the past, the parameters in the model were expressed in terms of the coupled-inductor coefficients L_{11}, M_{12}, L_{22} etc., while in this thesis, they are expressed in terms of the permeances which link the model directly to the physical layout of the windings. With this representation, the physical insight of the transformer is explicitly exposed in the model.

Part III analyzes the cross-regulation problem of a two-output Ćuk converter. The unique effect of the unequal discharge of the coupling capacitances on the cross-regulation of a Ćuk converter

is first discussed. It is pointed out that this effect can be made arbitrarily small by increasing the values of the capacitances. The parasitic effects such as leakage inductances, winding resistances and diode offset voltages are then included in the more general analysis. Quantitative results, which are useful in control and improvement of the cross-regulation, are given at the end.

TABLE OF CONTENTS

INTRODUCTION

As world energy becomes increasingly scarce and expensive, the efficiency of all the power processing equipments in the electrical and electronic industries becomes more and more important. For example, a better designed motor drive announced by Exxon this year is claimed to save the equivalent of a million barrels of oil a day in the U.S. Although efficiency alone is worthy of attracting more attention to better design of power processing equipments, volume, weight, and cost of such equipments deserve even more improvement. This is because advancement of very large scale integrated circuit technology, which drastically reduces the size and the cost of signal processing electronics, leaves the power processing electronics relatively bulky and expensive. Leading manufacturers of motor drives, computers, communications systems, and electronic instruments have been investing more and more heavily in research and development of power processing equipments, and a new field -- Power Electronics -- has just emerged from limbo.

Power Electronics is an interdisciplinary field which combines three of the major disciplines of electrical engineering -- control, power, and electronics. In the control part, both continuous and discrete analysis methods of linear system theory and modern control theory are being adapted to analyze the dynamics of power processing systems. In the power part, static and rotating equipments are being restudied, and emphasis has been on the better design of magnetics and

development of new magnetic materials. In the electronics part, new devices such as thyristors, power transistors, VMOS, low ESR capacitors and new control chips are being developed and applied to innovative circuit topologies and feedback schemes. It is only recently that some efforts have been made to integrate the state-of-the-art technologies from these three disciplines to improve power processing equipments.

The three parts in this thesis correspond to the three disciplines mentioned above. Part I is an application of modern control theory to the design of any dc-to-dc converter. In recent years, a method of analysis, called the state-space averaging method, has been developed to describe the dynamics of the power stage of any dc-to-dc converter, which is a nonlinear system, by a set of linearized differential equations or by a linearized equivalent circuit model [1,2]. The beauty of this analysis method is that all the familiar results from linear system theory and control theory can be applied to power processing circuits. Many applications of this linearized equivalent circuit model have been demonstrated successfully in the design of conventional voltage feedback switching regulators [3-10]. However, the feedback control is not limited to the single-loop scheme: substantial advantages can be effected by two-state feedback, such as the current-programmed mode in which both the transistor current and the output voltage are sensed and fed back to control the duty ratio of the main power transistor [11,12]. This idea of two-state feedback can be further generalized to multi-state

feedback. In fact, from mathematical system theory, it is known that the closed-loop poles of a linear controllable system can be placed anywhere desired on the s-plane, provided that the feedback signal is a linear combination of all the state variables in the system [13]. When this technique is applied to switching regulators, the design iterations on the feedback network can be avoided. The closed-loop pole locations are first determined from the specified stability margins and the transient responses, and the feedback gains from each state variable can then be calculated. Detailed discussion of this technique is presented in Part I.

Part II is a study of the transformer modelling. Transformers and coupled-inductors are among the most important elements in a power processing circuit because they are responsible for energy storage, energy transfer and power split. Unfortunately they are probably the least controllable components in the circuit. The non-idealities of a power transformer usually have a strong effect on the performance of the converter and give high stress to the other components in the circuit. But on the other hand, the leakage inductances of the coupled inductor in a Ćuk converter can be used to steer the switching ripples away from the output and/or input current [14]. Thus, a good transformer model is extremely important. It should be not only simple and accurate enough but also physically interpretable. The model is to bear a close relationship to the physical layout of the transformer windings so that the effect of different winding techniques on the leakage inductances can be easily

understood. For many years, transformers and coupled-inductors have been modelled by the popular π-model, which consists of one ideal transformer with effective turns ratio in the center, one magnetizing inductance in parallel with it, and one leakage inductance on each winding. This model is the most convenient one to use, but it is noticed that the π-model is under-determined for two-winding transformers, uniquely-determined for three-winding transformers, and over-determined for transformers of more than three windings. In other words, the π-model can be used in two-winding and three-winding transformers, but only under special cases can it be used in four-winding transformers. A general model has to be used when the π-model is not applicable. In the past, the elements of the π-model have been expressed in terms of the coupled-inductor coefficients L_{11}, M_{12}, L_{22}, etc., but in Part II, they are expressed in terms of the permeances associated with each magnetic flux path in the field map of the transformer. It is found that more physical insight into the transformer properties can be obtained with use of the permeances. For example, it is observed that each leakage inductance on a three-winding transformer is not only a function of the physical tightness of the winding itself to the core, but also the relative layout of the other two windings with respect to the first one. Some applications of the transformer models, such as the effect of the air gap on the coupling coefficient of a two-winding transformer and the effect of the leakage inductances on the zero ripple Ćuk converter, are also presented.

The third part of the thesis is on the cross-regulation of a two-output Ćuk converter. In switching dc-to-dc converters, it is quite common to provide multiple outputs from one converter by inserting a multiple-winding transformer in the switching part of the converter to split the energy flow to several secondary windings. The voltage of the major output is sensed and fed back to control the duty ratio of the main power transistor. The voltages of the other outputs are ideally fixed with respect to the major output voltage by the turns ratio of the transformer. But actually they are affected by the changes in the load current of any of the outputs. The variations in the voltages of these "slaved" outputs due to load current changes are called cross-regulations. Since the cross-regulation is basically a second-order effect and is a strong function of the non-idealities in the circuit, it is usually not analyzed quantitatively. Many multiple-output converters are built simply by adjusting the turns ratio of the transformer by a trial and error method. Part III of this thesis is an effort to analyze the cross-regulation of a two-output Ćuk converter. The quantitative effects of the non-idealities in the circuit such as the ESR of the capacitors, winding resistances of the transformer and the inductors, the leakage inductances of the transformer and the diode offset voltages, are presented.

The three topics above are three typical problems encountered in the Power Electronics field. They are not similar in nature because they came from three different disciplines of electrical

engineering, but it takes all of them to make a good design -- an example of the breadth of this new field.

PART I

Pole Placement Technique for Dc-to-dc Switching Regulators

CHAPTER 1

INTRODUCTION

A dc-to-dc switching regulator is a power processing circuit which converts the unregulated dc voltage at the input to a well-regulated dc voltage at the output. The components used in the power stage are low-loss switching transistors, switching diodes, inductors and capacitors. Four common switching dc-to-dc converters are shown in Fig. 1.1. The switch is periodically thrown between positions 1 and 2 to transfer the energy from input to output. For example, in a buck-boost converter, the input energy is transferred and stored in the inductor when the switch is in position 1, and released to the output when the switch is in position 2. Similar energy transfer mechanisms hold for the buck converter and the boost converter. In a Ćuk converter, the energy is transferred through the capacitor C_1 when the switch flips back and forth between position 1 and position 2. The switching period T_s, which is a complete cycle for the switch to go through positions 1 and 2, is typically constant. The fraction of the whole period for which the switch is in position 1 is called the duty ratio d. By modulating the duty ratio according to the error signal derived from the output, the output voltage can be well regulated, as shown in Fig. 1.2. Since the power transistors and power diodes are used as low-loss switches and the switching frequency is typically as high as 20kHz to 200kHz (which means that the energy transferred per cycle is small so that the energy-storage

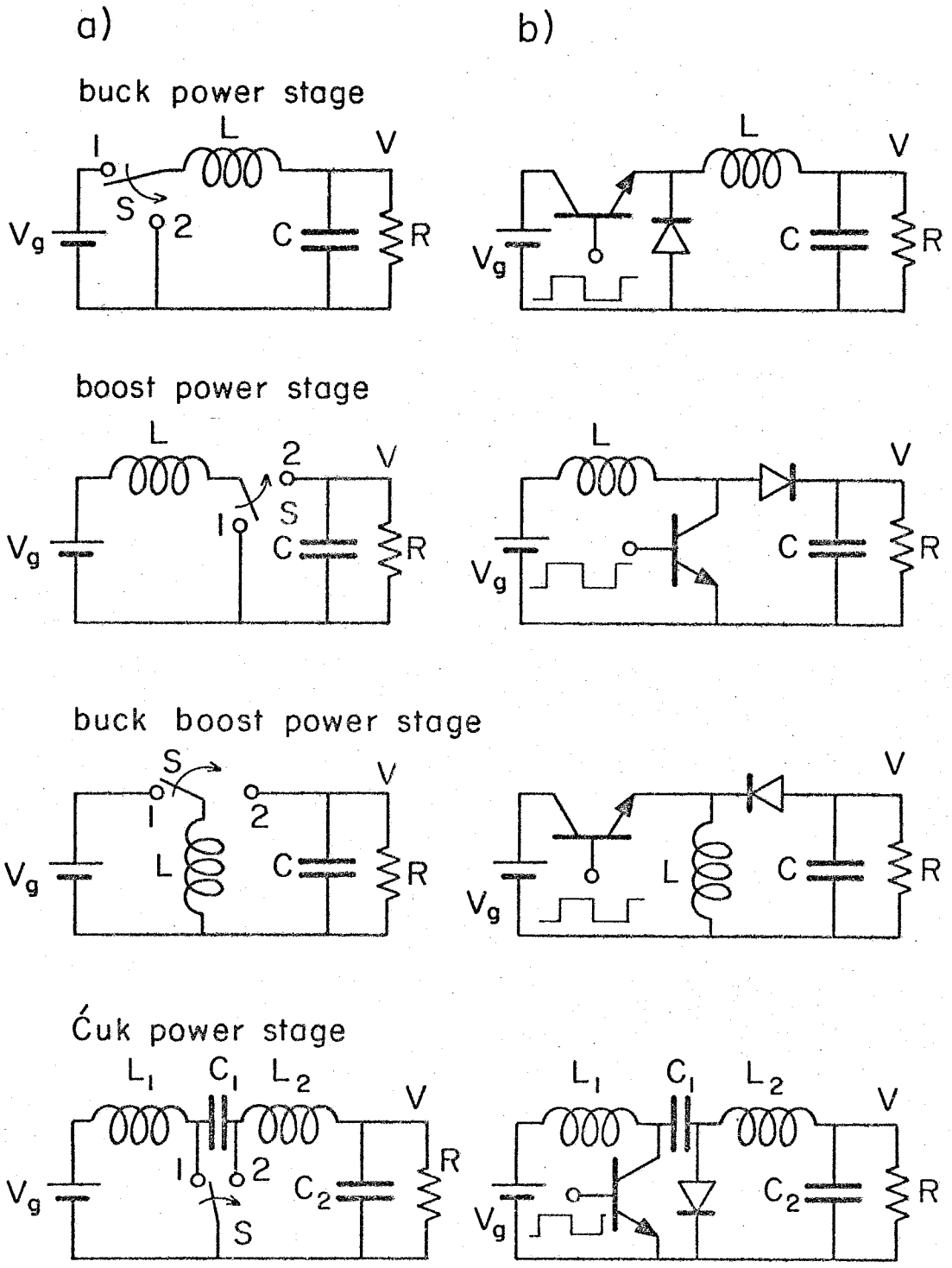

Fig. 1.1 Four common switching dc-to-dc converters:
a) topological configuration independent of switch realization
b) bipolar transistor implementation of the switch S.

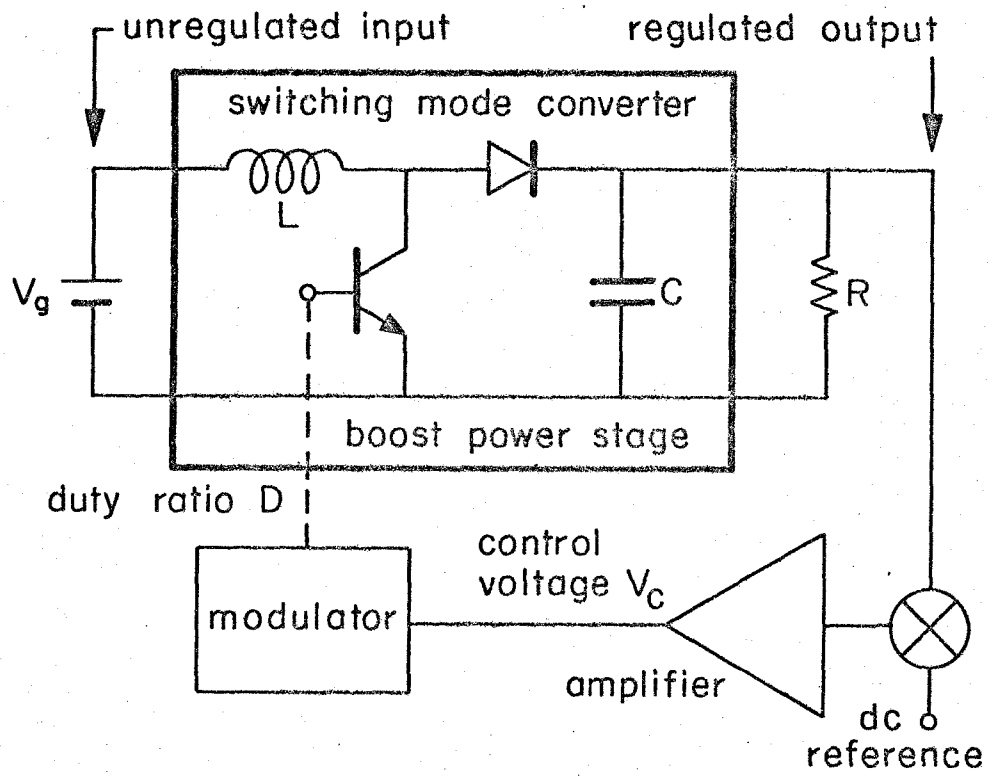

Fig. 1.2 Switching regulator: closed-loop implementation of the switching dc-to-dc converter.

components such as inductors and capacitors can be made small), the total efficiency, volume, and weight of a switching regulator are much superior to those of a conventional linear regulator.

Although a switching regulator has many advantages over a linear regulator, its design and analysis are not trivial problems. This is because a switching mode dc-to-dc converter is a variable piecewise-linear system. It is piecewise-linear because it switches from one linear system when the power switch is ON, to another when the power switch is OFF. It is variable because the switch ON or OFF time is modulated by the feedback signal, and hence is not a constant. The difficulty in analyzing such a complicated system has until recently kept the design of switching regulators in a very primitive state.

In recent years, a method of analysis has been developed which describes the dynamics of a switching converter around its nominal operating point by a set of averaged linear time-invariant equations [1,2]. The success of simplifying the converter into a linear time-invariant system may be appreciated by the fact that the converter can now be modelled by an equivalent circuit and the standard feedback theories such as the Nyquist criterion and the root-locus method can be directly applied. The use of this state-space averaging method and the linear feedback theories has been demonstrated in many applications [3-12].

In this, part I of the thesis, another technique which has been used in modern control theory is applied to the linearized

system of a switching converter. In mathematical system theory, it is known that the closed-loop poles of a linear controllable system can be placed anywhere desired on the s-plane provided that the feedback signal is a linear combination of all the state variables of the system [13]. When this technique is applied to place the closed-loop poles of a switching regulator [15], the stability margins and the transient responses of the regulator can be shaped as desired. Furthermore, if the source voltage and the load current are monitored and fed back together with all the states, better line rejection and load regulation can be obtained.

Although the method is illustrated only for constant frequency duty-ratio-programmed converters in this work, the same analysis also applies with minor modifications to constant ON-time or constant OFF-time converters.

CHAPTER 2

MATHEMATICAL DESCRIPTION OF A TOTAL-STATE FEEDBACK REGULATOR

2.1 Review of state-space averaging method, continuous conduction mode

The state-space averaging method has been developed to describe the small-signal dynamics of any dc-to-dc converter operated in both the continuous and discontinuous conduction mode [1,2]. Since the results of this method are the basis for the total-state feedback scheme, a brief review of the state-space averaging method for the continuous conduction case is presented here.

The state-space averaging technique, outlined in Fig. 2.1, begins with a description of the converter topologies appearing during one cycle of operation. During the interval dT_s, d being the duty ratio, when the switch is closed, the converter can be described by a set of linear, time-invariant differential equations

$$\dot{x} = A_1 x + b_1 v_g \tag{2.1}$$

where x is a state vector of inductor currents and capacitor voltages. Similarly, it can be described by another set of linear differential equations

$$\dot{x} = A_2 x + b_2 v_g \tag{2.2}$$

during the interval $d'T_s \equiv (1-d)T_s$ when the switch is open, as shown in box 2 of Fig. 2.1. These two sets of equations can be combined

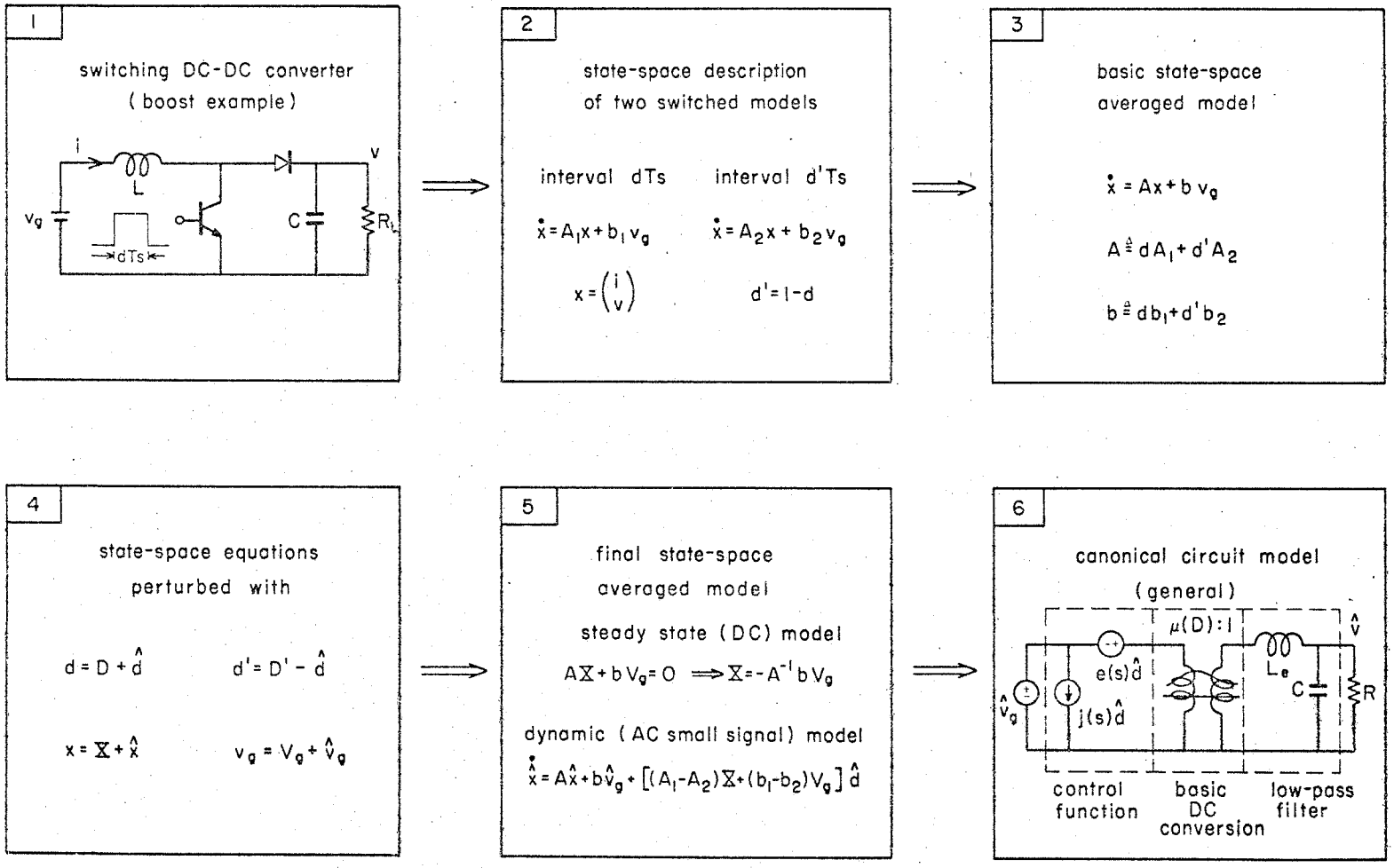

Fig. 2.1 Flowchart of state-space averaging method for modelling dc-to-dc switching converters in the duty-ratio-programmed continuous-conduction mode.

in an average sense to produce a single matrix differential equation, also shown in box 3 of Fig. 2.1

$$\dot{x} = A\,x + b\,v_g \tag{2.3}$$

where $A \equiv dA_1 + d'A_2$

$b \equiv db_1 + d'b_2$

which describes the averaged behavior of the converter, that is, with the switching ripple filtered from the state variables.

Note that the matrices A and b may be duty-ratio dependent, which means that the averaged equation may be nonlinear with respect to duty ratio. Since the ultimate goal is to find an equivalent linear circuit model, the analysis is to be restricted to the linear domain. Hence, as in box 4 of Fig. 2.1, the averaged equation is perturbed around the operating point by substitution into (2.3) of

$$\begin{aligned} d &= D + \hat{d} \\ x &= X + \hat{x} \\ v_g &= V_g + \hat{v}_g \\ R_L &= R + \hat{R} \qquad \text{load resistance variation} \end{aligned} \tag{2.4}$$

where capitalized quantities on the right side of (2.4) refer to steady state values and carets indicate small perturbations. Upon expansion of the result and retention of only first-order perturbations, the final state-space averaged equations are obtained (represented in box 5 of Fig. 2.1):

steady state operating point

$$AX + bV_g = 0 \tag{2.5}$$

ac small-signal

$$\dot{\hat{x}} = A\hat{x} + b\hat{v}_g + c\hat{d} + e\hat{R} \tag{2.6}$$

where

$$A = DA_1 + D'A_2$$

$$b = Db_1 + D'b_2$$

$$c = (A_1 - A_2)X + (b_1 - b_2)V_g$$

$$e = \left(D\frac{\partial A_1}{\partial R_L} + D'\frac{\partial A_2}{\partial R_L}\right)X + \left(D\frac{\partial b_1}{\partial R_L} + D'\frac{\partial b_2}{\partial R_L}\right)V_g$$

The small-signal equivalent circuit model can then be derived from (2.6).

In summary, the small-signal low-frequency behavior of the converter in box 1 of Fig. 2.1, including both input and output properties, has been represented by the canonical model in box 6 of Fig. 2.1 or the linear time-invariant differential eq. (2.6) through the averaging, perturbation, and linearization processes.

2.2 Total-state feedback applied to switching regulators

Now that the system has been reduced to a standard linear time-invariant equation (2.6) around its steady state (2.5), total-state feedback can be applied to the regulator. Equation (2.6) can be transformed into the s-domain:

$$s\hat{x}(s) = A\hat{x}(s) + b\hat{v}_g(s) + c\hat{d}(s) + e\hat{R}(s) \tag{2.7}$$

where $\hat{v}_g$ and $\hat{R}$ are the two independent inputs and $\hat{d}$ is the feedback signal. If the feedback is a linear combination of all the state variables $\hat{x}$, the input voltage variation $\hat{v}_g$, and the load variation $\hat{R}$, that is,

$$\hat{d}(s) = g\hat{x}(s) + f_1(s)\hat{v}_g(s) + f_2(s)\hat{R}(s) \tag{2.8}$$

where $g = (g_1, g_2, \ldots g_n)$ is a row vector of constants, $f_1(s)$ and $f_2(s)$ are the frequency dependent feedback gains from the source voltage and the load, respectively.

then the state equation (2.7) becomes

$$s\hat{x} = (A+cg)\hat{x} + [b+cf_1(s)]\hat{v}_g + [e+cf_2(s)]\hat{R} \tag{2.9}$$

or

$$\hat{x}(s) = \frac{\text{adj}(sI-A-cg)[(b+cf_1(s))\hat{v}_g + (e+cf_2(s))\hat{R}]}{\det(sI-A-cg)} \tag{2.10}$$

Upon application of the inverse Laplace transform, eq. (2.10) becomes

$$\hat{x}(t) = L^{-1}\left\{\frac{\text{adj}(sI-A-cg)[(b+cf_1(s))\hat{v}_g + (e+cf_2(s))\hat{R}]}{\det(sI-A-cg)}\right\} \tag{2.11}$$

Equation (2.10) can be used to study the closed-loop dynamics in the frequency domain and eq. (2.11) can be used to study the transient responses due to small source and load variations in the time domain.

The poles of the closed-loop system are the eigenvalues of A+cg. They can be calculated by

$$\det(sI-A-cg) = 0 \qquad (2.12)$$

For stability, all the poles should be in the left half of the s-plane, and for fast transient responses, the dominant pole should have a large negative real part. Thus, a judicious choice of the feedback gain g can not only assure stability, but also provide a fast transient response for the system.

In fact, thanks to mathematical system theory, the poles can be placed anywhere desired if the system is controllable. Chapter 3 is a description of how to choose the feedback gain g so that the closed-loop poles can be assigned at the desired places. Once the feedback gain g is determined, eq. (2.10) can be used to determine $f_1(s)$ and $f_2(s)$ so that a better line rejection $\hat{v}(s)/\hat{v}_g(s)$ and load regulation $\hat{v}(s)/\hat{R}(s)$ can be obtained. In the case of the buck converter, f_1 can be chosen to null out the numerator of the line rejection function completely. Thus excellent line rejection can be realized. Notice that the choices of f_1 and f_2 do not affect the pole positions.

2.3 Closed-loop pole movement in the presence of multi-state feedback

The pole movement on the s-plane may be better understood by the following discussion. The closed-loop poles are determined by eq. (2.12), repeated here:

$$\det(sI-A-cg) = 0 \qquad (2.12)$$

But

$$\det(sI-A-cg) = \det\begin{pmatrix} s-a_{11}-c_1g_1 & -a_{12}-c_1g_2 & \cdots & -a_{1n}-c_1g_n \\ -a_{21}-c_2g_1 & s-a_{22}-c_2g_2 & \cdots & -a_{2n}-c_2g_n \\ \vdots & \vdots & & \vdots \\ -a_{n1}-c_ng_1 & -a_{n2}-c_ng_2 & \cdots & s-a_{nn}-c_ng_n \end{pmatrix}$$

$$= \det\begin{pmatrix} s-a_{11} & -a_{12} & \cdots & -a_{1n} \\ -a_{21} & s-a_{22} & \cdots & -a_{2n} \\ \vdots & \vdots & & \vdots \\ -a_{n1} & -a_{n2} & \cdots & s-a_{nn} \end{pmatrix}$$

$$+ \sum_{i=1}^{n} g_i \begin{pmatrix} s-a_{11} & \cdots & -a_{1(i-1)} & -c_1 & \cdots & -a_{1n} \\ -a_{21} & \cdots & s-a_{2(i-1)} & -c_2 & \cdots & -a_{2n} \\ \vdots & & \vdots & \vdots & & \vdots \\ -a_{n1} & \cdots & -a_{n(i-1)} & -c_n & \cdots & s-a_{nn} \end{pmatrix}$$

$$= \det(sI-A) + \sum_{i=1}^{n} g_i N_i(s)$$

$$= \det(sI-A) \cdot \left[1 + \sum_{i=1}^{n} T_i(s) \right] \qquad (2.13)$$

where $N_i(s)$ equals sI-A except that the i^{th} column is replaced by the vector -c,

$T_i(s) = g_i N_i(s) / \det(sI-A)$ is the loop gain associated with

with the i^{th} state variable.

Comparison of eq. (2.13) with the result for a single-loop feedback system, i.e., n=1 in eq. (2.13), shows that the sum of the loop gains $\sum_{i=1}^{n} T_i(s)$ replaces the role played by the usual single loop gain T: for stability, $\sum_{i=1}^{n} T_i(s)$ has to satisfy the Nyquist criterion; and for good regulation, $\sum_{i=1}^{n} T_i(s)$ has to have high gain and wide bandwidth.

The positions of the poles on the s-plane are determined by the linear combination of the loop gains. In the special case where only the i^{th} state is returned, $g = (0\ 0\cdots g_i\ 0\cdots 0)$, the closed-loop poles move from the open-loop pole positions $\det(sI-A) = 0$ to the zeros of $N_i(s)$ as g_i increases from 0 to ∞. A root-locus plot is shown in Fig. 2.2. If $N_i(s)$ has zeros in the right half-plane, the system could be unstable when the feedback gain g_i becomes too large. Output voltages of the boost, buck-boost and Ćuk converters belong to this category.

One way to overcome this stability problem is to feed back two state variables. Fig. 2.3 shows how to stabilize the system by feeding back a second state with left-half plane zeros. The system can be stabilized by proper choice of the weights between the two states. It is also noticed that the root loci expand from a line into an area, which means more design freedom is obtained.

In general, the span of the closed-loop poles on the s-domain increases as more and more states are returned in the feedback path. In particular, when all the states are fed back, the closed-loop poles can be assigned anywhere desired on the s-plane.

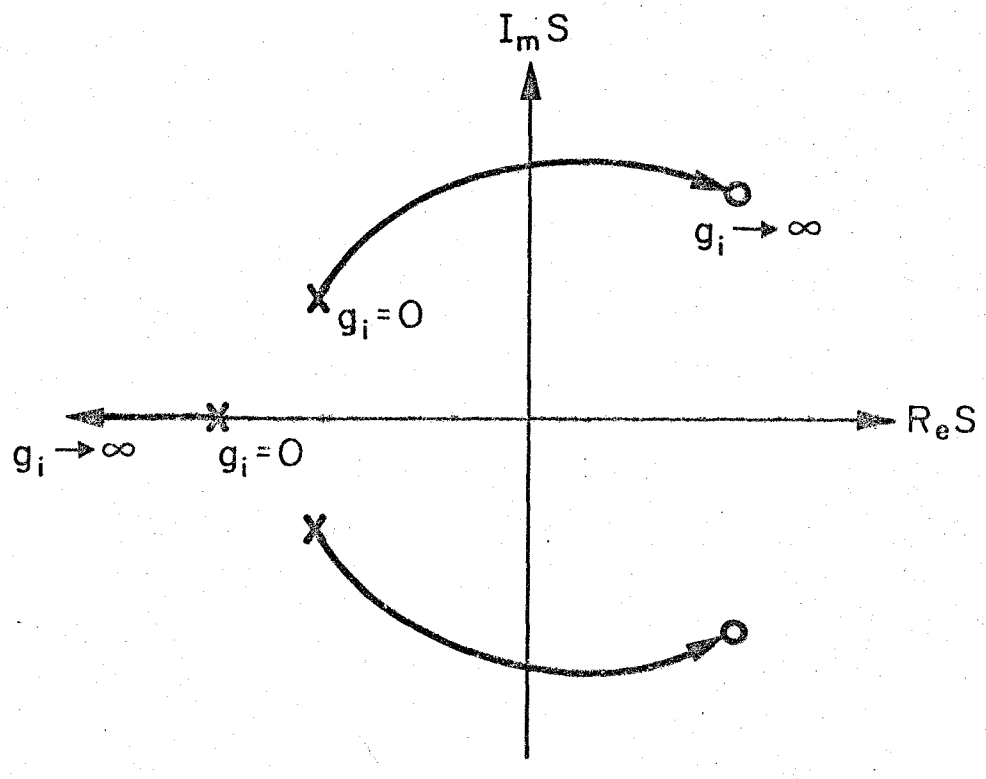

Fig. 2.2 Root-locus plot for a single-state feedback system with right-half plane zeros.

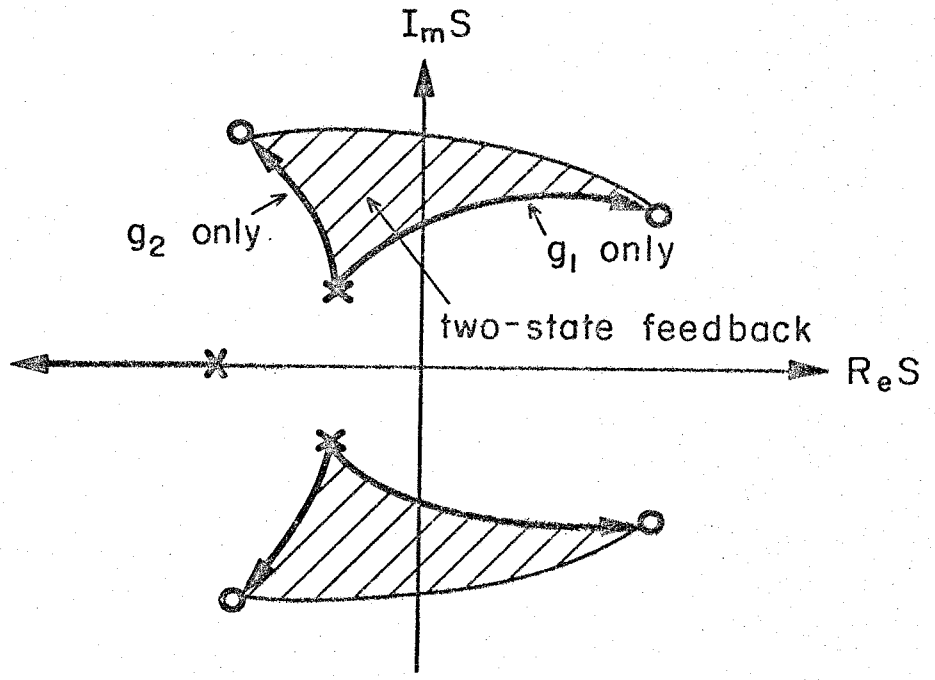

Fig. 2.3 The root loci are expanded into an area when two states are fed back in the system. The system can be stabilized by putting more weight on the feedback gain g_2.

CHAPTER 3

CALCULATION OF FEEDBACK GAINS FOR POLE PLACEMENT

Suppose that the closed-loop poles of a regulator are desired to be placed at $-\alpha_1, -\alpha_2, \ldots -\alpha_n$. One brute force method for solution of the feedback gains $g = (g_1, g_2, \ldots g_n)$ is to compare the coefficients on the two sides of the following equation

$$\det(sI-A-cg) = (s+\alpha_1)(s+\alpha_2) \ldots (s+\alpha_n) \tag{3.1}$$

However, the algebra can be very complicated as the order of the system increases. A more systematic method, which lends itself to direct computer programming, is presented in the following.

The system of eq. (2.7), repeated here with $\hat{R}$ omitted for simplicity,

$$s\hat{x} = A\hat{x} + c\hat{d} + b\hat{v}_g \tag{3.2}$$

will be transformed into its "phase variable canonical form" as in eq. (3.9) so that the gain g can be easily determined. To transform an arbitrary matrix into its phase variable canonical form, two successive changes of variables are performed. First, the system is transformed into its diagonalized form through a similarity transformation:

$$\hat{x} = T\hat{y} \qquad \text{where columns of T are the eigenvectors of A} \tag{3.3}$$

Assume that the system has distinct eigenvalues $\lambda_1, \lambda_2, \ldots \lambda_n$; then, the new system matrix has a diagonal form:

$$s\hat{y} = \Lambda\hat{y} + T^{-1}c\hat{d} + T^{-1}b\hat{v}_g \tag{3.4}$$

where

$$\Lambda = T^{-1}AT = \begin{pmatrix} \lambda_1 & & & \\ & \lambda_2 & & 0 \\ & & \ddots & \\ 0 & & & \lambda_n \end{pmatrix}$$

This diagonal form can be further transformed into the desired phase variable canonical form through a Vandermonde transformation:

$$\hat{z} = VK\hat{y} \tag{3.5}$$

where

$$V = \begin{pmatrix} 1 & 1 & \cdots & 1 \\ \lambda_1 & \lambda_2 & & \lambda_n \\ \vdots & \vdots & & \vdots \\ \lambda_1^{n-1} & \lambda_2^{n-1} & & \lambda_n^{n-1} \end{pmatrix} \qquad K = \begin{pmatrix} k_1 & & & \\ & k_2 & & 0 \\ & & \ddots & \\ 0 & & & k_n \end{pmatrix}$$

V is the Vandermonde matrix for Λ, which tranforms a diagonal matrix into its phase variable canonical form. Matrix K is just a scaling factor whose function is to transform the coefficient of $\hat{d}$ into $(0\ 0\ \ldots\ -1)^T$ as in eq. (3.9). With this Vandermonde transformation, the state equation in terms of $\hat{z}$ becomes

$$s\hat{z} = P\hat{z} + (VKT^{-1}c)\hat{d} + (VKT^{-1}b)\hat{v}_g \tag{3.6}$$

where

$$P = V\Lambda V^{-1} = \begin{pmatrix} 0 & 1 & 0 & \cdots & 0 & 0 \\ 0 & 0 & 1 & \cdots & 0 & 0 \\ \cdot & \cdot & \cdot & & \cdot & \cdot \\ \cdot & \cdot & \cdot & & \cdot & \cdot \\ \cdot & \cdot & \cdot & & \cdot & \cdot \\ 0 & 0 & 0 & \cdots & 0 & 1 \\ -a_1 & -a_2 & -a_3 & \cdots & -a_{n-1} & -a_n \end{pmatrix}$$

The next step is to determine the scaling factor K such that the coefficient of $\hat{d}$ is simplified to $(0\ 0\ \ldots\ -1)^T$

i.e. $$VKT^{-1}c = (0\ 0\ \ldots\ -1)^T \tag{3.7}$$

or

$$\begin{pmatrix} k_1 & & & \\ & k_2 & & 0 \\ & & \ddots & \\ 0 & & & k_n \end{pmatrix} T^{-1}c = V^{-1} \begin{pmatrix} 0 \\ 0 \\ \cdot \\ \cdot \\ \cdot \\ -1 \end{pmatrix} \tag{3.8}$$

Apparently, if all the n elements of $T^{-1}c$ are non-zero, a unique solution for K can be easily obtained. On the other hand, if $T^{-1}c$ has a zero element in it, the system is called "uncontrollable", which means that K cannot be solved and the poles cannot be placed as desired. It will be assumed here that the system is controllable, i.e. K has a unique solution. Equation (3.6) then becomes the desired canonical form:

$$s\hat{z} = \begin{pmatrix} 0 & 1 & 0 & \cdots & 0 & 0 \\ 0 & 0 & 1 & \cdots & 0 & 0 \\ \vdots & \vdots & \vdots & & \vdots & \vdots \\ 0 & 0 & 0 & \cdots & 0 & 1 \\ -a_1 & -a_2 & -a_3 & \cdots & -a_{n-1} & -a_n \end{pmatrix} \hat{z} + \begin{pmatrix} 0 \\ 0 \\ \vdots \\ 0 \\ -1 \end{pmatrix} \hat{d} + (VKT^{-1}b)\hat{v}_g \qquad (3.9)$$

With substitution of a linear feedback

$$\hat{d} = g\hat{x} + f_1\hat{v}_g = gTK^{-1}V^{-1}\hat{z} + f_1\hat{v}_g = (h_1\ h_2\ \cdots\ h_n)\hat{z} + f_1\hat{v}_g \qquad (3.10)$$

into eq. (3.9),

$$s\hat{z} = \begin{pmatrix} 0 & 1 & \cdots & 0 \\ 0 & 0 & \cdots & 0 \\ \vdots & \vdots & & \vdots \\ 0 & 0 & & 1 \\ -(a_1+h_1) & -(a_2+h_2) & \cdots & -(a_n+h_n) \end{pmatrix} \hat{z} + \left[VKT^{-1}b - \begin{pmatrix} 0 \\ 0 \\ \vdots \\ 0 \\ 1 \end{pmatrix} f_1 \right] \hat{v}_g \qquad (3.11)$$

The closed-loop poles of this system satisfy the much simplified equation

$$\begin{aligned} &\det[sI-P+(0\ 0\ \cdots\ 1)^T h] \\ &= s^n + (a_n+h_n)s^{n-1} + \cdots + (a_2+h_2)s + (a_1+h_1) \\ &= 0 \end{aligned} \qquad (3.12)$$

But the desired poles are

$$(s+\alpha_1)(s+\alpha_2)\ \cdots\ (s+\alpha_n)$$

$$= \det(sI-A-cg)$$

$$= \det(VKT^{-1})\cdot\det(sI-A-cg)\cdot\det(VKT^{-1})^{-1}$$

$$= \det[VKT^{-1}sITK^{-1}V^{-1} - VK(T^{-1}AT)K^{-1}V^{-1} - VKT^{-1}c(gTK^{-1}V^{-1})]$$

$$= \det(sI - P + (0\ 0\ \ldots\ 1)^T h)$$

$$= s^n + (a_n+h_n)s^{n-1} + \ldots + (a_2+h_2)s + (a_1+h_1) \tag{3.13}$$

Equation (3.13) can be used to solve for the feedback gain $h = (h_1\ h_2\ \ldots\ h_n)$ in the $\hat{z}$ coordinate easily. Once the h-vector is solved, the desired feedback gain

$$g = hVKT^{-1} \tag{3.14}$$

in the original $\hat{x}$ coordinate can be calculated.

In summary, the system is first transformed into its canonical form through two similarity transformations. Since eigenvalues are invariant under similarity transformations, the feedback gain can be easily determined in the canonical space. The feedback gain is then transformed back to its original coordinate system. The symbols used are summarized in the following. The open-loop poles satisfy

$$\begin{aligned}
&(s-\lambda_1)(s-\lambda_2)\ \ldots\ (s-\lambda_n) \\
&= \det(sI-A) \\
&= \det(sI-P) \\
&= s^n + a_n s^{n-1} + \ldots + a_2 s + a_1 \\
&= 0
\end{aligned} \tag{3.15}$$

The desired closed-loop poles satisfy

$$\begin{aligned}
&(s+\alpha_1)(s+\alpha_2)\ \ldots\ (s+\alpha_n) \\
&= \det(sI-A-cg) \\
&= \det(sI-P+(0\ 0\ \ldots\ 1)^T h) \\
&= s^n + (a_n+h_n)s^{n-1} + \ldots + (a_1+h_1)
\end{aligned}$$

$$= 0 \qquad (3.16)$$

By choosing appropriate h_i's, which can be transformed back to g_i's through eq.(3.14), the closed-loop poles can be assigned at anywhere desired. Since A is a real matrix, all the a_i's are real numbers. Hence h_i's are real from eq. (3.16). But $g = h \cdot VKT^{-1}$ and VKT^{-1} is real from eq. (3.7), so g is always real. Note that the gain $f_1(s)$ from the source voltage does not affect the positions of the poles.

Although this method is applicable only to controllable systems with distinct eigenvalues, real systems almost always fall into this category, fortunately. A slight change in the values of the circuit elements can separate the degenerate eigenvalues and make all the elements in $T^{-1}c$ non-zero.

A computer program can be developed to solve for the feedback gain using this technique. A flowchart is presented in Fig. 3.1.

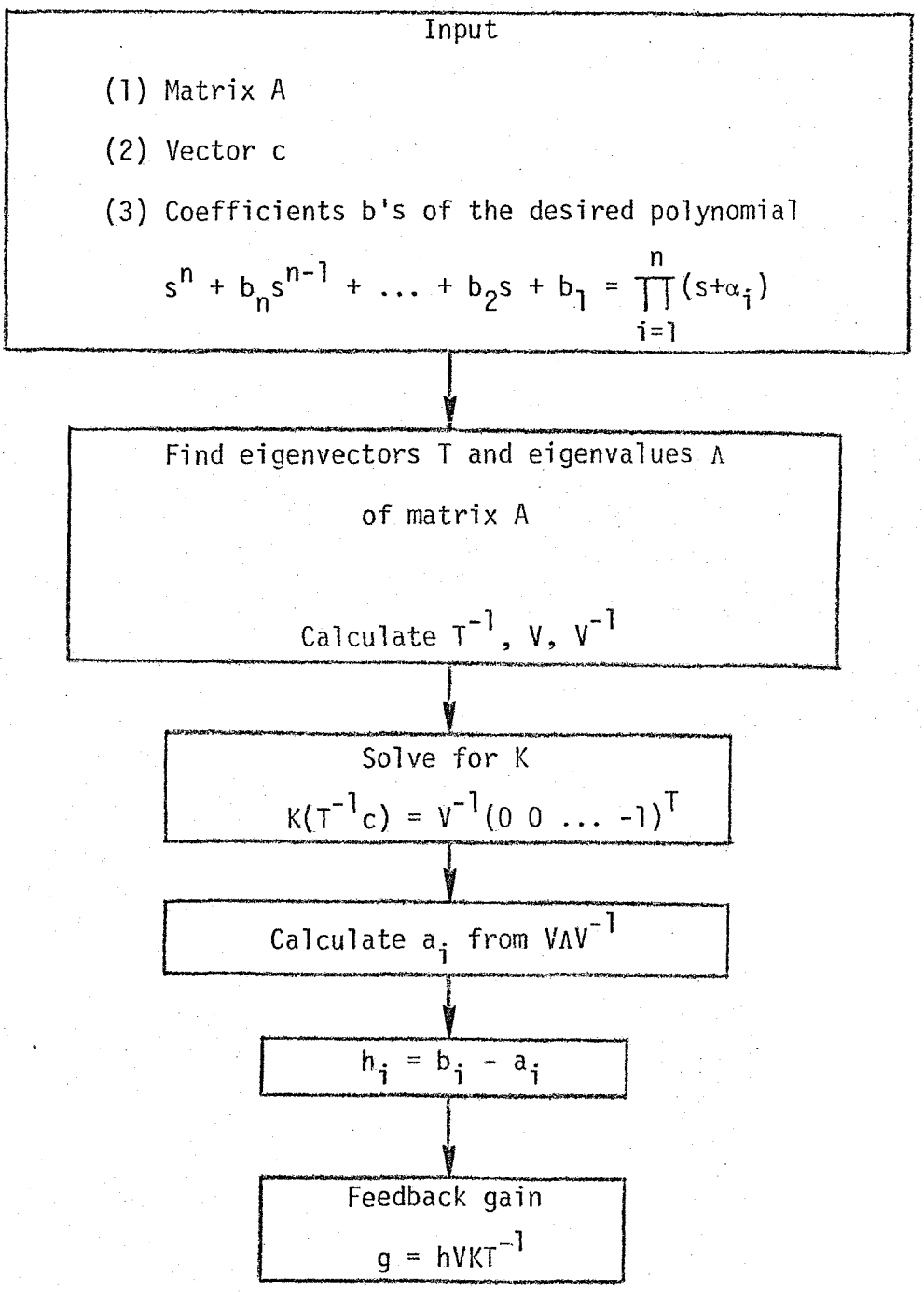

Fig. 3.1 Flowchart for solving feedback gain g

CHAPTER 4

ILLUSTRATIVE EXAMPLE OF A TOTAL-STATE FEEDBACK BOOST REGULATOR

The methods discussed in the previous chapters are illustrated in this chapter by a boost converter. The design equations are developed in Sec. 4.1 and the experimental circuit and data are given in Sec. 4.2. The same converter is designed again in Sec. 4.3 using the conventional single-loop compensation method to compare the merits of the total-state feedback vs. single-loop feedback.

4.1 Design of a total-state feedback boost regulator

The design equations for a total-state feedback boost converter, whose basic configuration is shown in Fig. 4.1, are developed in this section.

The state-space equations for the two states, inductor current i_ℓ and output voltage v, are:

$$\begin{pmatrix} \dot{i}_\ell \\ \dot{v} \end{pmatrix} = \begin{pmatrix} 0 & 0 \\ 0 & \frac{-1}{R_L C} \end{pmatrix} \begin{pmatrix} i_\ell \\ v \end{pmatrix} + \begin{pmatrix} \frac{1}{L} \\ 0 \end{pmatrix} v_g \qquad \text{during } dT_s \qquad (4.1)$$

$$\begin{pmatrix} \dot{i}_\ell \\ \dot{v} \end{pmatrix} = \begin{pmatrix} 0 & \frac{-1}{L} \\ \frac{1}{C} & \frac{-1}{R_L C} \end{pmatrix} \begin{pmatrix} i_\ell \\ v \end{pmatrix} + \begin{pmatrix} \frac{1}{L} \\ 0 \end{pmatrix} v_g \qquad \text{during } d'T_s \qquad (4.2)$$

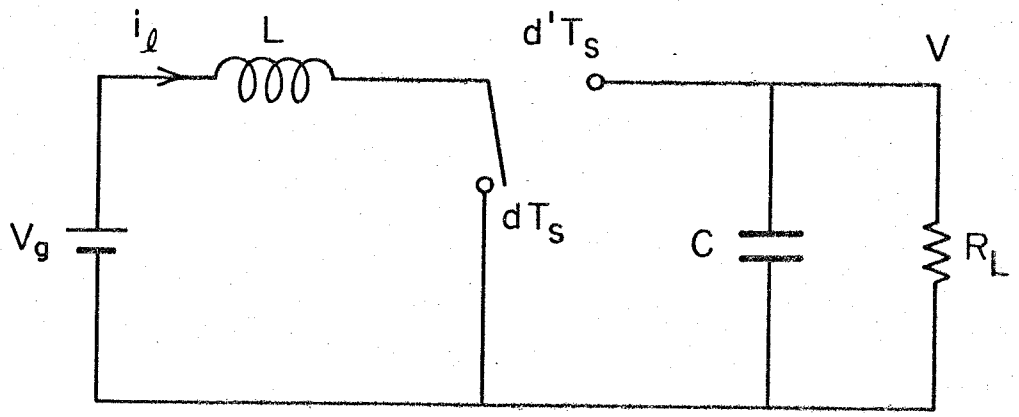

Fig. 4.1 Basic configuration of a boost converter.

Proceeding with the state-space averaging method, one can weight-average these two equations to obtain a single equation which describes the average behavior of the converter:

$$\begin{pmatrix} \dot{i}_\ell \\ \dot{v} \end{pmatrix} = \begin{pmatrix} 0 & \frac{-d'}{L} \\ \frac{d'}{C} & \frac{-1}{R_L C} \end{pmatrix} \begin{pmatrix} i_\ell \\ v \end{pmatrix} + \begin{pmatrix} \frac{1}{L} \\ 0 \end{pmatrix} v_g \tag{4.3}$$

In order to arrive at a linear time-invariant description of the system, the state variables can be perturbed around their operating point by substitution of

$$\begin{aligned} v &= \hat{v} + V \\ i_\ell &= \hat{i}_\ell + I_L \\ v_g &= \hat{v}_g + V_g \\ d &= \hat{d} + D \\ R_L &= \hat{R} + R \end{aligned} \tag{4.4}$$

into eq. (4.3). With omission of the second-order terms, the desired set of linear time-invariant differential equations is obtained:

$$s\begin{pmatrix} \hat{i}_\ell \\ \hat{v} \end{pmatrix} = \begin{pmatrix} 0 & \frac{-D'}{L} \\ \frac{D'}{C} & \frac{-1}{RC} \end{pmatrix} \begin{pmatrix} \hat{i}_\ell \\ \hat{v} \end{pmatrix} + \begin{pmatrix} \frac{1}{L} \\ 0 \end{pmatrix} \hat{v}_g + \begin{pmatrix} \frac{V}{L} \\ -\frac{I_L}{C} \end{pmatrix} \hat{d} + \begin{pmatrix} 0 \\ \frac{V}{R^2 C} \end{pmatrix} \hat{R} \tag{4.5}$$

If integral control is used, a new state

$$\hat{\varepsilon} = \int \hat{v} dt \tag{4.6}$$

should be incorporated into the state equation (4.5):

$$s\begin{pmatrix} \hat{i}_\ell \\ \hat{v} \\ \hat{\varepsilon} \end{pmatrix} = \begin{pmatrix} 0 & \frac{-D'}{L} & 0 \\ \frac{D'}{C} & \frac{-1}{RC} & 0 \\ 0 & 1 & 0 \end{pmatrix} \begin{pmatrix} \hat{i}_\ell \\ \hat{v} \\ \hat{\varepsilon} \end{pmatrix} + \begin{pmatrix} \frac{1}{L} \\ 0 \\ 0 \end{pmatrix} \hat{v}_g + \begin{pmatrix} \frac{V}{L} \\ \frac{-I_L}{C} \\ 0 \end{pmatrix} \hat{d} + \begin{pmatrix} 0 \\ \frac{V}{R^2C} \\ 0 \end{pmatrix} \hat{R} \tag{4.7}$$

With substitution of the total-state feedback

$$\hat{d} = (g_1 \; g_2 \; g_3)(\hat{i}_\ell \; \hat{v} \; \hat{\varepsilon})^T + f_1(s)\hat{v}_g \tag{4.8}$$

into eq. (4.7), the closed-loop behavior of the converter is described by

$$s\begin{pmatrix} \hat{i}_\ell \\ \hat{v} \\ \hat{\varepsilon} \end{pmatrix} = \begin{pmatrix} \frac{g_1 V}{L} & \frac{g_2 V}{L} - \frac{D'}{L} & \frac{g_3 V}{L} \\ \frac{D'}{C} - \frac{g_1 I_L}{C} & \frac{-1}{RC} - \frac{g_2 I_L}{C} & \frac{-g_3 I_L}{C} \\ 0 & 1 & 0 \end{pmatrix} \begin{pmatrix} \hat{i}_\ell \\ \hat{v} \\ \hat{\varepsilon} \end{pmatrix}$$

$$+ \begin{pmatrix} \frac{1}{L} + \frac{f_1 V}{L} \\ \frac{-I_L f_1}{C} \\ 0 \end{pmatrix} \hat{v}_g + \begin{pmatrix} 0 \\ \frac{V}{R^2C} \\ 0 \end{pmatrix} \hat{R} \tag{4.9}$$

With use of the inverse of the matrix sI-A-cg,

$$\begin{pmatrix} \hat{i}_\ell \\ \hat{v} \\ \hat{\varepsilon} \end{pmatrix} = \frac{\begin{pmatrix} -- & \frac{-s(D'-g_2V)+g_3V}{L} & -- \\ \frac{-s(g_1I_L-D')}{C} & s(s-\frac{g_1V}{L}) & -- \\ -- & -- & -- \end{pmatrix} \left[\begin{pmatrix} \frac{1+f_1V}{L} \\ \frac{-I_Lf_1}{C} \\ 0 \end{pmatrix} \hat{v}_g + \begin{pmatrix} 0 \\ \frac{V}{R^2C} \\ 0 \end{pmatrix} \hat{R} \right]}{s(s^2+\frac{s}{RC}+\frac{D'^2}{LC}) - \frac{g_1V}{L}s(s+\frac{2}{RC}) + \frac{g_2I_L}{C}s(s-\frac{RD'^2}{L}) + \frac{g_3I_L}{C}(s-\frac{D'^2R}{L})} \tag{4.10}$$

The open-loop poles of the system are

$$s\,(s^2+\frac{s}{RC}+\frac{D'^2}{LC}) = 0 \tag{4.11}$$

The three loop gains associated with inductor current, output voltage and integral of error signal are:

$$T_{i\ell} = \frac{\frac{-g_1V}{L}(s+\frac{2}{RC})}{s^2+\frac{s}{RC}+\frac{D'^2}{LC}} \tag{4.12}$$

$$T_v = \frac{\frac{g_2I_L}{C}(s-\frac{D'^2R}{L})}{s^2+\frac{s}{RC}+\frac{D'^2}{LC}} \tag{4.13}$$

$$T_{\varepsilon} = \frac{\frac{g_3 I_L}{C}(s - \frac{D'^2 R}{L})}{s(s^2 + \frac{s}{RC} + \frac{D'^2}{LC})} \tag{4.14}$$

The root locus corresponding to each of the three feedback gains are plotted in Fig. 4.2, 4.3 and 4.4.

From eq. (4.10), the closed-loop line rejection is

$$\frac{\hat{v}}{\hat{v}_g} = \frac{s\left[\frac{1}{V} - \frac{g_1}{RD'^2} + f_1(s)(1 - \frac{sL}{RD'^2})\right]}{-g_3(1 + \frac{s}{\alpha_1})(1 + \frac{s}{\alpha_2})(1 + \frac{s}{\alpha_3})} \tag{4.15}$$

where α_1, α_2, α_3 are the desired pole positions.

It is seen from the root loci and eq. (4.15) that the negative feedback from the inductor current $-g_1$ moves the poles away from the imaginary axis to stabilize and speed up the converter, but, at the same time, it degrades the line rejection. Quite on the contrary, the feedback from the integral of the output voltage error tends to destabilize the system but improves the line rejection. A compromise has to be made between stability margins and line rejection. The feedback from the source voltage $f_1(s)$ can be chosen to minimize the numerator of eq. (4.15) to improve the line rejection.

The transient responses of the inductor current and the output voltage due to small load variation can be calculated from eq. (4.10) to be:

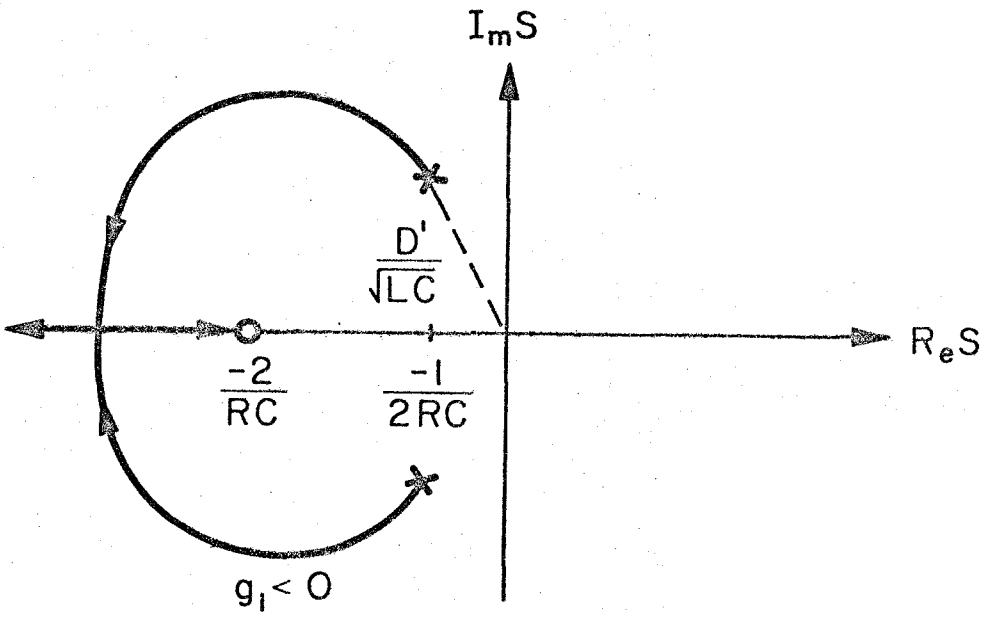

Fig. 4.2 Root loci for feeding back the inductor current alone.

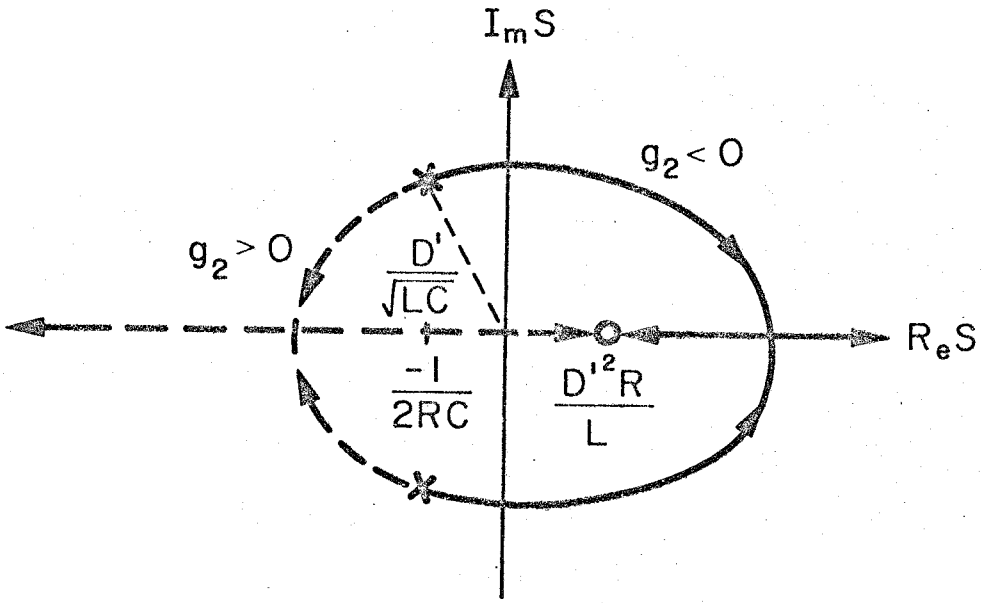

Fig. 4.3 Root loci for feeding back the output voltage alone.

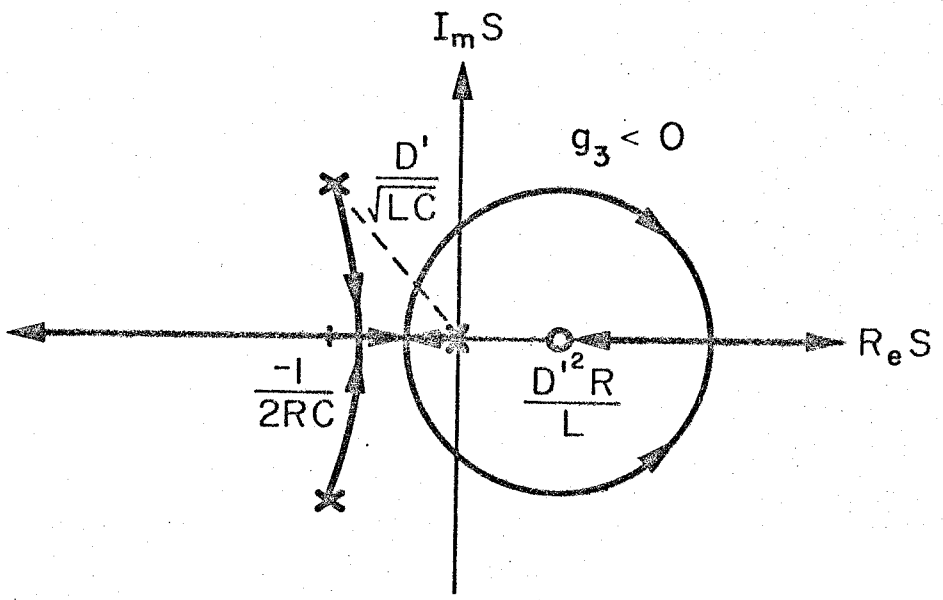

Fig. 4.4 Root loci for feeding back the integral of the output voltage error alone.

$$\hat{i}_\ell(t) = L^{-1}\left\{\frac{-\frac{V}{R^2LC}[s(D'-g_2V) - g_3V]}{(s+\alpha_1)(s+\alpha_2)(s+\alpha_3)}\right\}\hat{R}(s) \qquad (4.16)$$

$$\hat{v}(t) = L^{-1}\left\{\frac{\frac{V}{R^2C}s\left(s-\frac{g_1V}{L}\right)}{(s+\alpha_1)(s+\alpha_2)(s+\alpha_3)}\right\}\hat{R}(s) \qquad (4.17)$$

where α_1, α_2, α_3 are the desired pole positions.

4.2 Implementation and experimental data

A total-state feedback boost converter has been constructed whose circuit diagram is shown in Fig. 4.5. The source voltage is 15V and the output voltage is regulated at 30V. Nominal load is 75Ω. Both states in the system, input inductor current and output capacitor voltage are sensed so that the closed-loop poles can be assigned anywhere on the s-plane. Integral control and source voltage sensing are used to improve the line rejection. The ac component of the inductor current is sensed by integrating the voltage across the inductor which was wound on a Magnetics Inc. pot core G-42616-25 with 90 turns of 24 AWG wire. The voltage across the inductor is sensed by the 11 turns of 24 AWG wire wound on the same core. The feedback gains from the output error signal and its integral were implemented on the same operational amplifier because they have the same sign in this example. All the feedback signals were summed up in a quarter of LM324 to control the duty ratio of the power transistor through the control chip SG 3524

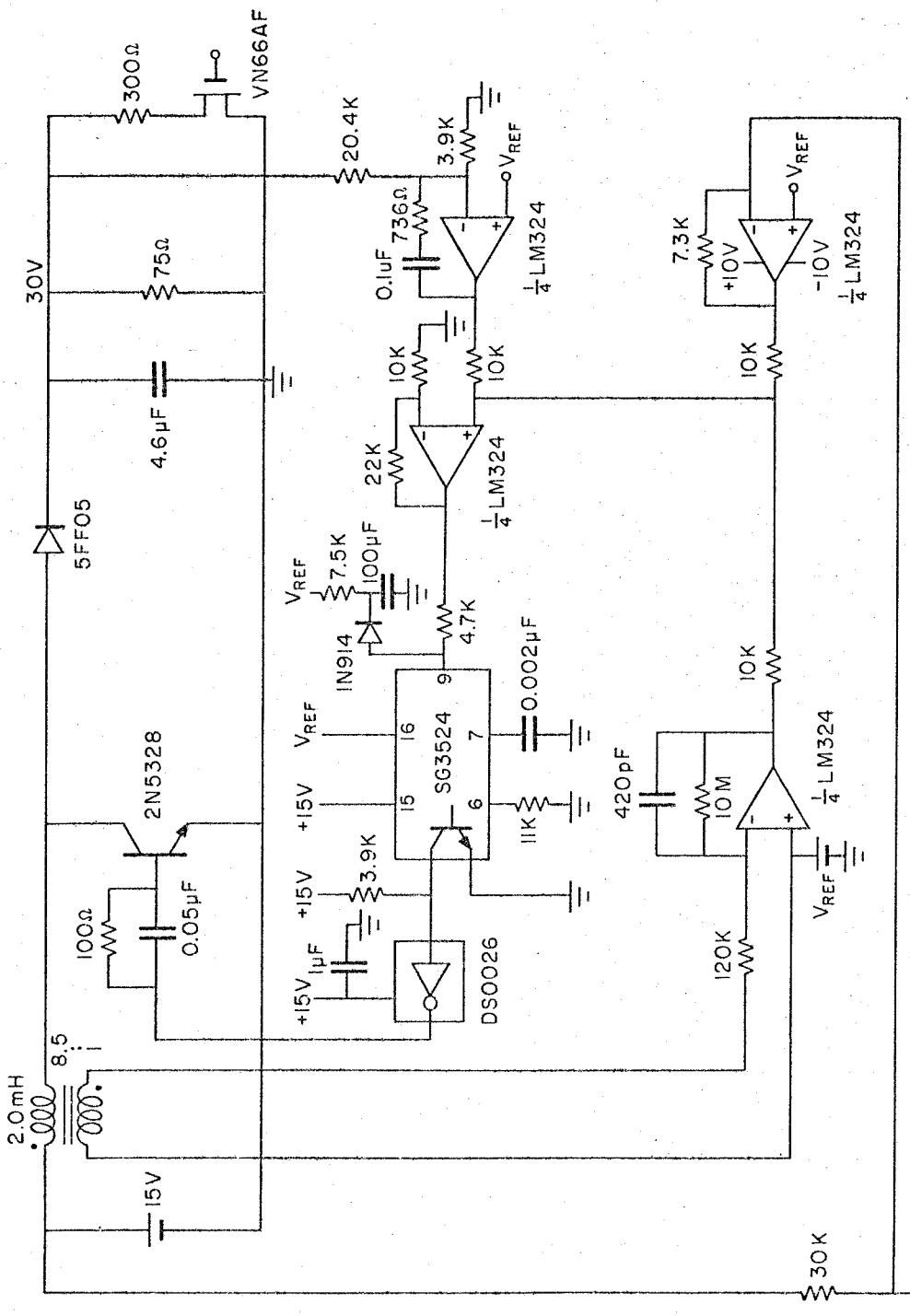

Fig. 4.5 An experimental 12W total-state feedback boost regulator.

and the base driver DS0026. The switching frequency is fixed at 50 KH_z and the nominal duty ratio is 0.5.

The selection of the pole positions is a compromise between stability, transient response, and line rejection. For good stability and fast transient, the poles should have large negative real parts, but the feedback gain required may be too high to be practical. High-Q complex pole pairs should be avoided because of the low stability margin and high peak in the frequency response of the line rejection. As an example, suppose that the closed-loop poles are desired to be at $s=-4000, -4000, -2\times10^4$ sec^{-1} so that the converter is well stabilized and its transient responses are dominated by the 250 μs time constant. The required feedback gains can be calculated to be

$$g_1 = -1.84 \qquad g_2 = -0.0142 \qquad g_3 = -196 \tag{4.18}$$

The component values in Fig. 4.5 are selected according to these values. Since both g_2 and g_3 are negative, they can be implemented by a single op-amp.

The closed-loop transient response of the system can be well displayed by the load to inductor current transfer function eq. (4.16). With the feedback gains as chosen, the response of $\hat{i}_\ell$ to a 20% step change of the load from 75Ω to 60Ω is

$$\hat{i}_\ell(t) = 0.16 - 0.18\, e^{\frac{-t}{250}} - 3\times10^{-4} t e^{\frac{-t}{250}} + 0.021\, e^{\frac{-t}{50}} \tag{4.19}$$

in which $\hat{i}_\ell$ is in amps and t is in μsec.

Note that the third term has a negative maximum of only -0.027 at t=250 μs. Apparently, the first two terms are dominant during the transient. The output voltage waveform during this transient can be calculated from eq. (4.17):

$$\hat{v}(t) = -0.026te^{\frac{-t}{250}} + 0.52e^{\frac{-t}{250}} - 0.52e^{\frac{-t}{50}} \qquad (4.20)$$

in which $\hat{v}$ is in volts and t is in μsec.

The first term, which has a negative maximum of -2.37 at t=250 μs, is the dominant one. The predicted transient responses of the inductor current and output voltage eqs. (4.19) and (4.20) are plotted in Fig. 4.6. The actual waveforms on the oscilloscope are given in Fig. 4.7. The slightly lower final value predicted by eq. (4.19) is due to the fact that 20% change on the load exceeds the assumption of small-signal pertubation in the state-space average method. However, the accuracy of the time dependence is still quite acceptable.

From eq. (4.15), the closed-loop line rejection is

$$\frac{\hat{v}}{\hat{v}_g} = \left(\frac{s/2\pi}{31Hz}\right)\frac{\left[0.131 + f_1(s)\left(1 - \frac{s/2\pi}{1490Hz}\right)\right]}{\left(1 + \frac{s/2\pi}{637Hz}\right)^2\left(1 + \frac{s/2\pi}{3180Hz}\right)} \qquad (4.21)$$

If f_1=0, i.e., without monitoring the source voltage, the line rejection is

$$\frac{\hat{v}}{\hat{v}_g} = \left(\frac{s/2\pi}{239Hz}\right)\cdot\frac{1}{\left(1 + \frac{s/2\pi}{637Hz}\right)^2\left(1 + \frac{s/2\pi}{3180Hz}\right)} \qquad (4.22)$$

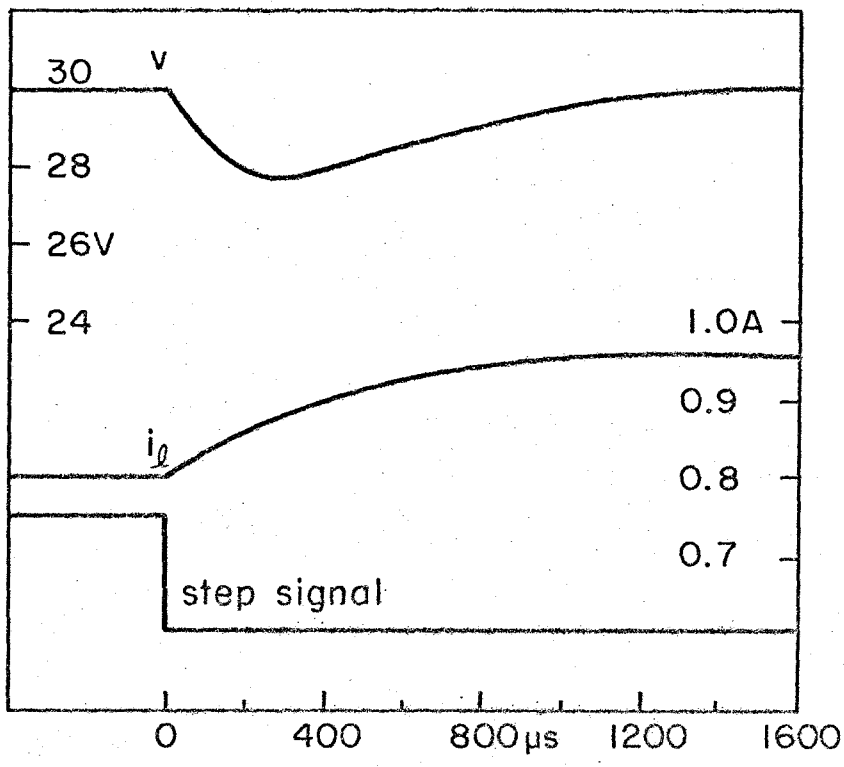

Fig. 4.6 Predicted transient responses of the inductor current and the output voltage under a 20% step load change.

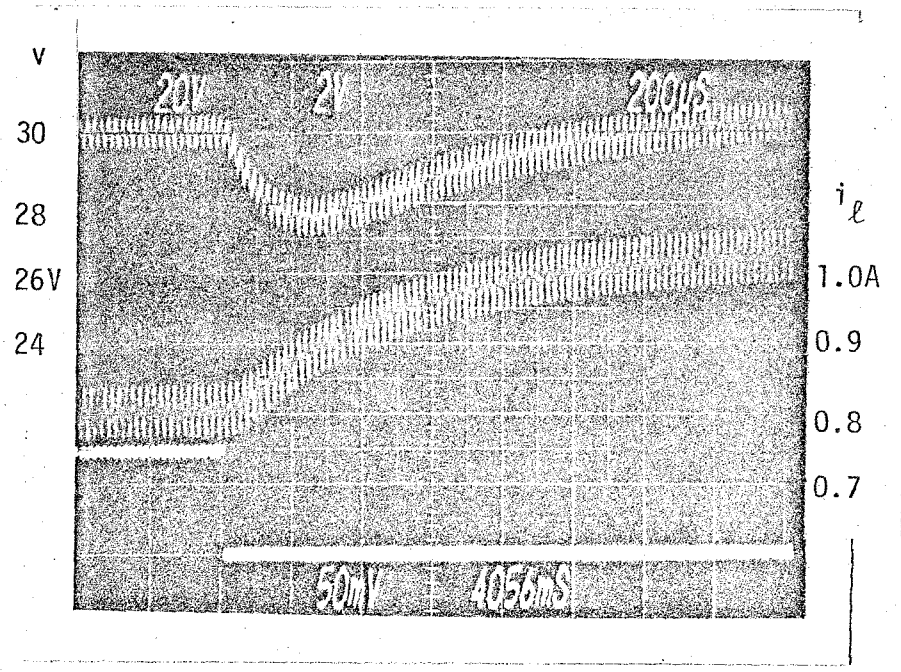

Fig. 4.7 Actual transient waveforms observed on the oscilloscope.

The asymptotes of this equation are plotted in Fig. 4.8 as the dotted lines. The open circles are the measured data. To improve the line rejection at low and medium frequency, f_1 can be chosen to minimize the numerator. With $f_1 = -0.092$, the low frequency line rejection can be improved and the zero introduced by f_1 cancels one of the poles, $s = -4000\ \text{sec}^{-1} = -2\pi \cdot 637\text{Hz}$. The line rejection then becomes

$$\frac{\hat{v}}{\hat{v}_g} = \left(\frac{s/2\pi}{797\text{Hz}}\right) \cdot \frac{1}{\left(1 + \frac{s/2\pi}{637\text{Hz}}\right)\left(1 + \frac{s/2\pi}{3180\text{Hz}}\right)} \tag{4.23}$$

The asymptotes of eq. (4.23) are shown in Fig. 4.8 as the solid lines. The "x" are the measured data. The deviation at the low frequency end is expected to be the non-exact cancellation of the pole and the zero because the position of the second zero is extremely sensitive to the value of f_1. It moves from ∞ when f_1=0 to 637Hz when f_1=-0.092 and to 0Hz when f_1=-0.131.

Note that this improvement on the line rejection by sensing the source voltage and modulating the duty ratio of the switch is of small-signal nature. A different approach, the feed-forward technique, which nulls out the source variations by modulation of the switching frequency, can be of large-signal nature.

4.3 Comparison with conventional single-loop design

In this section, the same boost converter used in Sec. 4.2 is redesigned using the conventional single-pole compensation

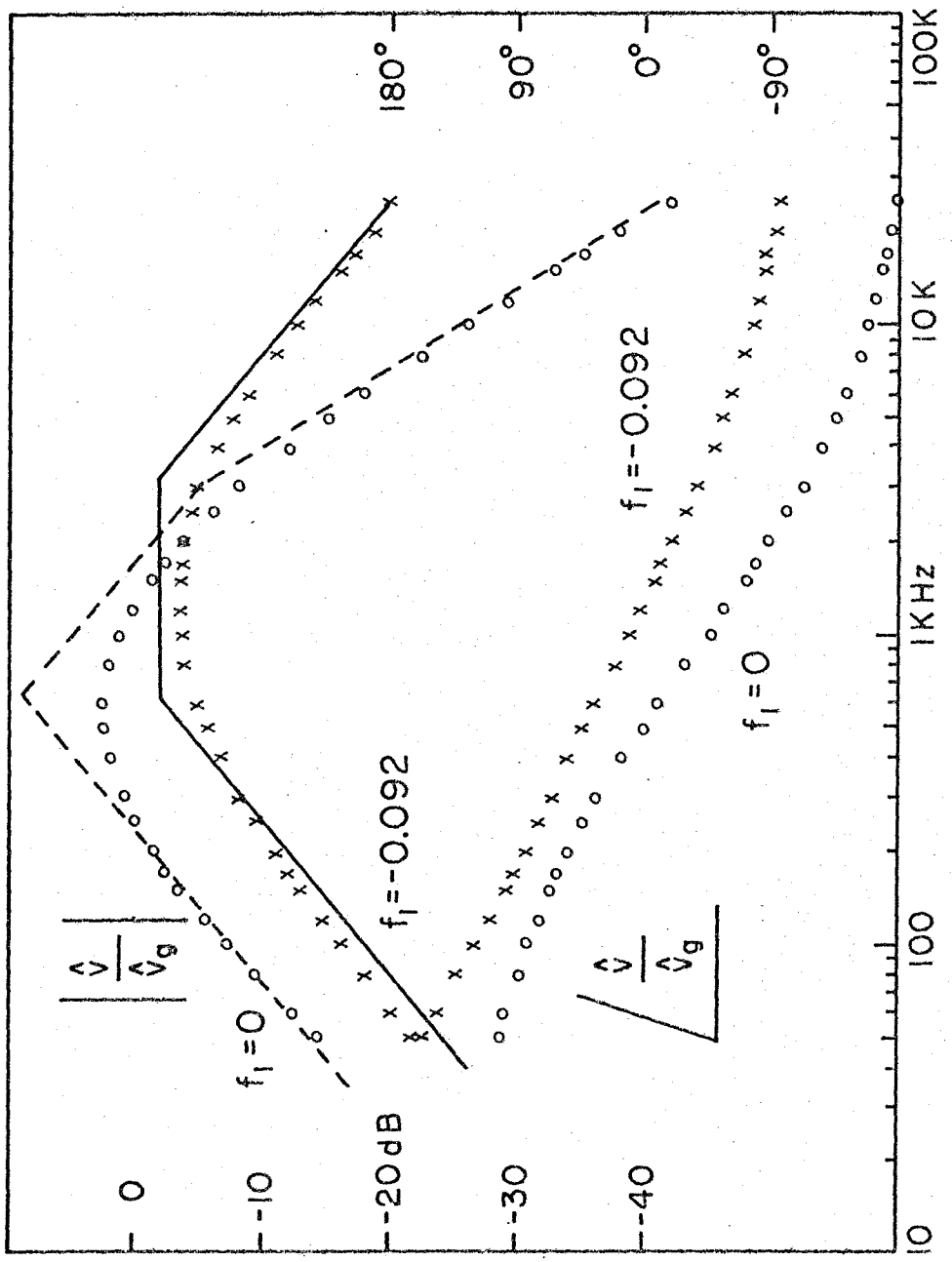

Fig. 4.8 Predicted asymptotes and measured data of the line rejection of the circuit in Fig. 4.5.

technique to compare the merits of the two designs.

From eq. (4.13), it is seen that the loop gain of a boost power stage has a pair of complex poles and a right half-plane zero. The right half-plane zero makes it very difficult to design a stable system with high loop gain. One common remedy to this problem is to add a single pole at very low frequency in the compensation network as shown in Fig. 4.9. The feedback gain can then be increased with loop gain crossover at low frequency with -6dB/oct slope. The stability problem is solved and the static regulation is improved. The following is a quantitative analysis of this compensation technique.

In Fig. 4.9 the duty ratio modulation $\hat{d}$ is related to the output voltage variation $\hat{v}$ by the following equation:

$$\hat{d} = \frac{-g\hat{v}}{1 + s/\omega_1} \tag{4.24}$$

where

$$g = \frac{R_1}{R_2}$$

$$\omega_1 = \frac{1}{R_1 C_1}$$

Substitution of eq. (4.24) into the state equation (4.5) of the boost converter, with $\hat{R}$ omitted, gives

$$\begin{pmatrix} \hat{i}_\ell \\ \hat{v} \end{pmatrix} = \begin{pmatrix} s & \frac{D'}{L} + \frac{V}{L} \cdot \frac{g}{1+s/\omega_1} \\ \frac{-D'}{C} & s + \frac{1}{RC} - \frac{I_L}{C} \cdot \frac{g}{1+s/\omega_1} \end{pmatrix}^{-1} \begin{pmatrix} \frac{1}{L} \\ 0 \end{pmatrix} \hat{v}_g$$

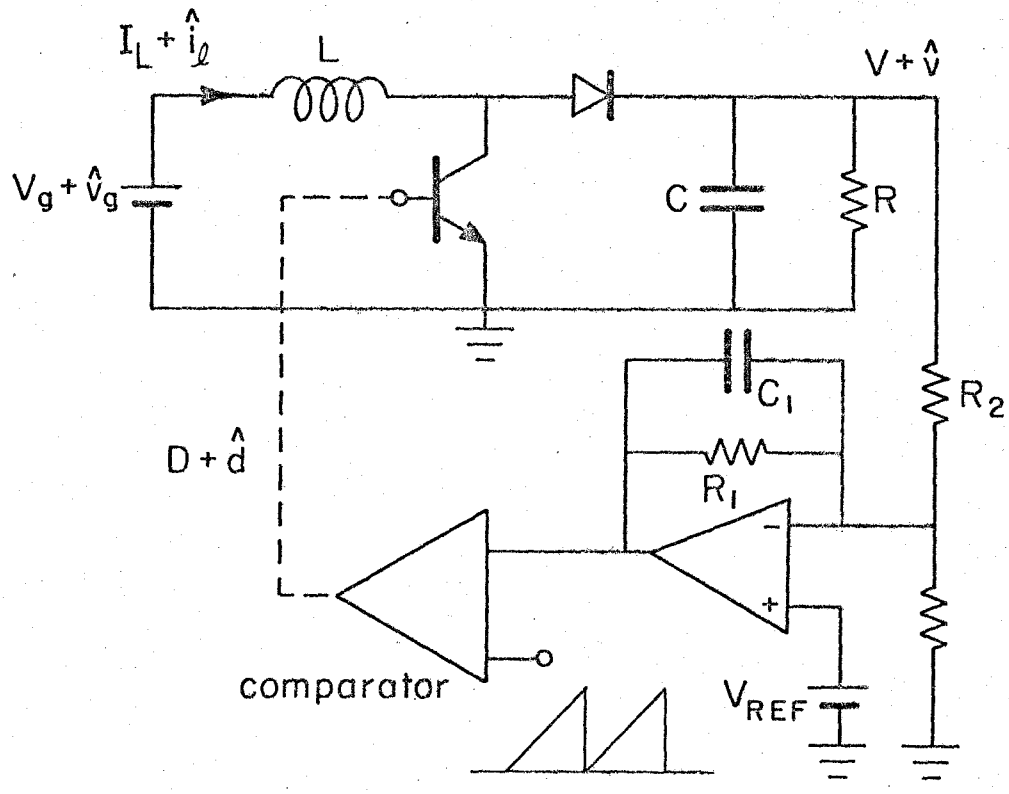

Fig. 4.9 Conventional single-pole compensation technique.

$$= \frac{\begin{pmatrix} (s+\frac{1}{RC})(1+s/\omega_1) - \frac{I_L g}{C} & \frac{-D'}{L}(1+s/\omega_1) - \frac{gV}{L} \\ \frac{D'}{C}(1+s/\omega_1) & s(1+s/\omega_1) \end{pmatrix} \begin{pmatrix} \frac{1}{L} \\ 0 \end{pmatrix} \hat{v}_g}{(1+s/\omega_1)\left(s^2 + \frac{s}{RC} + \frac{D'^2}{LC}\right) + g\frac{VD'}{LC}\left(1 - \frac{sL}{RD'^2}\right)} \tag{4.25}$$

The closed-loop line rejection is

$$\frac{\hat{v}}{\hat{v}_g} = \frac{1 + s/\omega_1}{D'(1+s/\omega_1)\left(1 + \frac{sL}{RD'^2} + \frac{s^2LC}{D'^2}\right) + gV\left(1 - \frac{sL}{RD'^2}\right)} \tag{4.26}$$

The locations of the closed-loop poles as g increases from 0 to ∞ are shown in the root-locus plot of Fig. 4.10.

For the element values of the circuit in Sec. 4.2, it can be shown that the root locus is always the type of Fig. 4.10(b) regardless of the value of ω_1. A typical design is to choose a low frequency $\omega_1/2\pi$=5Hz. Figure 4.11 shows the asymptotes of the closed-loop line rejection eq. (4.26) for g=1, g=0.5, and g=0.2. It is seen that as g increases, the poles move toward the imaginary axis, producing a high Q pair which exhibits a high peak in the line rejection function. For g=0.2 the line rejection eq. (4.26) becomes

$$\frac{\hat{v}}{\hat{v}_g} = \frac{1 + \frac{s/2\pi}{5Hz}}{6.5\left(1 + \frac{s/2\pi}{67Hz}\right)\left[1 + \frac{1}{2.0}\left(\frac{s/2\pi}{815Hz}\right) + \left(\frac{s/2\pi}{815Hz}\right)^2\right]} \tag{4.27}$$

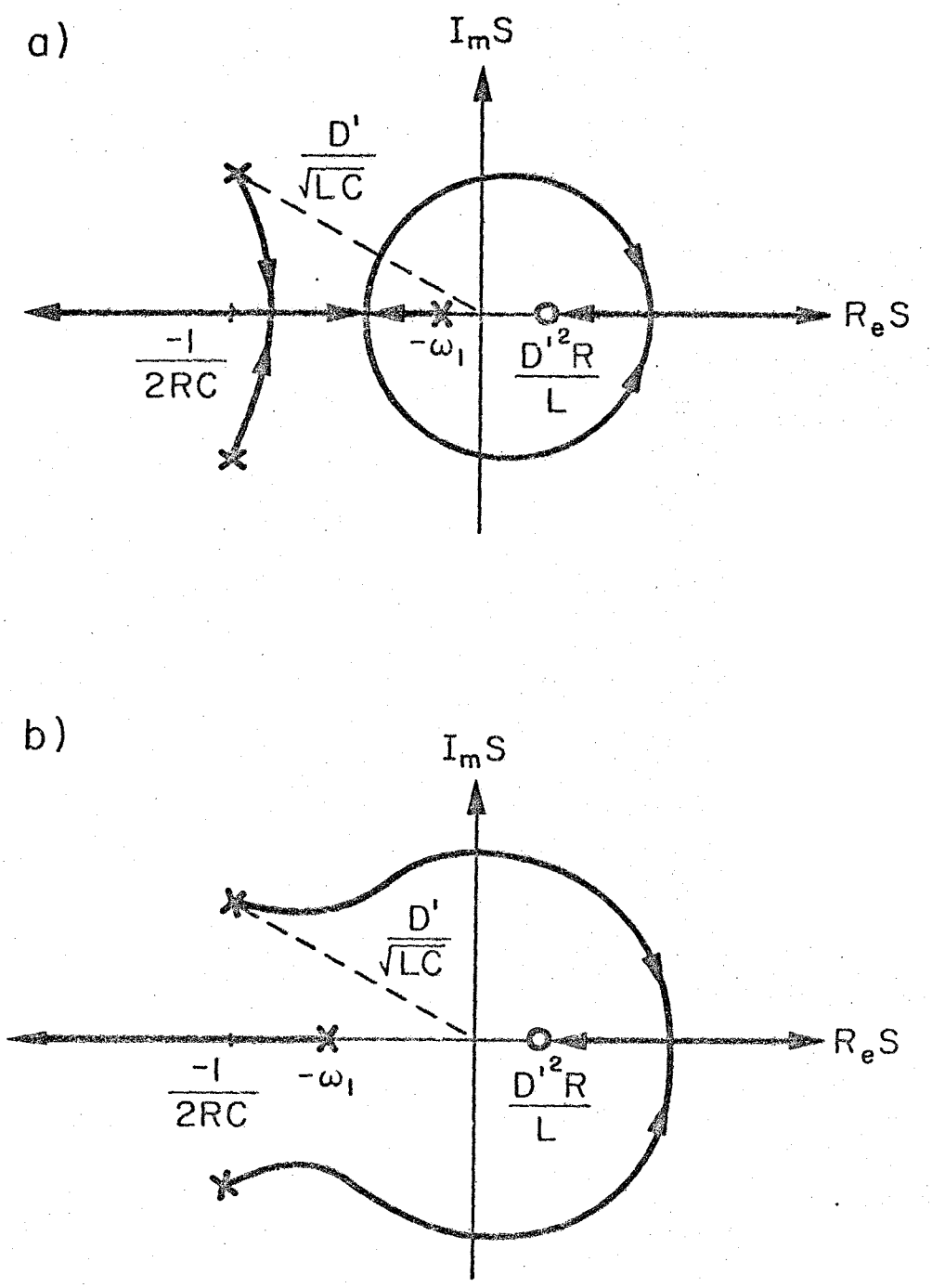

Fig. 4.10 Possible root loci when the single-pole compensation technique is applied to a boost regulator.

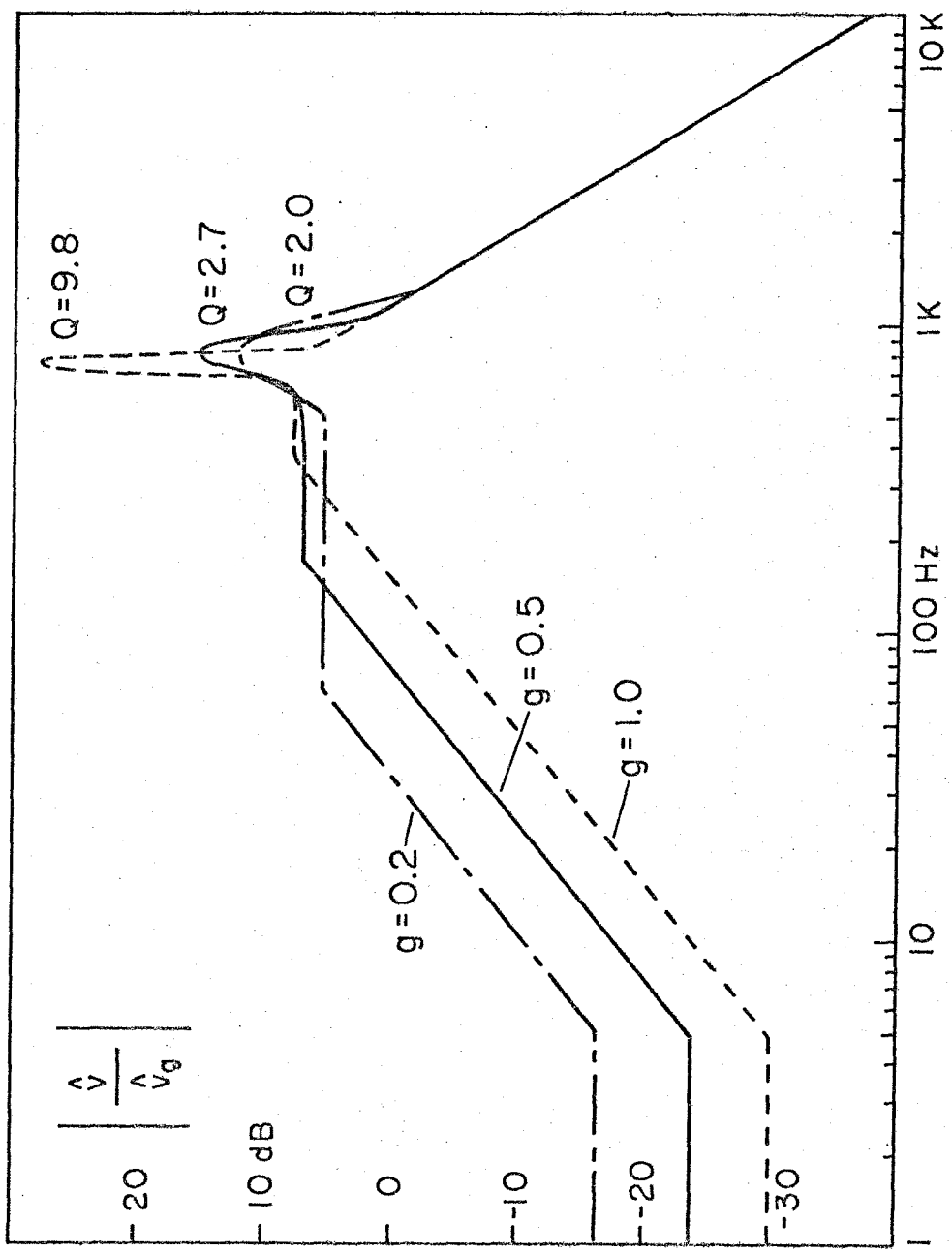

Fig. 4.11 Predicted line rejection of the boost regulator compensated by the single-pole technique.

The closed-loop poles are

$$s = -424, \quad -1256 \pm 4967j \text{ sec}^{-1} \tag{4.28}$$

The transient response is dominated by the single pole which has a time constant of 2.4 msec. Apparently, the design in Sec. 4.2 has better stability margin, transient response and line rejection. The pole locations of these two designs are summarized in Fig. 4.12.

The comparison between the pole placement technique and the single-pole compensation method can be better understood from the root-locus plot of Fig. 4.10(b). As feedback gain g increases, the complex closed-loop pole pair move toward the imaginary axis from their open-loop pole positions, which means the closed-loop poles always have a higher Q than the open-loop poles. The Q increases with the feedback gain g. The static regulation is improved with high feedback gain, but the resultant high Q means less stability margins and higher peak on the line rejection function. The transient response is dominated by the low-frequency single pole when the feedback gain is low, and is taken over by the complex high-Q pole pair as the feedback gain increases. But the negative real part of the dominating pole, which determines the speed of the transient, is always smaller than that of the open-loop pole pair. In other words, the speed of the transient response and the Q value of the complex pole pair are limited by the open-loop pole positions. In contrast to this, the pole placement technique eliminates the limit imposed by the open-loop poles. The closed-loop poles can be assigned anywhere desired on the s-plane regardless

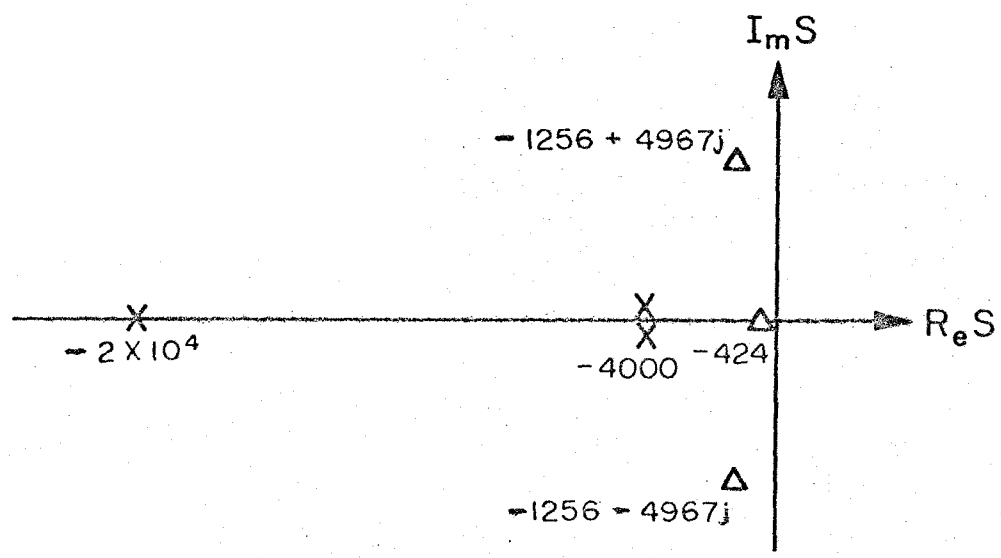

Fig. 4.12 Closed-loop pole positions using the total-state feedback technique vs. the single-pole compensation technique.

of the positions of the open-loop poles.

One common problem encountered in the design of a switching regulator is that the user may add an extra capacitor to the output of the switching regulator. This effectively changes the positions of the poles of the system. If the size of this extra capacitor is too large, the system may be unstable. For example, in the design of eq. (4.27) with g=0.2, the system will be unstable if an extra capacitor of 30 μF or larger is added to the output, according to eq.(4.26). However, this phenomenon does not exist in the design of Sec. 4.2. With the component values used and the feedback gain chosen in Sec. 4.2, eq. (4.10) predicts that the system will be stable regardless of the size of the capacitor. This is because of the large stability margins reserved in that particular design, and also because of the fact that in a multiple-state feedback system, the feedback from the output voltage constitutes only part of the loop gain, but not the entire loop gain. The breadboard of Sec. 4.2 has been working successfully with an extra 100 μF added to the output. It did not pass the test when another 100 μF was added because the stability margin of the system was too small to be practical. The performances of the two designs are summarized in Table 4.1.

	Pole-placement technique ($f_1 = 0$)	Single-pole compensation ($g = 0.2$)
Closed-loop poles	$-4000, -4000, -2\times10^4$ sec^{-1}	$-424, -1256\pm4967j$ sec^{-1}
Dominant transient time constant	250 μs	2.4 ms
Static line regulation	$-\infty$ (theoretical)	-16.3 dB
Peak of line rejection	+2.4 dB	+13.5 dB
Bandwidth of loop gain	4.0 kHz	60 Hz
Max. external capacitor	∞ (theoretical) 100μF (tested)	30μF (theoretical)

Table 4.1 Summary of the performances of the boost regulator example using pole placement technique and single-pole compensation technique.

CHAPTER 5

CONCLUSIONS

The state-space averaging method has been demonstrated in various papers as a useful tool to obtain a set of linear time-invariant differential equations which describes the dynamics of any switching dc-to-dc converter around its operating point [1-10]. The standard analytical tools for linear systems can then be applied to the linearized system to study the stability, small-signal transient responses, and various transfer functions of the converter.

In this part of the thesis, the pole placement technique was used along with the state-space averaging method to assign closed-loop poles of any switching regulator at the desired locations on the s-plane. The advantage of this method over the conventional single-loop design is that the locations of the closed-loop poles are no longer constrained on the root loci between the open-loop poles and zeros. The result is that the stability margins and the transient responses can be shaped and controlled as desired. The enlarged stability margins and the less sensitivity to the output voltage loop gain are appreciated when an extra capacitor is added to the output by the user.

One limitation of this method is that the dc level of the line rejection of the regulator depends on the feedback gains and cannot be independently placed as desired, since the feedback gains are also determined from the considerations of the stability and transient responses. In the cases of boost, buck-boost, and Ćuk converters,

there exists a right half-plane zero in the control-to-output transfer function. In order to stabilize the systems, the pole placement technique depends heavily on the feedbacks from those states which tend to bring the poles to the left half-plane, such as the input inductor current. Unfortunately, the feedback from these states tend to degrade the line rejection. In the case of the Ćuk converter, this problem can be overcome by properly damping the converter as discussed in [10]. The relative weights of feedback from the input states will then be reduced. Sensing the source voltage to control the duty ratio is one way to improve the line rejection. In the case of the buck converter, feedback from the source voltage can be properly chosen to completely null out, around the operating point, the line effect on the output voltage.

Another potential problem of this method is that the sensitivity of the pole positions on the feedback gains may be large because the pole positions may be determined by the small difference between two large gains. A sensitivity study has to be performed in practical applications. Also, since the state-space averaging method is accurate only for small variations around the operating point, the regulator performances have to be checked for extreme operating conditions.

PART II

TRANSFORMER MODELLING

CHAPTER 6

INTRODUCTION

Transformers and coupled inductors are among the most important components in the field of Power Electronics. They are used for isolation, energy transfer and power splitting in almost every power processing circuit. Unfortunately, an ideal transformer or coupled inductor is impossible to build. Magnetic leakages always exist between the windings and the magnetic core. Usually these leakages have adverse effects on the circuit performance and produce high stress on the other components in the circuit. But they can also be used wisely to steer the switching ripple away from the input or output current in a Ćuk converter [14]. A good understanding of transformer modelling is thus necessary to the analysis of power converters and inverters.

For decades, two-winding transformers and coupled inductors have been modelled by the π-model which consists of an ideal transformer with effective turns ratio in the center, a magnetizing inductance in parallel with it, and one leakage inductance on each winding. A similar model can be used for three-winding transformers [16]. Since this model is simple and convenient, it should be used whenever applicable. It will be shown in the subsequent chapters that this π-model is actually under-determined for two-winding transformers, uniquely-determined for three-winding transformers, and over-determined for four-winding transformers. This means that the model can be used for two-winding and three-

winding transformers, but only under special cases can it be used for four-winding transformers. A general model, which models an arbitrary n-winding transformer, exists. But it is too complicated to be of help in physical interpretation.

For many years, the elements in the π-model have been expressed in terms of the standard coupled-inductor coefficients L_{11}, M_{12}, L_{22} etc. In this work, they are expressed in terms of the permeances of the associated magnetic flux paths. In transformers and coupled inductors, magnetic flux paths can be artificially decomposed into flux components and each component has an associated permeance. If the elements in the transformer model are expressed in terms of the permeances, close relations between the model and the physical layout of the transformer windings are preserved. This makes it possible to expose explicitly the physical meaning of each element in the model and a better understanding of the transformer is obtained. For example, it is observed that each leakage inductance of a three-winding transformer is not only a function of the physical tightness of that winding itself to the core, but is also a function of the coupling between the other two windings and their relative positions to the first one. The effects of the leakage fluxes on the effective turns ratio of a three winding transformer are also explicitly represented in the model.

Two-winding, three-winding and four-winding transformer modelling are discussed in the subsequent chapters. In all these cases, the core loss is neglected to linearize the B-H loop.

Interwinding capacitances are not included. Some examples and applications of the models are given in Chapter 10.

CHAPTER 7

TWO-WINDING TRANSFORMER MODELLING

Consider a two-winding transformer with currents flowing in both windings. A typical resultant field map is shown on the left side of Fig. 7.1. For the purpose of analysis, the flux per turn linked by each winding can be decomposed into two artificial components: (1) a mutual flux ϕ, which links both windings, and (2)leakage fluxes $\phi_{\ell 1}$ and $\phi_{\ell 2}$ which only link one winding, as shown in Fig. 7.1.

Under this decomposition,

$$\phi_1(t) = \phi(t) + \phi_{\ell 1}(t) \tag{7.1}$$

$$\phi_2(t) = \phi(t) + \phi_{\ell 2}(t) \tag{7.2}$$

By Faraday's law,

$$v_1 = n_1\dot{\phi}_1 = n_1(\dot{\phi}+\dot{\phi}_{\ell 1}) \tag{7.3}$$

$$v_2 = n_2\dot{\phi}_2 = n_2(\dot{\phi}+\dot{\phi}_{\ell 2}) \tag{7.4}$$

Since the leakage flux is in the air for a considerable portion of the length of its path, it is almost directly proportional to the current producing it, i.e.,

$$\phi_{\ell 1} = p_1 n_1 i_1 \tag{7.5}$$

$$\phi_{\ell 2} = p_2 n_2 i_2 \tag{7.6}$$

The mutual flux is mostly confined inside the core, so

$$\begin{cases} \phi = B\cdot A_c & (7.7) \\ H\cdot \ell_m = n_1 i_1 + n_2 i_2 & (7.8) \end{cases}$$

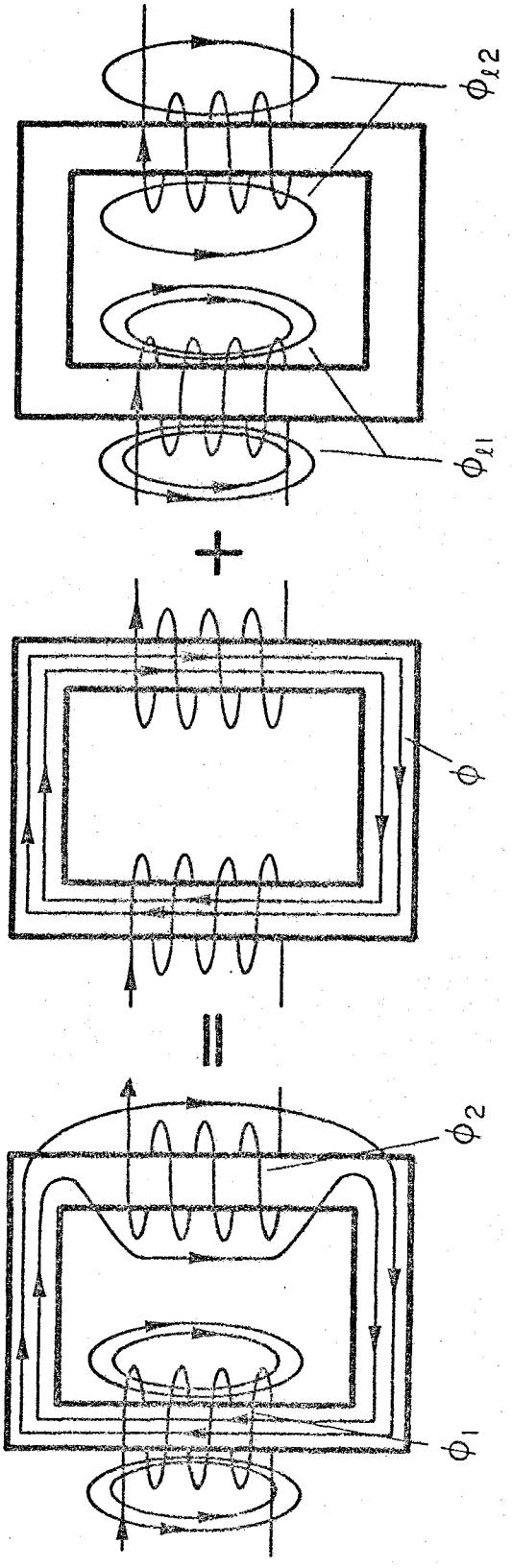

Fig. 7.1 Decomposition of magnetic flux in a two-winding transformer.

If the core loss is neglected, and the B-H loop is assumed to be linear as shown in Fig. 7.2, then

$$B = \mu H \tag{7.9}$$

Equations (7.7), (7.8) can then be combined to relate the mutual flux to the currents:

$$\phi = p_m(n_1 i_1 + n_2 i_2) \tag{7.10}$$

where

$$p_m = \frac{\mu \cdot A_c}{\ell_m}$$

The coefficients p_1, p_2, p_m are the permeances of the associated magnetic paths. The permeance relates the flux per turn to the currents producing the flux. Thus, it has the meaning of inductance per turn for that particular magnetic flux component.

Substituting eqs. (7.5), (7.6), and (7.10) into eqs. (7.3), (7.4), we have

$$v_1 = L_{11}\dot{i}_1 + M_{12}\dot{i}_2 \tag{7.11}$$

$$v_2 = M_{12}\dot{i}_1 + L_{22}\dot{i}_2 \tag{7.12}$$

where

$$L_{11} = n_1^2(p_1 + p_m) \tag{7.13}$$

$$L_{22} = n_2^2(p_2 + p_m) \tag{7.14}$$

$$M_{12} = n_1 n_2 p_m \tag{7.15}$$

An equivalent circuit, or the π-model, that corresponds to eqs. (7.11), (7.12) is given in Fig. 7.3. The π-model is composed of an ideal transformer of effective turns ratio A in the center,

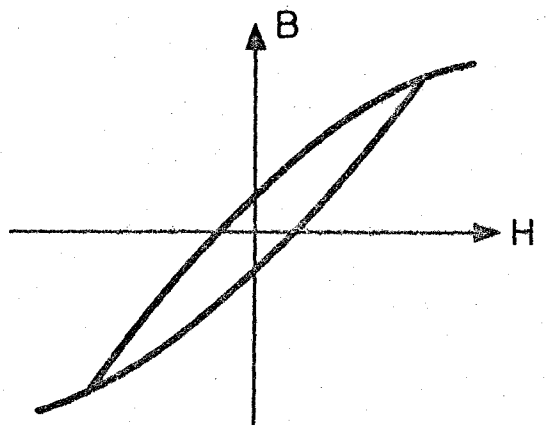

(a) actual

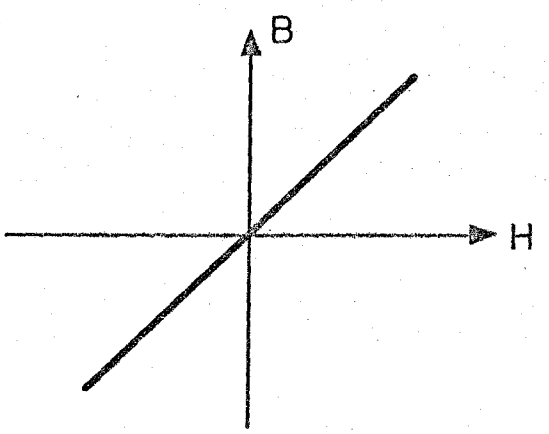

(b) linear approximation

Fig. 7.2 Linear assumption on the B-H loop of a magnetic core.

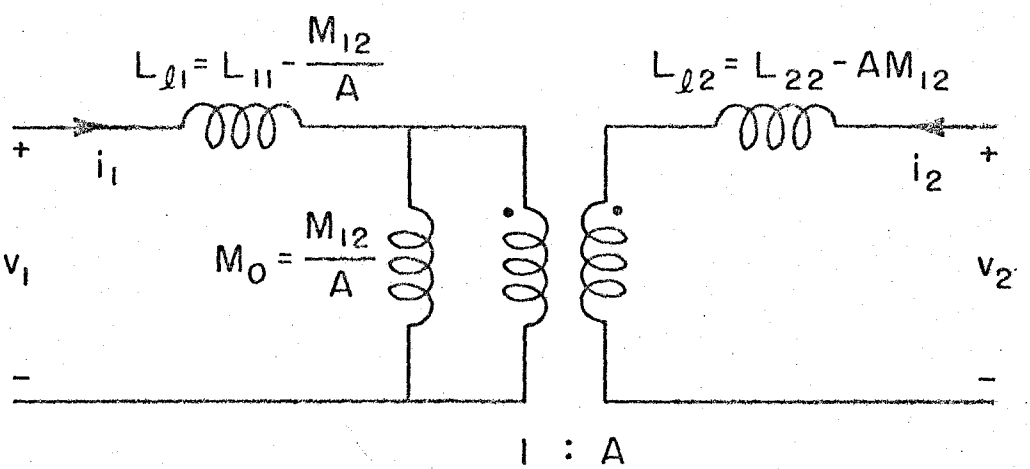

Fig. 7.3 The π-model for a two-winding transformer.

a magnetizing inductance M_0 in parallel with it, and leakage inductances $L_{\ell 1}$, $L_{\ell 2}$ on the two windings. Since there are four parameters in the model but there are only three constants L_{11}, L_{22}, and M_{12} in eqs. (7.11), (7.12), the model is actually underdetermined and the turns ratio A can be chosen arbitrarily. The arbitrary choice of A corresponds to some artificial manipulation of the flux components. For example, the leakage flux in winding 1 can be reduced by decreasing A. Since the mutual flux will increase by the same amount, the flux sensed by winding 1 will remain the same. The increased mutual flux will not affect the total flux sensed by winding 2 because the effective turns ratio and the leakage flux on the secondary can be changed accordingly.

Although the turns ratio A can be chosen arbitrarily, it is most natural to choose $A = n_2/n_1$ so that the model is closely related to the physical transformer. The model parameters expressed in terms of permeances under such a choice of A are shown in Fig. 7.4. It is seen that the leakage and the mutual inductances are just n^2 times the associated permeances which have the meaning of inductance per turn.

If the core is made of ungapped square-loop material, the magnetizing current is usually negligible compared with the current flowing in any of the windings. In this case, the B-H loop can be assumed to be a vertical line through the origin. In other words, $\mu \to \infty$ or $p_m \to \infty$, and the model is reduced to that in Fig. 7.5. Note that in general, there are infinite choices of models because A is

arbitrary. However, in the ungapped case, there is no other choice since $p_m \to \infty$.

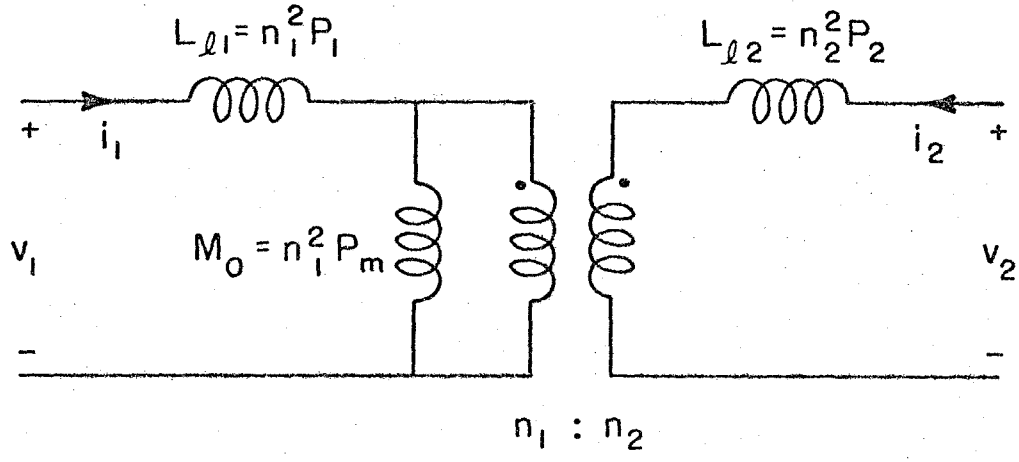

Fig. 7.4 The π-model expressed in terms of permeances, with choice $A = n_2/n_1$.

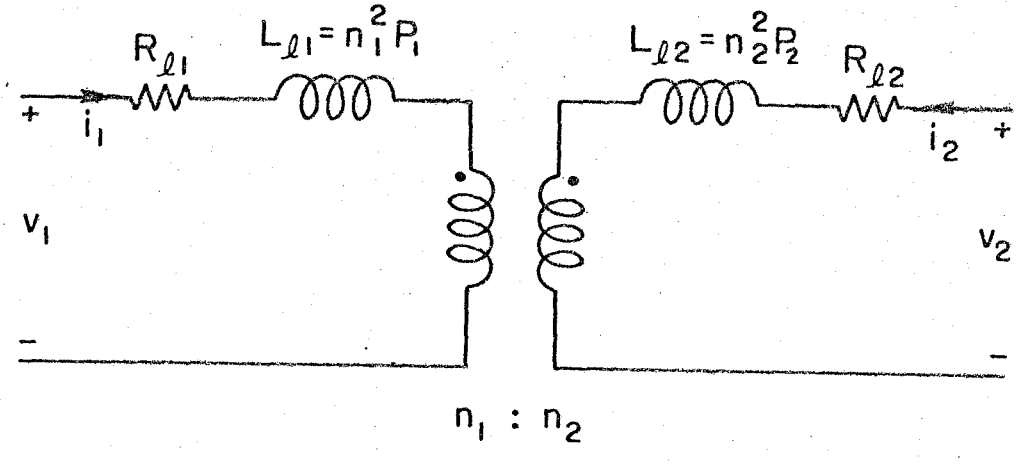

Fig. 7.5 The π-model for an ungapped square loop material transformer with winding resistances included.

CHAPTER 8

THREE-WINDING TRANSFORMER MODELLING

The procedures used in two-winding transformers are now used to model three-winding transformers. The voltages and currents are related by the standard coupled-inductor equations but all the coefficients L_{11}, M_{12}, L_{22}, etc. are expressed in terms of the associated permeances. The π-model corresponding to the standard coupled-inductor equations can then be related to the permeances.

In a three-winding transformer, the flux per turn can be decomposed into seven components: one mutual flux ϕ which links all three windings, three leakage fluxes, ϕ_{12}, ϕ_{23}, ϕ_{13} which link only two windings, and three leakage fluxes, $\phi_{\ell 1}$, $\phi_{\ell 2}$, $\phi_{\ell 3}$ which only link one winding. The components are shown in Fig. 8.1. By Faraday's law:

$$v_1 = n_1(\dot{\phi} + \dot{\phi}_{12} + \dot{\phi}_{13} + \dot{\phi}_{\ell 1}) \tag{8.1}$$

$$v_2 = n_2(\dot{\phi} + \dot{\phi}_{12} + \dot{\phi}_{23} + \dot{\phi}_{\ell 2}) \tag{8.2}$$

$$v_3 = n_3(\dot{\phi} + \dot{\phi}_{13} + \dot{\phi}_{23} + \dot{\phi}_{\ell 3}) \tag{8.3}$$

Since the leakage fluxes have most of their paths in the air, they can be assumed to be proportional to the currents producing them:

$$\phi_{\ell 1} = p_1 n_1 i_1 \tag{8.4}$$

$$\phi_{\ell 2} = p_2 n_2 i_2 \tag{8.5}$$

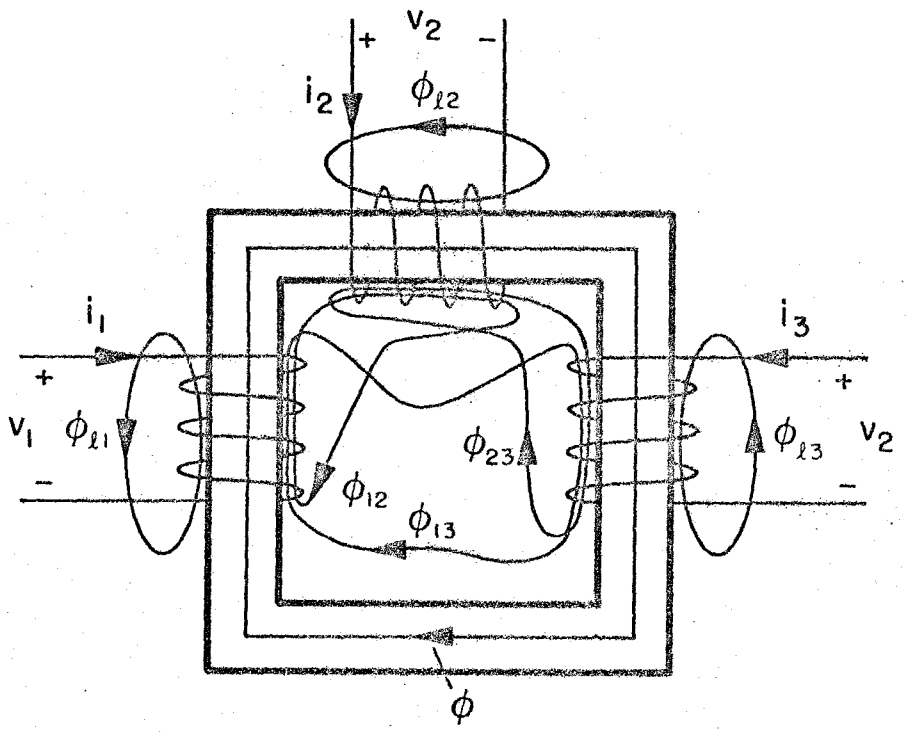

Fig. 8.1 The seven flux components in a three-winding transformer.

$$\phi_{\ell 3} = p_3 n_3 i_3 \tag{8.6}$$

$$\phi_{12} = p_{12}(n_1 i_1 + n_2 i_2) \tag{8.7}$$

$$\phi_{23} = p_{23}(n_2 i_2 + n_3 i_3) \tag{8.8}$$

$$\phi_{13} = p_{13}(n_1 i_1 + n_3 i_3) \tag{8.9}$$

The mutual flux is mostly confined inside the core, thus

$$\begin{cases} \phi = B \cdot A_c & (8.10) \\ H \cdot \ell_m = n_1 i_1 + n_2 i_2 + n_3 i_3 & (8.11) \end{cases}$$

If the core is linear, i.e.,

$$B = \mu H \tag{8.12}$$

then

$$\phi = p_m(n_1 i_1 + n_2 i_2 + n_3 i_3) \tag{8.13}$$

where

$$p_m \equiv \mu \cdot A_c / \ell_m$$

To find an equivalent circuit model in terms of permeance, the voltages across the three windings will first be put in the standard coupled-inductor form. The π-model can be easily derived from these equations. The permeances can then be substituted into the elements of the model. From eqs. (8.1) through (8.9) and (8.13)

$$v_1 = L_{11}\dot{i}_1 + M_{12}\dot{i}_2 + M_{13}\dot{i}_3 \tag{8.14}$$

$$v_2 = M_{12}\dot{i}_1 + L_{22}\dot{i}_2 + M_{23}\dot{i}_3 \tag{8.15}$$

$$v_3 = M_{13}\dot{i}_1 + M_{23}\dot{i}_2 + L_{33}\dot{i}_3 \tag{8.16}$$

where

$$L_{11} = n_1^2(p_m + p_{12} + p_{13} + p_1) \tag{8.17}$$

$$L_{22} = n_2^2(p_m + p_{12} + p_{23} + p_2) \tag{8.18}$$

$$L_{33} = n_3^2(p_m + p_{13} + p_{23} + p_3) \tag{8.19}$$

$$M_{12} = n_1 n_2(p_m + p_{12}) \tag{8.20}$$

$$M_{23} = n_2 n_3(p_m + p_{23}) \tag{8.21}$$

$$M_{13} = n_1 n_3(p_m + p_{13}) \tag{8.22}$$

The π-equivalent circuit model corresponding to eqs. (8.14), (8.15), and (8.16) is shown in Fig. 8.2 [16]. Again, the π-model has an ideal transformer with effective turns ratios A and B in the center, a magnetizing inductance M_o in parallel with it, and one leakage inductance on each winding. By comparison of the model of Fig. 8.2 with eqs. (8.14), (8.15), and (8.16), the unique solutions for the six unknowns are

$$L_{\ell 1} = L_{11} - M_{12}M_{13}/M_{23} \tag{8.23}$$

$$L_{\ell 2} = L_{22} - M_{12}M_{23}/M_{13} \tag{8.24}$$

$$L_{\ell 3} = L_{33} - M_{23}M_{13}/M_{12} \tag{8.25}$$

$$M_o = M_{12}M_{13}/M_{23} \tag{8.26}$$

$$A = M_{23}/M_{13} \tag{8.27}$$

$$B = M_{23}/M_{12} \tag{8.28}$$

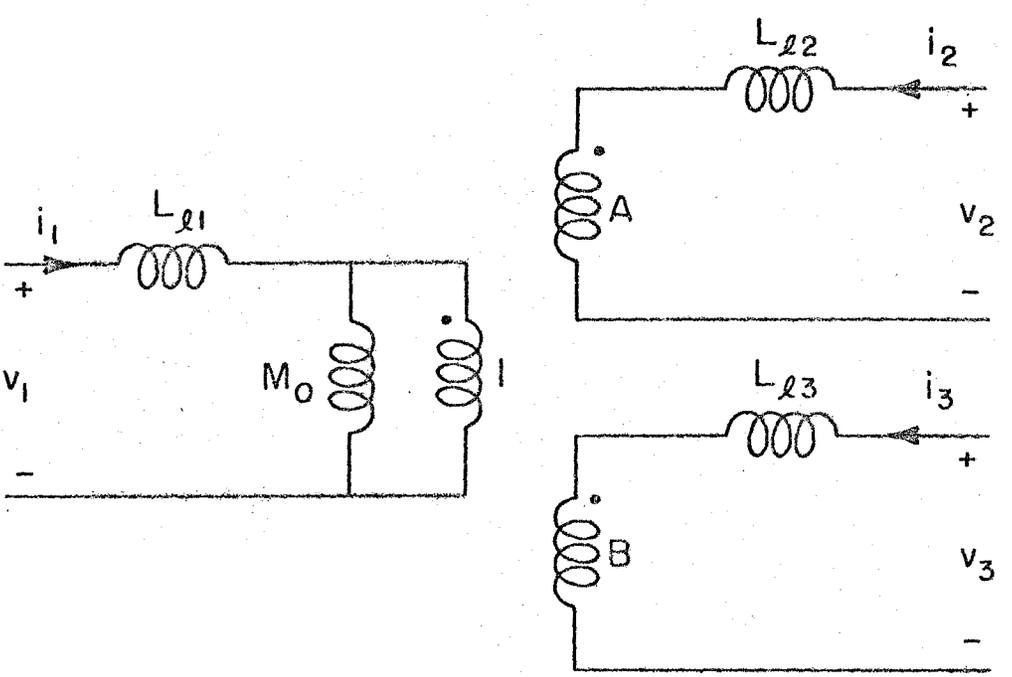

Fig. 8.2 The π-model for a three-winding transformer.

Substitution of eqs. (8.17) through (8.22) into (8.23) through (8.28) leads to

$$L_{\ell 1} = n_1^2[(p_1+p_{23})p_m + p_{23}(p_1+p_{12}+p_{13}) - p_{12}p_{13}] \,/\, (p_m+p_{23})$$

$$\simeq n_1^2(p_1+p_{23}) \tag{8.29}$$

$$L_{\ell 2} = n_2^2[(p_2+p_{13})p_m + p_{13}(p_2+p_{12}+p_{23}) - p_{23}p_{12}] \,/\, (p_m+p_{13})$$

$$\simeq n_2^2(p_2+p_{13}) \tag{8.30}$$

$$L_{\ell 3} = n_3^2[(p_3+p_{12})p_m + p_{12}(p_3+p_{13}+p_{23}) - p_{13}p_{23}] \,/\, (p_m+p_{12})$$

$$\simeq n_3^2(p_3+p_{12}) \tag{8.31}$$

$$M_o = n_1^2(p_m+p_{12})(p_m+p_{13}) \,/\, (p_m+p_{23})$$

$$\simeq n_1^2 p_m \tag{8.32}$$

$$A = (n_2/n_1)(p_m+p_{23}) \,/\, (p_m+p_{13}) \tag{8.33}$$

$$B = (n_3/n_1)(p_m+p_{23}) \,/\, (p_m+p_{12}) \tag{8.34}$$

The results are summarized in Fig. 8.3.

If the core is made of ungapped square loop material, $\mu \to \infty$, or $p_m \to \infty$, the model is then reduced to that in Fig. 8.4.

The effective turns ratio of the π-model in Fig. 8.3 can be understood by the following argument. Consider the case when both winding 1 and winding 2 are open circuit and only the third winding is carrying the current. The ratio of the open-circuit voltages measured at winding 2 and winding 1 is clearly the effective turns

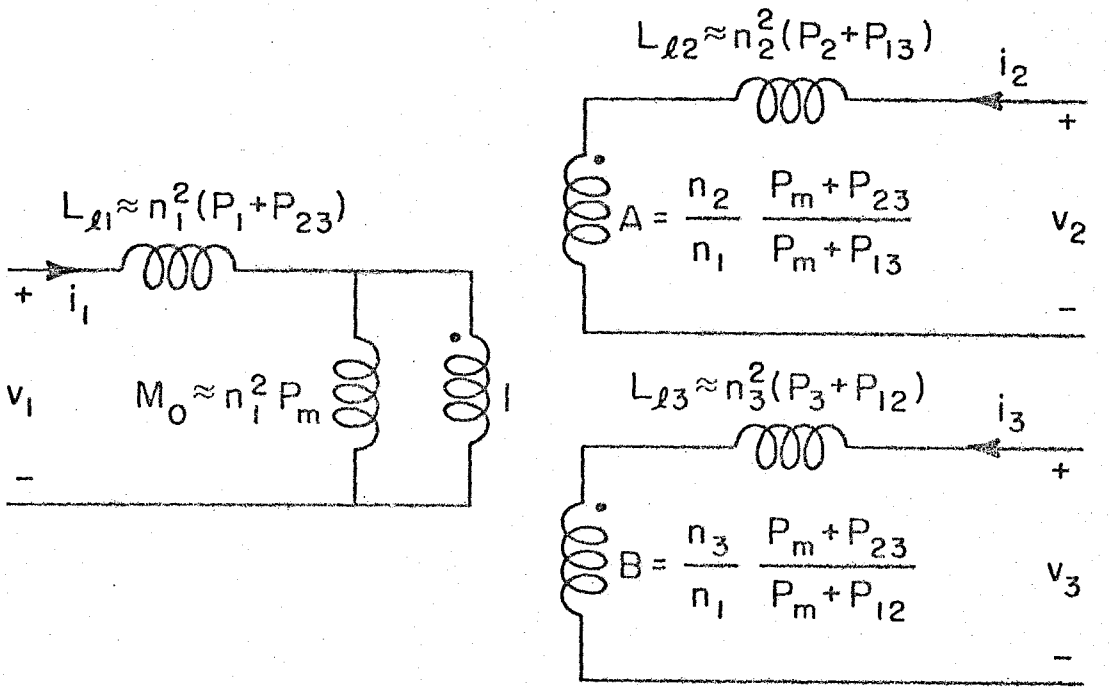

Fig. 8.3 The π-model for a three-winding transformer, expressed in terms of permeances.

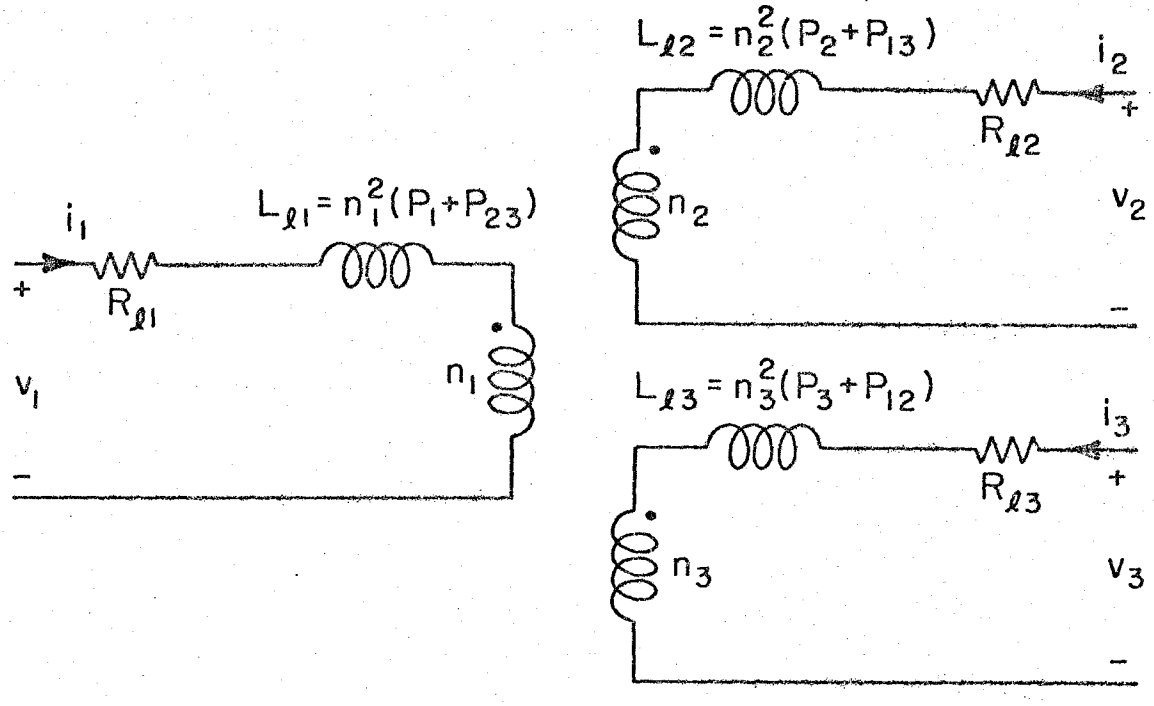

Fig. 8.4 The π-model for a three-winding transformer, with magnetizing current neglected.

ratio A. From the flux map in Fig. 8.5, it is easy to see that the effective turns ratio A is equal to $(n_2/n_1)(p_m+p_{23})/(p_m+p_{13})$. The physical turns ratio n_2/n_1 is corrected by the relative size of the partial leakages p_{23} and p_{13} to the mutual permeance p_m.

The leakage inductance on winding 1 is

$$L_{\ell 1} \approx n_1^2(p_1+p_{23}) \tag{8.29}$$

The contribution from p_1 is easy to understand because it is proportional to the flux which flows only in winding 1 without coupling to any other winding. However, the contribution from p_{23} is not so obvious, because p_{23} is a measure of the coupling between the windings 2,3 and the core, and it seems as though it has nothing to do with the coupling between winding 1 and the core. Nevertheless, the total flux $\phi+\phi_{12}+\phi_{13}+\phi_{\ell 1}$ sensed by winding 1 can be thought of as a new mutual flux ϕ' plus $n_1^2(p_1+p_{23})i_1$ if the magnetizing current $n_1i_1+n_2i_2+n_3i_3$ is small compared with the current on any of the windings. Thus, the term $n_1^2(p_1+p_{23})$ becomes the effective leakage in winding 1. The detailed manipulation is shown in the following. With use of the assumption

$$n_1i_1 + n_2i_2 + n_3i_3 = 0 \tag{8.35}$$

$$\begin{aligned}
\phi_1 &= n_1 (\phi + \phi_{12} + \phi_{13} + \phi_{\ell 1}) \\
&= n_1 [\phi + p_{12}(n_1i_1+n_2i_2) + p_{13}(n_1i_1+n_3i_3) + p_1n_1i_1] \\
&= n_1 [\phi - p_{12}n_3i_3 - p_{13}n_2i_2 - p_{23}n_1i_1] + n_1^2(p_1+p_{23})i_1 \\
&= n_1\phi' + n_1^2(p_1+p_{23})i_1
\end{aligned} \tag{8.36}$$

where $\phi' = \phi - p_{12}n_3i_3 - p_{13}n_2i_2 - p_{23}n_1i_1$

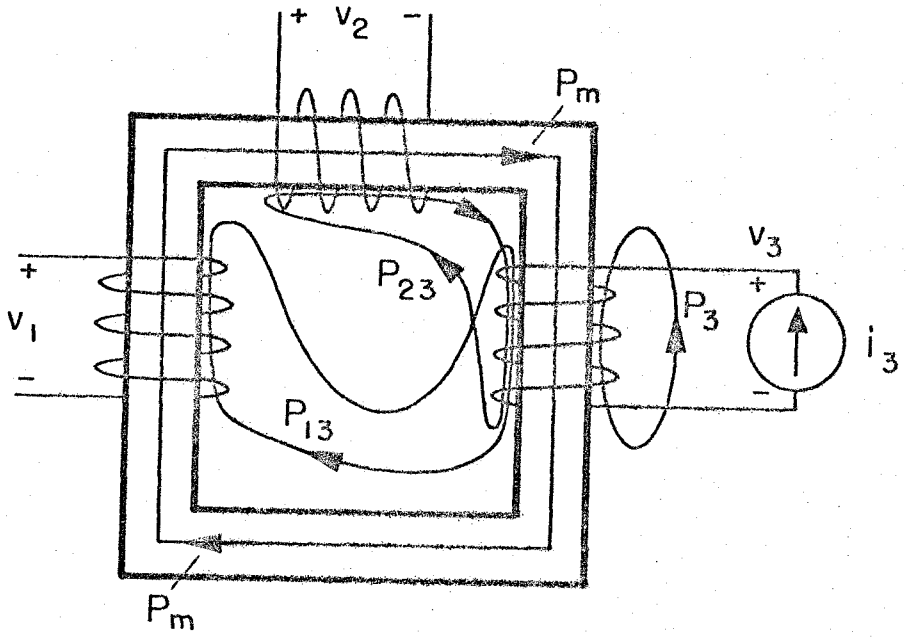

Fig. 8.5 The effective turns ratio between winding 1 and 2 can be easily interpreted by considering the flux components passing through winding 1 and 2.

Similarly

$$\phi_2 = n_2\phi' + n_2^2(p_2+p_{13})i_2 \tag{8.37}$$

$$\phi_3 = n_3\phi' + n_3^2(p_3+p_{12})i_3 \tag{8.38}$$

Notice that ϕ' is common to all three windings, thus it can be thought of as the new mutual flux.

The effect of p_{23} on the leakage in winding 1 is demonstrated in the example of Sec. 10.1 where it is shown that even though the transformer winding 1 is closely wound around the core, the effective leakage on winding 1 can vary drastically depending on the winding geometry of windings 2 and 3.

Note that, in the three-winding transformer model, the magnetizing inductance can be reflected to any of the three windings but, unlike the case of the two-winding model, the leakage inductance cannot be reflected to the other windings.

The six parameters $L_{\ell 1}$, $L_{\ell 2}$, $L_{\ell 3}$, M_o, A, B in the three winding π-model as shown in Fig. 8.3 can be derived from the following measurements.

(1) With use of a network analyzer, inject a voltage at winding 3 and measure the open-circuit voltage at winding 2 with respect to the open-circuit voltage at winding 1. The reading on the analyzer is the value of the turns ratio A. A similar measurement gives the turns ratio B.

(2) With use of the network analyzer and a current probe, measure the impedance looking into winding 1 with the other two windings

open. This gives $s(L_{\ell 1}+M_o)$.

(3) Measure the impedance looking into winding 1 with winding 2 open and winding 3 shorted. Theis gives

$$s\left\{ L_{\ell 1} + [M_o \,//\, (L_{\ell 3}/B^2)] \right\}$$

Similar measurements give

$$s\left\{ L_{\ell 1} + [M_o \,//\, (L_{\ell 2}/A^2)] \right\}$$

and

$$s\left\{ L_{\ell 2} + A^2(M_o \,//\, (L_{\ell 3}/B^2)] \right\}$$

These four data can be used to calculate $L_{\ell 1}$, $L_{\ell 2}$, $L_{\ell 3}$ and M_o.

The network analyzer has to be zeroed before the measurement of turns ratio. The frequency for the measurement of impedance has to be high enough that the winding resistances are negligible, and low enough that the effect of interwinding capacitance is very small.

Similar methods can also be applied to the two-winding π-model, except that a specific turns ratio has to be chosen before the values of other parameters can be assigned.

If the mutual inductance were neglected in the model, the three impedance measurements in step (3) can still be used to determine the three leakage inductances. However, in the case of the two-winding transformer, it is impossible to separate the leakage inductances from their reflected sum when the magnetizing inductance is neglected.

CHAPTER 9

FOUR-WINDING TRANSFORMER MODELLING

The same procedures used in three-winding transformer modelling are used in this chapter to model the four-winding transformer. But it will be found that the π-model is over-determined, and only in special cases can it be used.

In a four-winding transformer, the flux per turn can be decomposed into 15 components: one mutual flux ϕ which links all four windings, four fluxes ϕ_{123}, ϕ_{234}, ϕ_{134}, ϕ_{124} which link three windings, six fluxes ϕ_{12}, ϕ_{23}, ϕ_{34}, ϕ_{13}, ϕ_{14}, ϕ_{24} which link two windings, and four leakage fluxes $\phi_{\ell 1}$, $\phi_{\ell 2}$, $\phi_{\ell 3}$, $\phi_{\ell 4}$ which link only one winding. Since all the leakage fluxes have most of their paths in the air, they can be assumed to be proportional to the current producing them:

$$\phi_{\ell 1} = p_1 n_1 i_1 \tag{9.1}$$

$$\phi_{\ell 2} = p_2 n_2 i_2 \tag{9.2}$$

$$\phi_{\ell 3} = p_3 n_3 i_3 \tag{9.3}$$

$$\phi_{\ell 4} = p_4 n_4 i_4 \tag{9.4}$$

$$\phi_{12} = p_{12}(n_1 i_1 + n_2 i_2) \tag{9.5}$$

$$\phi_{23} = p_{23}(n_2 i_2 + n_3 i_3) \tag{9.6}$$

$$\phi_{14} = p_{14}(n_1 i_1 + n_4 i_4) \tag{9.7}$$

$$\phi_{13} = p_{13}(n_1 i_1 + n_3 i_3) \tag{9.8}$$

$$\phi_{24} = p_{24}(n_2 i_2 + n_4 i_4) \tag{9.9}$$

$$\phi_{34} = p_{34}(n_3 i_3 + n_4 i_4) \tag{9.10}$$

$$\phi_{123} = p_{123}(n_1 i_1 + n_2 i_2 + n_3 i_3) \tag{9.11}$$

$$\phi_{234} = p_{234}(n_2 i_2 + n_3 i_3 + n_4 i_4) \tag{9.12}$$

$$\phi_{124} = p_{124}(n_1 i_1 + n_2 i_2 + n_4 i_4) \tag{9.13}$$

$$\phi_{134} = p_{134}(n_1 i_1 + n_3 i_3 + n_4 i_4) \tag{9.14}$$

The mutual flux ϕ is mostly confined inside the core, thus

$$\begin{cases} \phi = B \cdot A_c & (9.15) \\ H \cdot \ell_m = n_1 i_1 + n_2 i_2 + n_3 i_3 + n_4 i_4 & (9.16) \end{cases}$$

If the core is linear, i.e.,

$$B = \mu H \tag{9.17}$$

then

$$\phi = p_m(n_1 i_1 + n_2 i_2 + n_3 i_3 + n_4 i_4)$$

where $p_m \equiv \mu \cdot A_c / \ell_m$ (9.18)

By Faraday's law,

$$\begin{aligned} v_1 &= n_1(\dot{\phi}_{\ell 1} + \dot{\phi}_{12} + \dot{\phi}_{13} + \dot{\phi}_{14} + \dot{\phi}_{123} + \dot{\phi}_{124} + \dot{\phi}_{134} + \dot{\phi}) \\ &= L_{11}\dot{i}_1 + M_{12}\dot{i}_2 + M_{13}\dot{i}_3 + M_{14}\dot{i}_4 \end{aligned} \tag{9.19}$$

Similarly,

$$v_2 = M_{12}\dot{i}_1 + L_{22}\dot{i}_2 + M_{23}\dot{i}_3 + M_{24}\dot{i}_4 \tag{9.20}$$

$$v_3 = M_{13}\dot{i}_1 + M_{23}\dot{i}_2 + L_{33}\dot{i}_3 + M_{34}\dot{i}_4 \tag{9.21}$$

$$v_4 = M_{14}\dot{i}_1 + M_{24}\dot{i}_2 + M_{34}\dot{i}_3 + L_{44}\dot{i}_4 \tag{9.22}$$

where

$$L_{11} = (p_m + p_1 + p_{12} + p_{13} + p_{14} + p_{123} + p_{124} + p_{134}) n_1^2 \tag{9.23}$$

$$L_{22} = (p_m + p_2 + p_{12} + p_{23} + p_{24} + p_{123} + p_{124} + p_{234}) n_2^2 \tag{9.24}$$

$$L_{33} = (p_m+p_3+p_{13}+p_{23}+p_{34}+p_{123}+p_{134}+p_{234})n_3^2 \tag{9.25}$$

$$L_{44} = (p_m+p_4+p_{14}+p_{24}+p_{34}+p_{124}+p_{134}+p_{234})n_4^2 \tag{9.26}$$

$$M_{12} = n_1n_2\ (p_{12}+p_{123}+p_{124}+p_m) \tag{9.27}$$

$$M_{13} = n_1n_3\ (p_{13}+p_{123}+p_{134}+p_m) \tag{9.28}$$

$$M_{14} = n_1n_4\ (p_{14}+p_{124}+p_{134}+p_m) \tag{9.29}$$

$$M_{23} = n_2n_3\ (p_{23}+p_{123}+p_{234}+p_m) \tag{9.30}$$

$$M_{24} = n_2n_4\ (p_{24}+p_{124}+p_{234}+p_m) \tag{9.31}$$

$$M_{34} = n_3n_4\ (p_{34}+p_{134}+p_{234}+p_m) \tag{9.32}$$

An exact equivalent circuit model can be found for eqs. (9.19) through (9.22) , as shown in Fig. 9.1. The model has an inductance between all the nodes and the ground. The same modelling technique can be extended to arbitrary n [17]. Since there are $n(n+1)/2$ elements in the equivalent circuit model and there are the same number of coefficients in the coupled-inductor equations, the values of the elements in the model can be uniquely determined.

Although this model is exact, it is too complicated to be useful. The measurements of the values of the elements are also difficult. The simple π-model, which ignores most of the inter-dependences between windings, is explored here. The purpose is to find out the conditions under which such a model is applicable. As shown in Fig. 9.2, there are 8 unknowns $L_{\ell 1}$, $L_{\ell 2}$, $L_{\ell 3}$, $L_{\ell 4}$, A, B, C, M_o to be expressed in terms of the 10 known constants: L_{11}, L_{22},

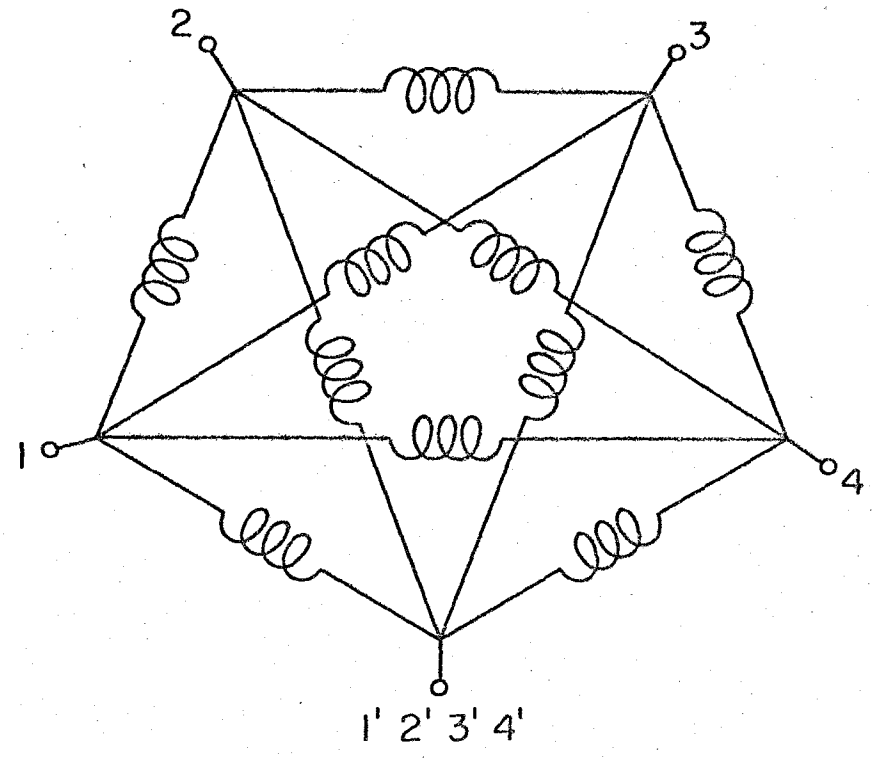

Fig. 9.1 An equivalent circuit model for a four-winding transformer.

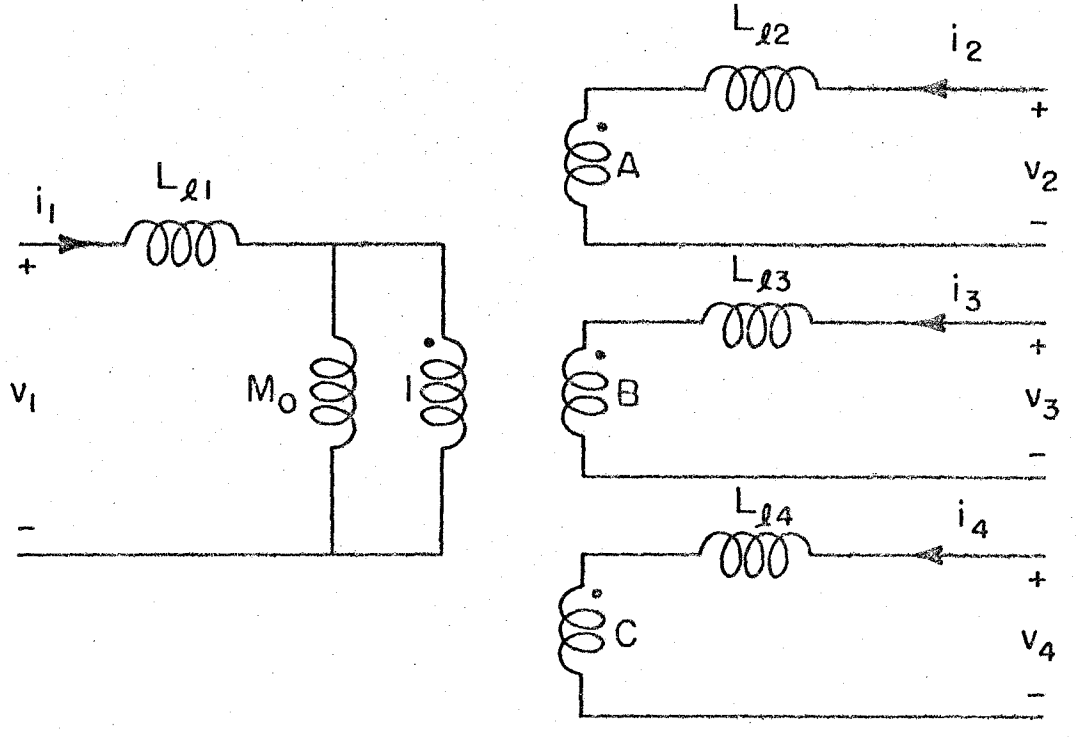

Fig. 9.2 The π-model for a four-winding transformer.

M_{12}, etc. Comparison of Fig. 9.2 with eqs. (9.19) through (9.22) shows that there are 10 equations to be satisfied:

$$L_{\ell 1} + M_o = L_{11} \tag{9.33}$$

$$L_{\ell 2} + A^2 M_o = L_{22} \tag{9.34}$$

$$L_{\ell 3} + B^2 M_o = L_{33} \tag{9.35}$$

$$L_{\ell 4} + C^2 M_o = L_{44} \tag{9.36}$$

$$M_o A = M_{12} \tag{9.37}$$

$$M_o B = M_{13} \tag{9.38}$$

$$M_o C = M_{14} \tag{9.39}$$

$$ABM_o = M_{23} \tag{9.40}$$

$$ACM_o = M_{24} \tag{9.41}$$

$$BCM_o = M_{34} \tag{9.42}$$

In general, there exists no solution to these ten equations unless they are a dependent set. In other words, the π-model is not adequate to represent the four-winding transformer except in certain special cases.

Consider the four unknowns A, B, C, and M_o in the six eqs. (9.37) through (9.42). It is easy to see that unique solutions exist if and only if

$$A : B : C = M_{12} : M_{13} : M_{14} = M_{24} : M_{34} : M_{34}M_{24}/M_{23}$$

or

$$M_{12}M_{34} = M_{13}M_{24} = M_{14}M_{23} \tag{9.43}$$

The unique solution under this assumption is

$$M_o = (M_{12}M_{13}M_{14})^{2/3} \Big/ (M_{23}M_{24}M_{34})^{1/3} \tag{9.44}$$

$$A = M_{12} / M_o \tag{9.45}$$

$$B = M_{13} / M_o \tag{9.46}$$

$$C = M_{14} / M_o \tag{9.47}$$

$$L_{\ell 1} = L_{11} - M_o \tag{9.48}$$

$$L_{\ell 2} = L_{22} - A^2 M_o \tag{9.49}$$

$$L_{\ell 3} = L_{33} - B^2 M_o \tag{9.50}$$

$$L_{\ell 4} = L_{44} - C^2 M_o \tag{9.51}$$

The constraints in eq. (9.43) can be expressed in terms of permeances by substitution of eqs. (9.27) through (9.32) into it:

$$\begin{aligned} &(p_m+p_{12}+p_{123}+p_{124})(p_m+p_{34}+p_{234}+p_{134}) \\ =\ &(p_m+p_{13}+p_{123}+p_{134})(p_m+p_{24}+p_{234}+p_{124}) \\ =\ &(p_m+p_{14}+p_{124}+p_{134})(p_m+p_{23}+p_{234}+p_{123}) \end{aligned} \tag{9.52}$$

or

$$\begin{aligned} &p_m^2 + p_m(p_{12}+p_{34}+p_{123}+p_{124}+p_{134}+p_{234}) + \cdots \\ =\ &p_m^2 + p_m(p_{13}+p_{24}+p_{123}+p_{124}+p_{134}+p_{234}) + \cdots \\ =\ &p_m^2 + p_m(p_{14}+p_{23}+p_{123}+p_{124}+p_{134}+p_{234}) + \cdots \end{aligned} \tag{9.53}$$

i.e.

$$\begin{cases} \text{either} & p_{12}+p_{34} = p_{13}+p_{24} = p_{14}+p_{23} \\ \text{or} & (p_{123}+p_{124}+p_{134}+p_{234}) \text{ dominates } p_{12},\ p_{34},\ p_{13},\ p_{24} \end{cases} \tag{9.54}$$

If eq. (9.43) is satisfied, the eight parameters in the π-model can be expressed in terms of permeances as follows: (with the assumption that p_m >> the rest of the p's)

$$\begin{aligned} M_o &= (M_{12}M_{13}M_{14})^{2/3} \Big/ (M_{23}M_{24}M_{34})^{1/3} \\ &\simeq n_1^2 p_m[1 + (p_{12}+p_{13}-p_{23}+p_{123}+p_{124}+p_{134}-p_{234})/p_m] \\ &\simeq n_1^2 p_m \end{aligned} \tag{9.55}$$

$$A = M_{12}/M_o \simeq (n_2/n_1)[1 + (p_{23}-p_{13}+p_{234}-p_{134})/p_m] \tag{9.56}$$

$$B = M_{13}/M_o \simeq (n_3/n_1)[1 + (p_{23}-p_{12}+p_{234}-p_{124})/p_m] \tag{9.57}$$

$$C = M_{14}/M_o \simeq (n_4/n_1)[1 + (p_{34}-p_{13}+p_{234}-p_{123})/p_m] \tag{9.58}$$

$$L_{\ell 1} = L_{11} - M_o \simeq n_1^2(p_1+p_{234}+p_{14}+p_{23}) \tag{9.59}$$

$$L_{\ell 2} = L_{22} - A^2 M_o \simeq n_2^2(p_2+p_{134}+p_{24}+p_{13}) \tag{9.60}$$

$$L_{\ell 3} = L_{33} - B^2 M_o \simeq n_3^2(p_3+p_{124}+p_{12}+p_{34}) \tag{9.61}$$

$$L_{\ell 4} = L_{44} - C^2 M_o \simeq n_4^2(p_4+p_{123}+p_{24}+p_{13}) \tag{9.62}$$

In other words, the π-model in Fig. 9.3 will be adequate if eq. (9.54) is satisfied.

Under the following conditions, the constraint eq. (9.54) can be considered satisfied.

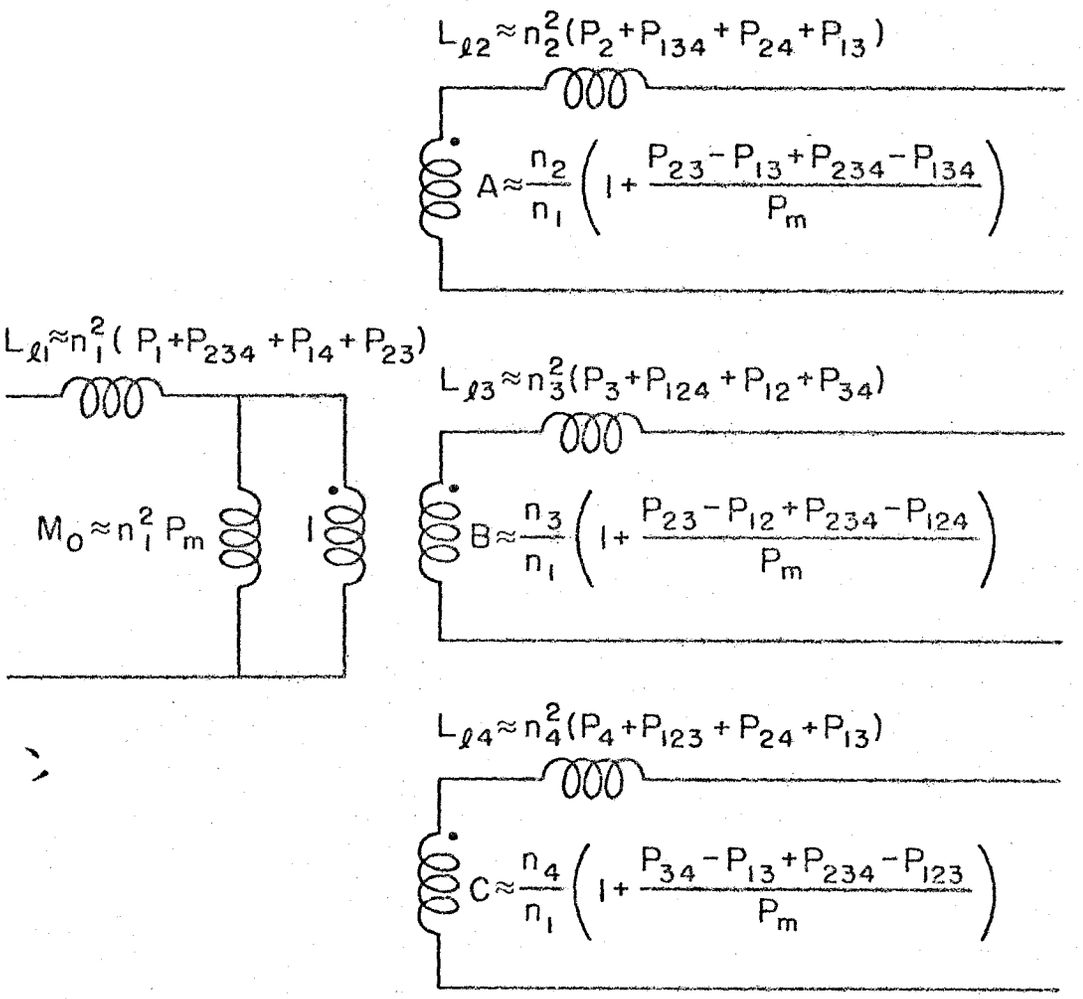

Fig. 9.3 The π-model expressed in terms of the permeances when the constraint (9.54) is satisfied.

(1) If the four windings are wound tetra-filar such that

$$p_{12} = p_{13} = p_{14} = p_{23} = p_{24} = p_{34} \tag{9.63}$$

$$p_{123} = p_{234} = p_{124} = p_{134} \tag{9.64}$$

then the transformer can be modelled by the π-model in Fig. 9.3.

(2) If three windings are wound tri-filar (e.g., windings 1, 2, 3) and the fourth winding is wound alone, then p_{123} and p_4 will dominate the rest of the leakages. In this case, eq. (9.54) will be satisfied and the transformer can be modelled by the π-model in Fig. 9.3.

(3) If the four windings are wound on the four sides of the core, p_1, p_2, p_3, p_4 will dominate the rest of the leakages. In this case, the interdependences become second-order compared with $L_{\ell 1}$, $L_{\ell 2}$, $L_{\ell 3}$, $L_{\ell 4}$, and the π-model in Fig. 9.3 is adequate.

The worst case is when windings 1, 2 are bifilar on one side of the core, and windings 3,4 are bifilar on the other side of the core. In this case, p_{12} and p_{34} dominate the rest of the leakages. Clearly, eq. (9.54) will not be satisfied, the π-model will not be adequate, and strong interdependent terms are expected. A model like the one in Fig. 9.1 has to be used.

CHAPTER 10

EXAMPLES AND APPLICATIONS OF TRANSFORMER MODELS

Some examples are given in this chapter to demonstrate the physical meanings and the applications of the models derived in the previous chapters.

10.1 An example of three-winding transformer modelling

A set of three-winding transformers has been wound to demonstrate the effect of p_{23} on the leakage of winding 1. All three transformers were wound on the Ferroxcube 3019 P-A400-3B7 ferrite pot core with $N_1 = N_2 = N_3 = 30$ turns of #28AWG. The individual differences and experimental data are summarized in Fig. 10.1.

The transformer #1 was wound tri-filar. Any flux which is linked by one winding would be linked by the other two. Therefore, the mutual permeance is the highest among the three transformers, the leakage inductances are all very small, and the effective turns ratios are each virtually unity.

The transformer #2 has all its three windings separated from one another by the blocking tape, but winding 1 is closest to the core. All the six leakage permeances p_1, p_2, p_3, p_{12}, p_{23}, p_{13} are higher than that of the transformer #1, so that the leakage inductances on the three windings are larger and the effective turns-ratios are different from the physical turns ratio 1.0. The mutual flux is smaller than that of transformer #1.

Transformer #3 has its winding 2 and winding 3 wound bifilar.

a) Transformer I

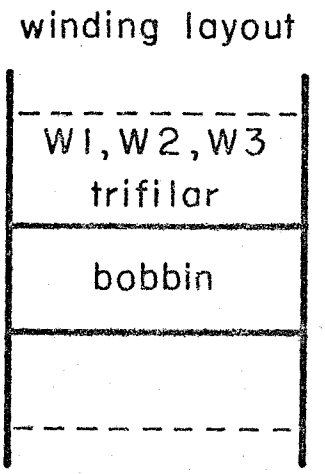

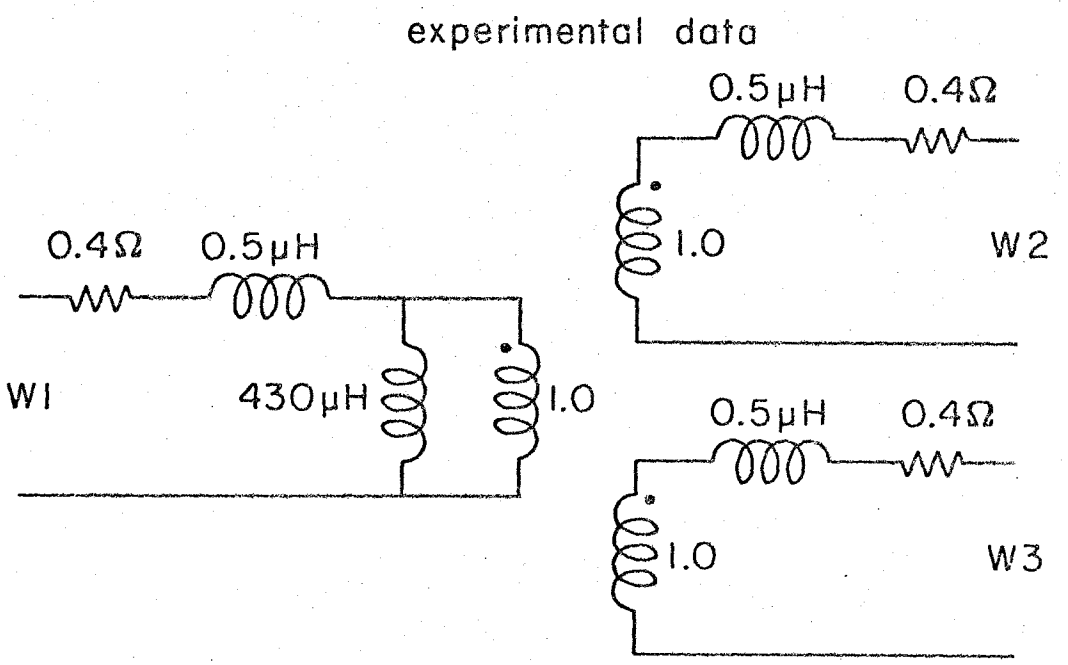

Fig. 10.1(a) The winding layout and the equivalent circuit model for the transformer #1.

b) Transformer 2

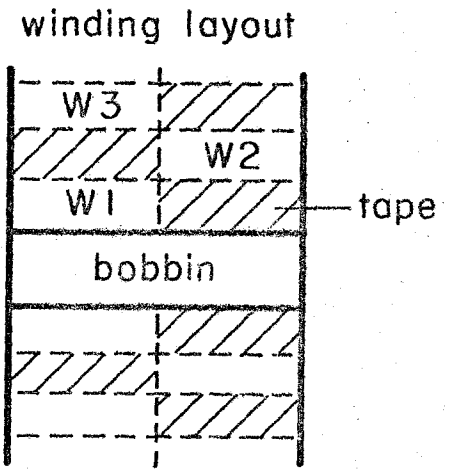

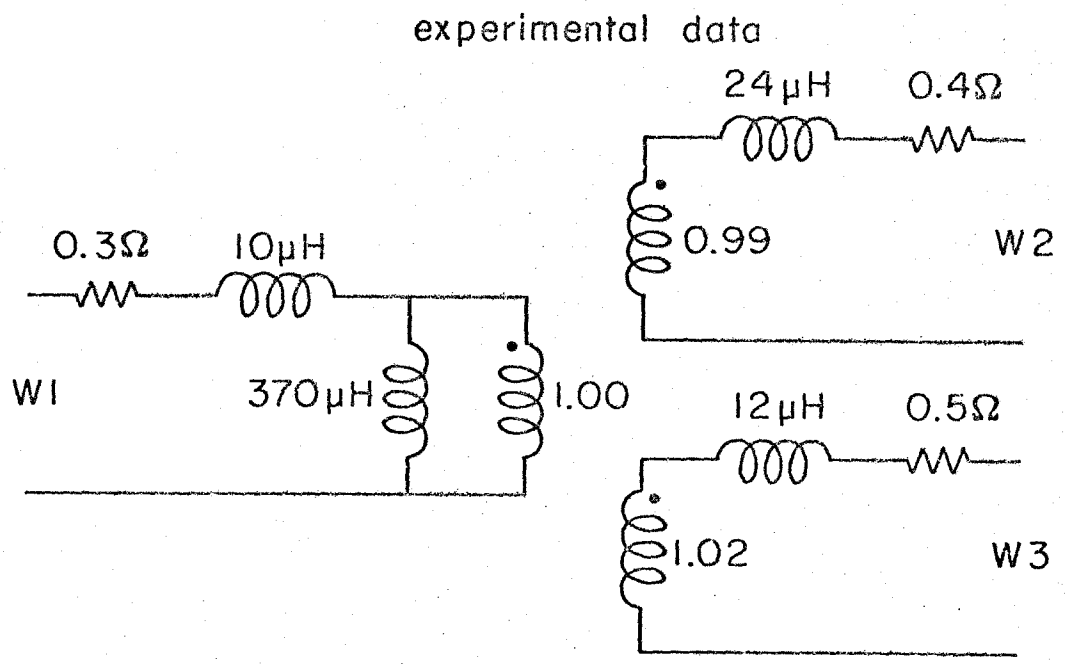

Fig. 10.1(b) The winding layout and the equivalent circuit model for the transformer #2.

c) Transformer 3

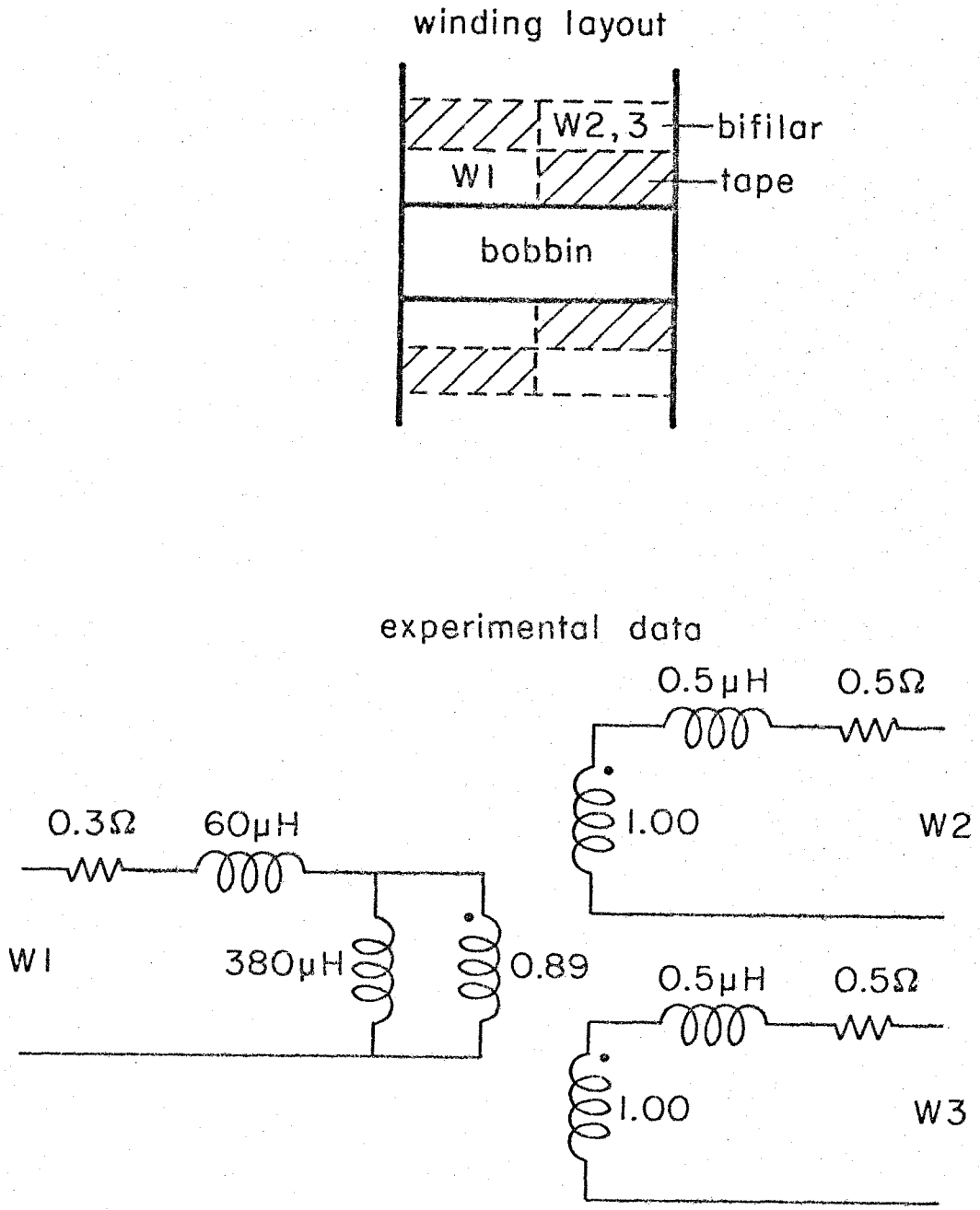

Fig. 10.1(c) The winding layout and the equivalent circuit model for the transformer #3.

The winding 1 was wound exactly the same way as in the transformer #2. Since winding 2 and winding 3 were bifilar, the leakage permeances p_{12}, p_{13}, p_2, p_3 must be very small, as in the case of the #1 transformer. This explains the small leakage inductances on winding 2 and winding 3. It also explains why the effective turns ratio between winding 2 and winding 3 is 1.0. Since the winding 1 was wound away from the other two windings, p_1 and p_{23} can be large. This explains why the winding 1 was wound closest to the core, and yet has the largest leakage inductance.

Note that the winding 1 in the transformer #3 was wound identically to that of the transformer #2 but the leakage inductances differ by 50μH. It is clear that this 50μH is the contribution from the permeance p_{23}. With the assumption that $n_1^2 p_{23}$ = 50μH and $n_1^2 p_{13}$ = 0μH, the effective turns ratio between winding 2 and winding 1 would be

$$\frac{n_1}{n_2}\,\frac{p_m + p_{13}}{p_m + p_{23}} = \frac{30}{30}\,\frac{380 + 0}{380 + 50} = 0.88 \qquad (10.1)$$

The measured value is 0.89.

Note that in all three transformers, winding 1 was always wound closest to the core, but the leakage inductance on winding 1 varies drastically from 0.5μH to 10μH, to 60μH depending on the winding layout of the other two windings.

10.2 Transformer model applied to the zero-ripple Ćuk converter

The purpose of this example is to test the validity of the

transformer model in a zero-ripple Ćuk converter. A coupled-inductor Ćuk converter with turns ratio n_2/n_1 is shown in Fig. 10.2. Its model, shown in Fig. 10.3 can be decomposed into a dc component as in Fig. 10.4 and an ac component as in Fig. 10.5. The input and output current ripples can be solved from Fig. 10.5 as

$$i_1(s) = [Z_2 + (1 - n_1/n_2)sM_o] \frac{v(s)}{Z_1Z_2 + sM_o[Z_1 + (n_1/n_2)^2Z_2]} \tag{10.2}$$

$$i_2(s) = [Z_1 - (1 - n_1/n_2)(n_1/n_2)sM_o] \frac{v(s)}{Z_1Z_2 + sMo[Z_1 + (n_1/n_2)^2Z_2]} \tag{10.3}$$

It is seen from eq. (10.2) that the input current ripple depends on the value of $Z_2 + (1-n_1/n_2)sM_o$. Since Z_2 is dominated by $sL_{\ell 2}$ at switching frequency and its higher harmonics, the switching ripple on the input current can be practically made zero if $L_{\ell 2} + (1-n_1/n_2)M_o$ is zero. This corresponds to the matching condition nk = 1 in [14]. Similar arguments hold for the output current. By adjusting n_1, n_2 and M_o, the ripple can be steered to the input or the output side.

A third winding can be wound on the same core to absorb the ripples away from both the input and output currents [18]. The arrangement is shown in Fig. 10.6. Its ac model is shown in Fig. 10.7 where m_1, m_2, m_3 are the effective turns ratios. From the model in Fig. 10.7, the current ripple on winding 1 is

$$i_1(s) = \frac{\dfrac{Z_1}{m_1^2} \,||\, \dfrac{Z_2}{m_2^2} \,||\, \dfrac{Z_3}{m_3^2} \,||\, \dfrac{sM_o}{m_3^2}}{Z_1} \frac{v(s)}{\dfrac{Z_2}{m_2(m_2-m_1)} \,||\, \dfrac{Z_3}{m_3(m_2-m_1)} \,||\, \dfrac{sM_o}{m_3^2}} \tag{10.4}$$

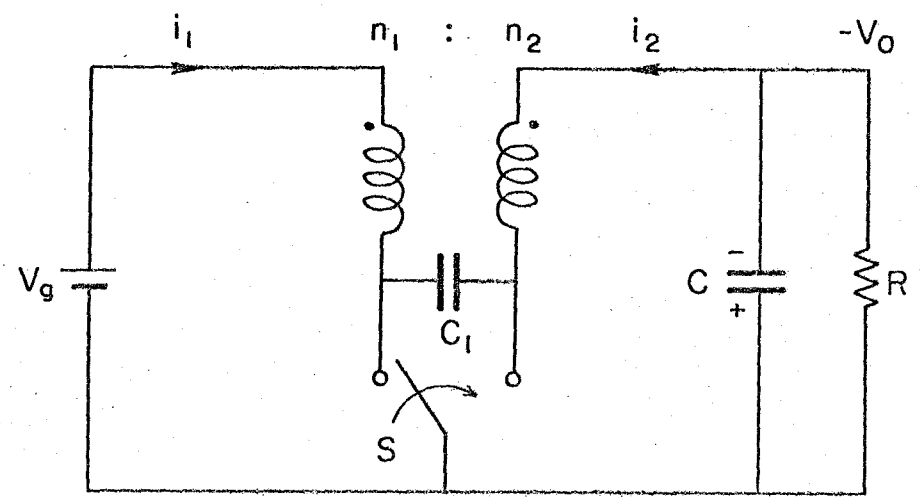

Fig. 10.2 The basic configuration of the coupled-inductor Ćuk converter.

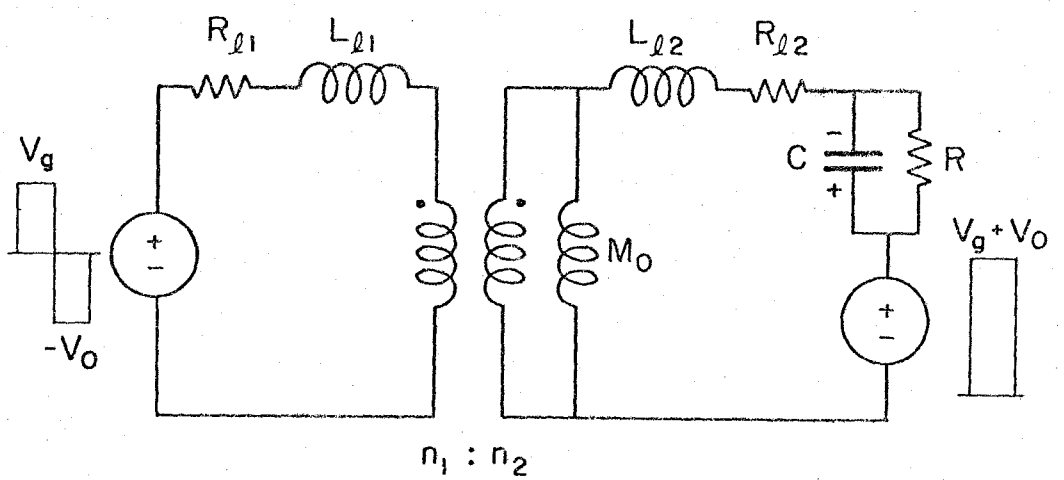

Fig. 10.3 A model for the coupled-inductor Ćuk converter in Fig. 10.2.

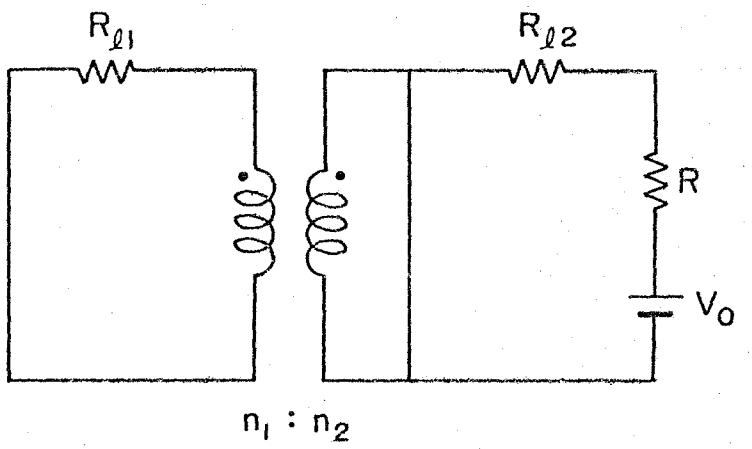

Fig. 10.4 The dc component of the model in Fig. 10.3.

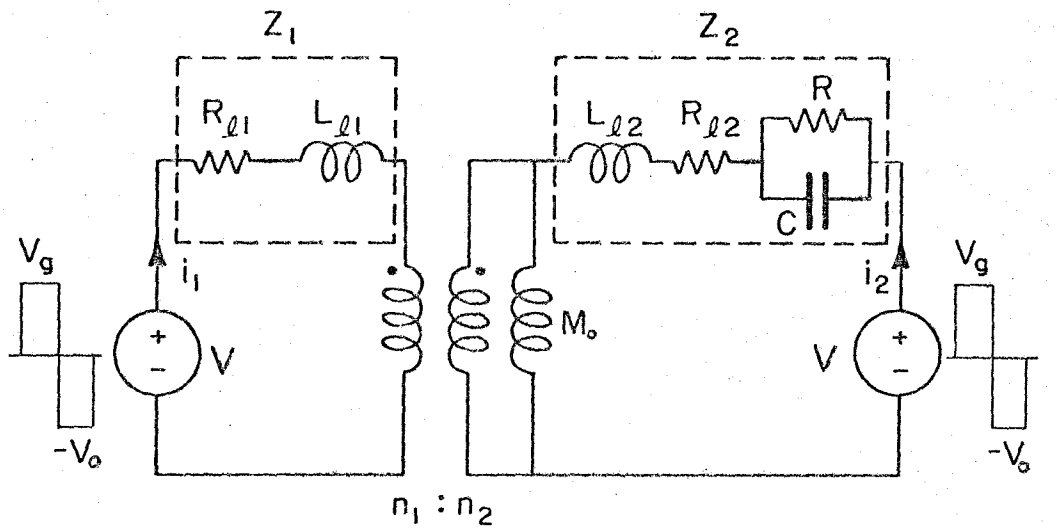

Fig. 10.5 The ac component of the model in Fig. 10.3.

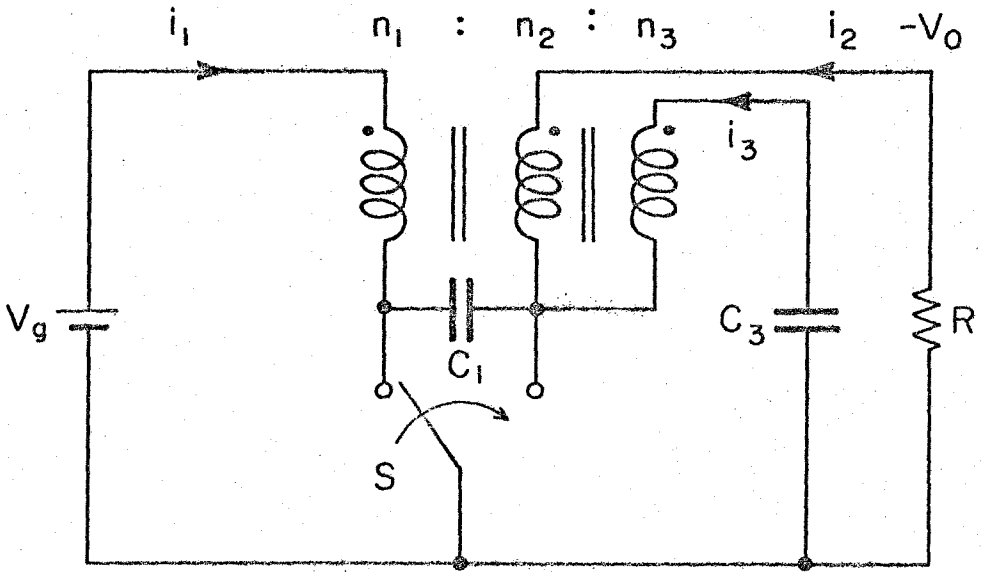

Fig. 10.6 A third winding can be added to the coupled inductor to absorb the switching ripples from the input and output inductor currents.

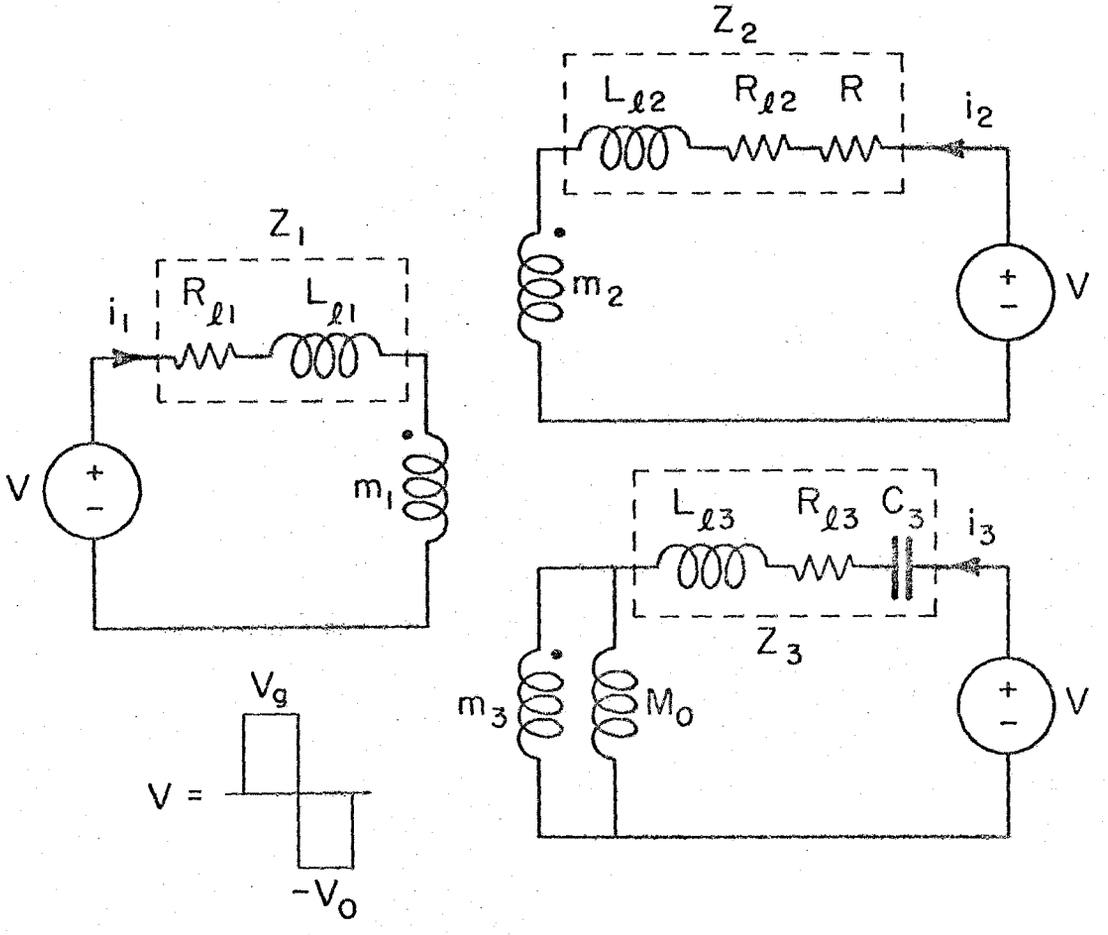

Fig. 10.7 The ac model for the circuit in Fig. 10.6.

Similar equations hold for $i_2(s)$ and $i_3(s)$.

If $m_1 = m_2 = m_3$, the current ripples become

$$i_1(s) = \frac{Z_1||Z_2||Z_3}{Z_1} \cdot \frac{v(s)}{sM_o + (Z_1||Z_2||Z_3)} \tag{10.5}$$

$$i_2(s) = \frac{Z_1||Z_2||Z_3}{Z_2} \cdot \frac{v(s)}{sM_o + (Z_1||Z_2||Z_3)} \tag{10.6}$$

$$i_3(s) = \frac{Z_1||Z_2||Z_3}{Z_3} \cdot \frac{v(s)}{sM_o + (Z_1||Z_2||Z_3)} \tag{10.7}$$

It is easily seen that the ripples in input and output currents can be made very small if $|Z_3|$ is much smaller than $|Z_1|$ and $|Z_2|$ at the switching frequency. This is the impedance division principle. Note that this principle holds only if $m_1 = m_2 = m_3$.

A demonstration circuit was built, whose circuit diagram is shown in Fig. 10.8. The coupled-inductor information is summarized in Fig. 10.9. Winding 1 was wound away from the bifilar winding 2 and 3 to create leakage permeances p_{23} and p_1 as discussed before. The extra 3 turns on winding 1 is to bring the effective turns ratio to 1:1:1. The waveforms are shown in Figs. 10.10 and 10.11. The fact that the winding 1 is directly connected to the power supply without any external impedance and yet the ripples on the input current are still cut down by the correct amount, demonstrates the validity of the transformer model.

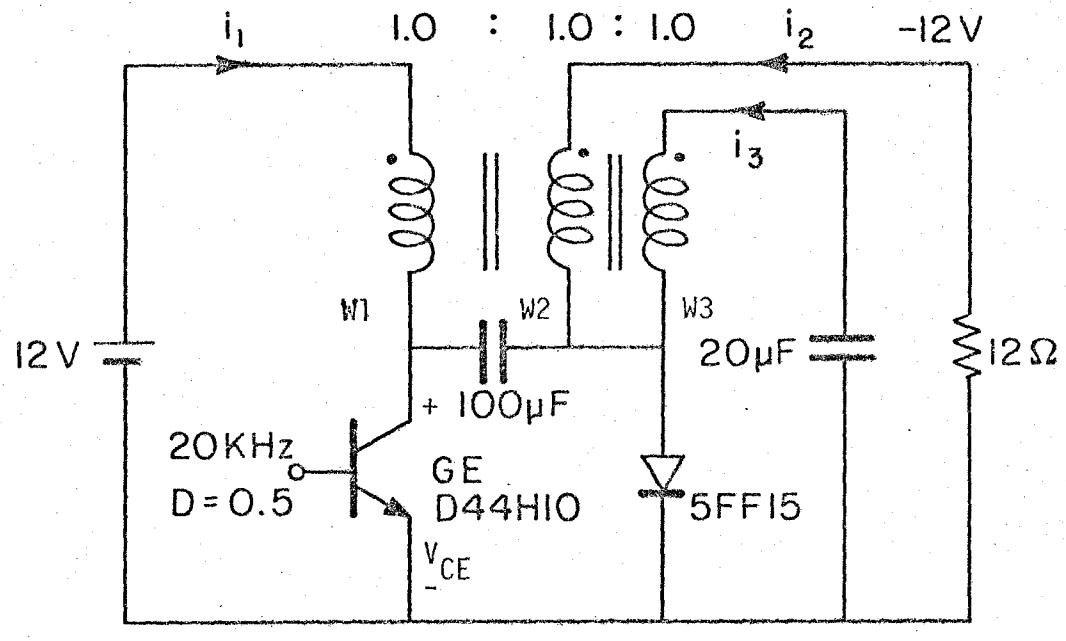

Fig. 10.8 The experimental circuit of a three-winding coupled-inductor Ćuk converter.

$N_1 = 32 \quad N_2 = N_3 = 29$ all of 28AWG wire

core: Ferroxcube 3019P-A400-3B7 ferrite pot core

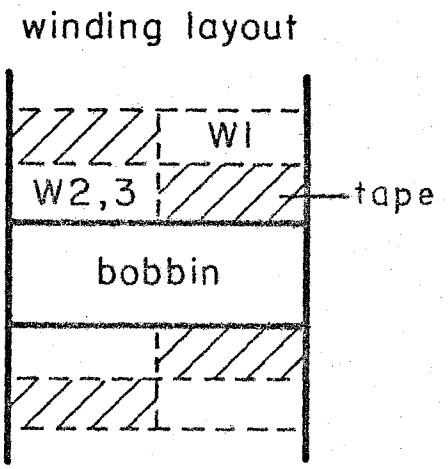

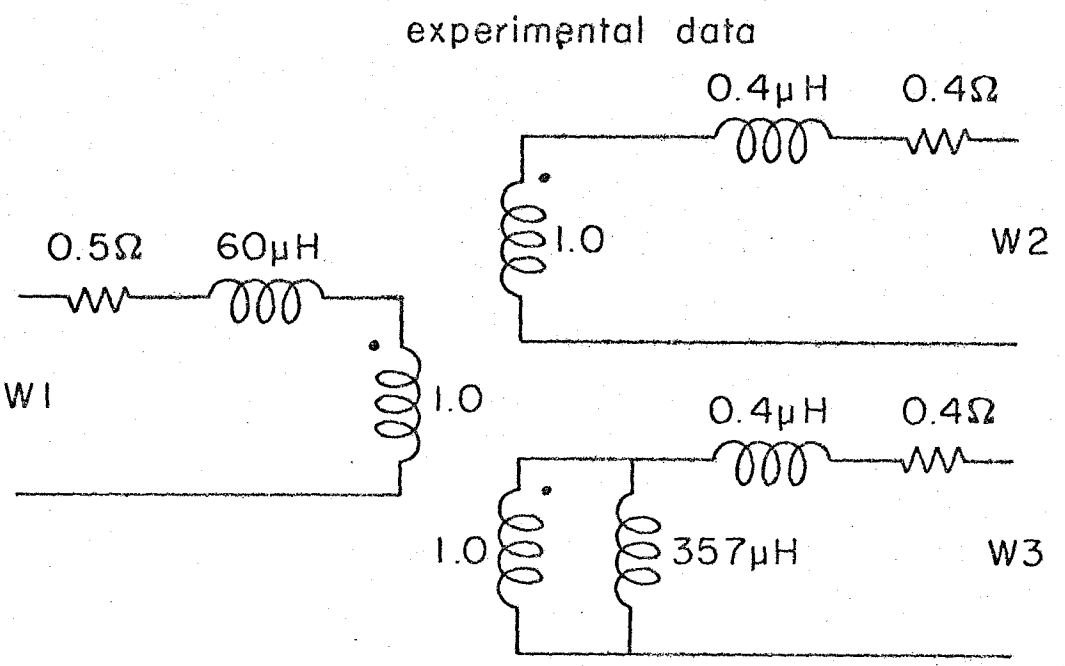

Fig. 10.9 The winding information and the equivalent circuit model of the coupled inductor used in the circuit of Fig. 10.8.

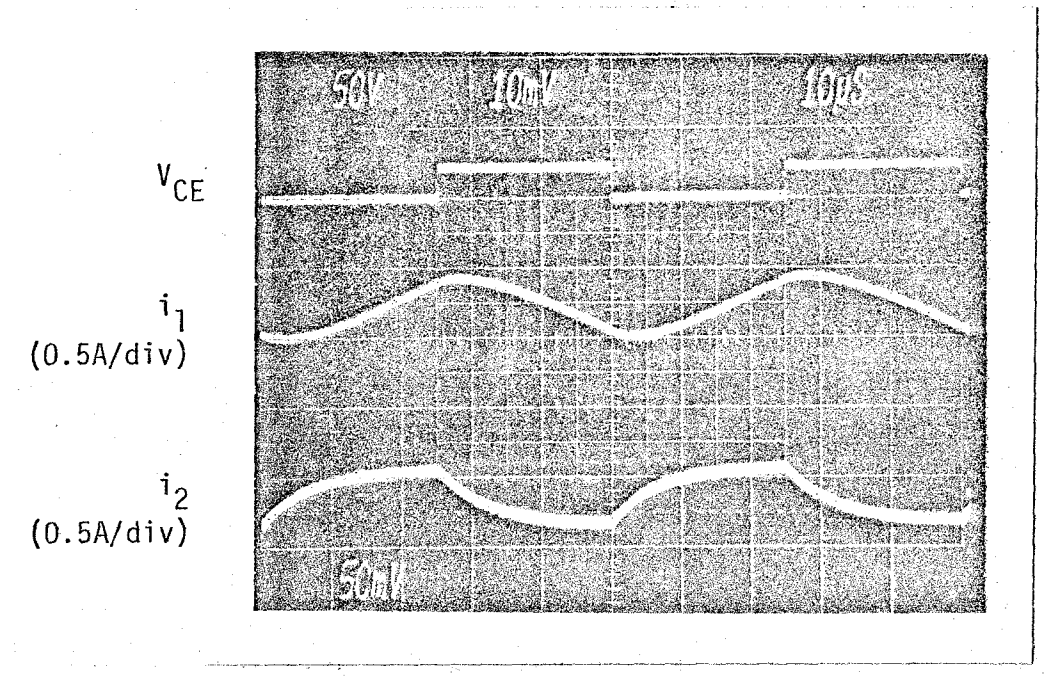

Fig. 10.10 *The input and output current ripples of the circuit in Fig. 10.8, with the third winding open.*

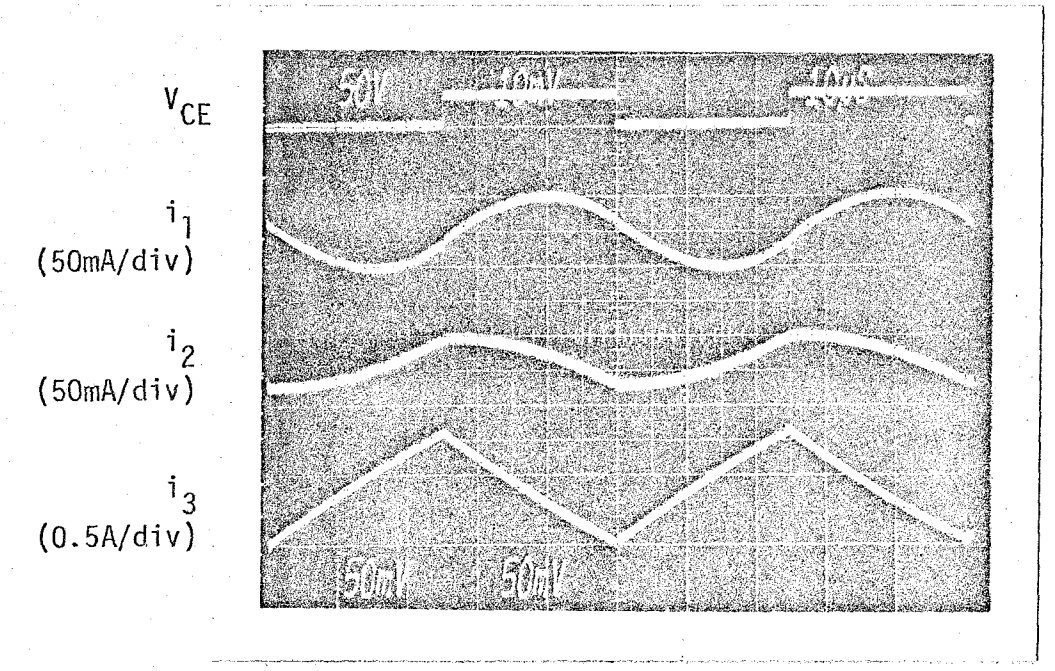

Fig. 10.11 *The current ripples in Fig. 10.10 are absorbed into the third winding which provides a low impedance path to the ground.*

10.3 Coupling coefficient as a function of air gap

In the zero-ripple Ćuk converter it is desired to know the functional dependence of the coupling coefficient k of a two-winding transformer on the length of the air gap ℓ_g [14]. In this section, it is found that the fringing flux in the air gap has substantial effect on the function 1/k vs. ℓ_g which would otherwise be a straight line.

Consider a two-winding transformer wound on a gapped core as shown in Fig. 10.12, in which ϕ_m and $\phi_{\ell 1}$, $\phi_{\ell 2}$ are the mutual and leakage fluxes per turn. H_m and B_m are the magnetic field intensity and magnetic induction inside the core while H_g and B_g are the corresponding quantities in the air gap. ℓ_m is the magnetic path length and ℓ_g is the gap length. Because of the fringing effect, the effective cross-section A_{cg} inside the air gap is different from the cross-section A_{cm} of the magnetic core.

Two of the Maxwell's equations can be written as:

$$\begin{cases} H_m \ell_m + 2H_g \ell_g = n_1 i_1 + n_2 i_2 & (10.8) \\ A_{cm} B_m = A_{cg} B_g \qquad (\nabla \cdot B = 0) & (10.9) \end{cases}$$

Inside the core: $$B_m = \mu_o \mu_r H_m \qquad (10.10)$$

Inside the air gap: $$B_g = \mu_o H_g \qquad (10.11)$$

where μ_o is the permeability of the free space and μ_r is the relative permeability.

By combinations of eqs. (10.8) through (10.11),

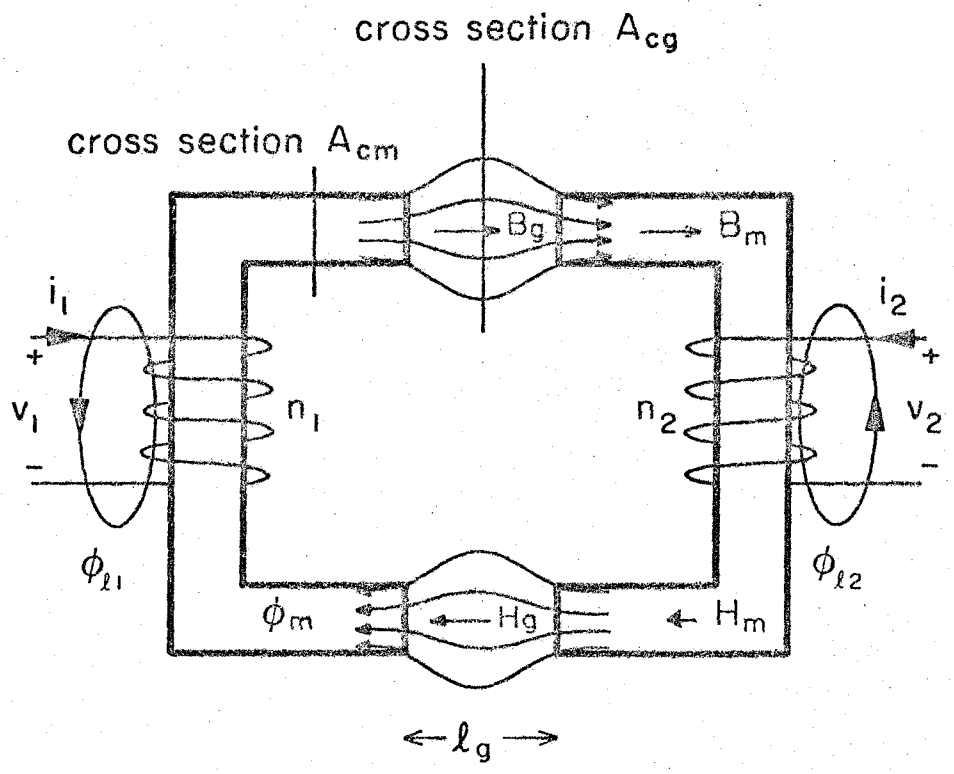

Fig. 10.12 A two-winding transformer with a small air gap.

$$B_m = \left[\frac{\mu_o \mu_r}{1 + \frac{A_{cm}}{A_{cg}} \frac{2\mu_r \ell_g}{\ell_m}} \right] \frac{n_1 i_1 + n_2 i_2}{\ell_m} \tag{10.12}$$

The quantity inside the bracket is the effective permeability of the gapped core, which is known as the "shear-over" effect on the B-H loop. From eq. (10.12),

$$\phi_m = B_m A_{cm} = p_m (n_1 i_1 + n_2 i_2) \text{ where } p_m = \frac{\mu_o A_{cg}}{2\ell_g + \frac{A_{cg}}{A_{cm}} \frac{\ell_m}{\mu_r}} \tag{10.13}$$

Note that when $\ell_g >> \frac{\ell_m}{\mu_r}$, the inductance per turn is proportional to the effective cross-section A_{cg} instead of the actual cross section A_{cm}. The relation between A_{cg}, A_{cm} and ℓ_g is a very complicated field mapping problem. An empirical equation has been found for rectangular cross-section core:

$$A_{cg} = (a + \ell_g)(b + \ell_g) \tag{10.14}$$

where a and b are the cross-sectional dimensions of the actual core faces [17]. Experience shows that this rule ordinarily gives satisfactory results if the correction applied does not exceed about one-fifth of the cross-sectional dimension to which it is applied. With eq. (10.14), p_m can be expressed as a function of the air gap:

$$p_m \simeq \frac{\mu_o (a + \ell_g)(b + \ell_g)}{2\ell_g + \ell_m/\mu_r} \tag{10.15}$$

In a two-winding transformer, the coupling coefficient k is defined as

$$k = \frac{M_{12}}{\sqrt{L_{11}L_{22}}} = \frac{n_1 n_2 p_m}{\sqrt{n_1^2(p_m + p_1) \cdot n_2^2(p_m + p_2)}} = \frac{1}{\sqrt{\left(1+\frac{p_1}{p_m}\right)\left(1+\frac{p_2}{p_m}\right)}}$$

$$= \frac{1}{1 + \frac{p_\ell}{p_m}} \quad \text{if the transformer is symmetrically wound such that}$$

$$p_1 \simeq p_2 = p_\ell \tag{10.16}$$

Substitution of eq. (10.15) into eq. (10.16) gives

$$k \simeq \frac{1}{1 + \frac{p_\ell \left(2\ell_g + \frac{\ell_m}{\mu_r}\right)}{\mu_o (a + \ell_g)(b + \ell_g)}} \tag{10.17}$$

$$\text{or} \qquad \frac{1}{k} \simeq 1 + \frac{p_\ell (2\ell_g + \ell_m/\mu_r)}{\mu_o (a + \ell_g)(b + \ell_g)} \tag{10.18}$$

Experiment shows that p_ℓ is approximately a constant as the gap length varies. Note that 1/k vs. ℓ_g would be a straight line if the fringing effect could be neglected.

An experimental set-up as shown in Fig. 10.13 was used to verify eqs. (10.14) and (10.18). Two core halves were mounted on a Kulicke-Soffa X-Y micropositioner. The gap length was adjusted by inserting Kraft paper of different thicknesses between the core halves so that the attractive force produced would not change the gap length. The core halves are Magnetics Inc. 2-103738-001A C-cores made of 2 mil

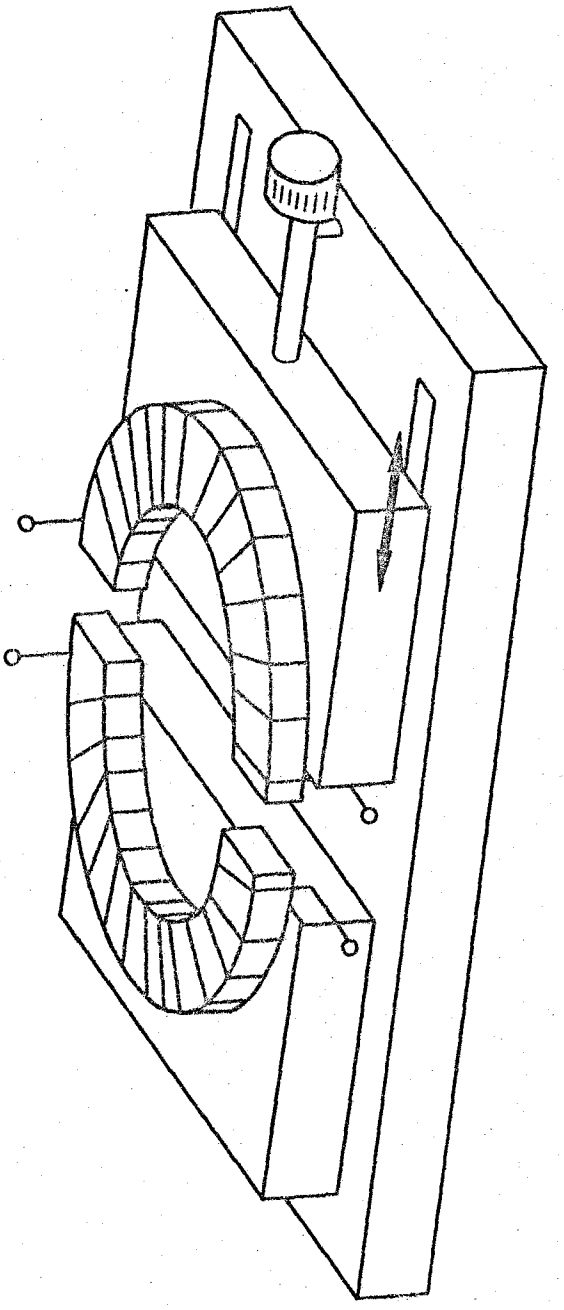

Fig. 10.13 Mechanical set-up providing continuous change of the gap length.

Westinghouse "Hypersil". The cross section of the core is 0.60 inch by 0.23 inch. The winding 1 is made of 50 turns of 24AWG wire and the winding 2 is made of 35 turns of the same wire. An HP3040A network analyzer system and a Tektronix AM503 current probe were used to measure L_{11}, L_{22}, M_{12} and L_{ℓ} (sum of the leakage inductances seen from winding 1) at 10kHz, as shown in Fig. 10.14. Note that only three out of these four quantities are independent. The data show very good consistency (to within 1%) between these four quantities except for the measurements when the air gap is less than 4 mils. For air gap less than 4 mils, the accuracy and consistency of the measurements were degraded because of the strong electromagnetic force between the core halves and the sensitivity of the measured quantity to the exact gap length.

From these measured quantities, the coupling coefficient k, the leakage inductances $L_{\ell 1}$, $L_{\ell 2}$, and the effective cross-section A_{cg} can be inferred. Both $L_{\ell 1}$ and $L_{\ell 2}$ are essentially constants (to within ± 2%) as the gap length varies from 4 mils to 78 mils. This shows that the leakage inductances are practically independent of the gap length. Thus the permeance p_{ℓ} in eq. (10.18) can be considered as a constant.

The effective cross section A_{cg} can be derived from the measured quantity M_{12} by the equation

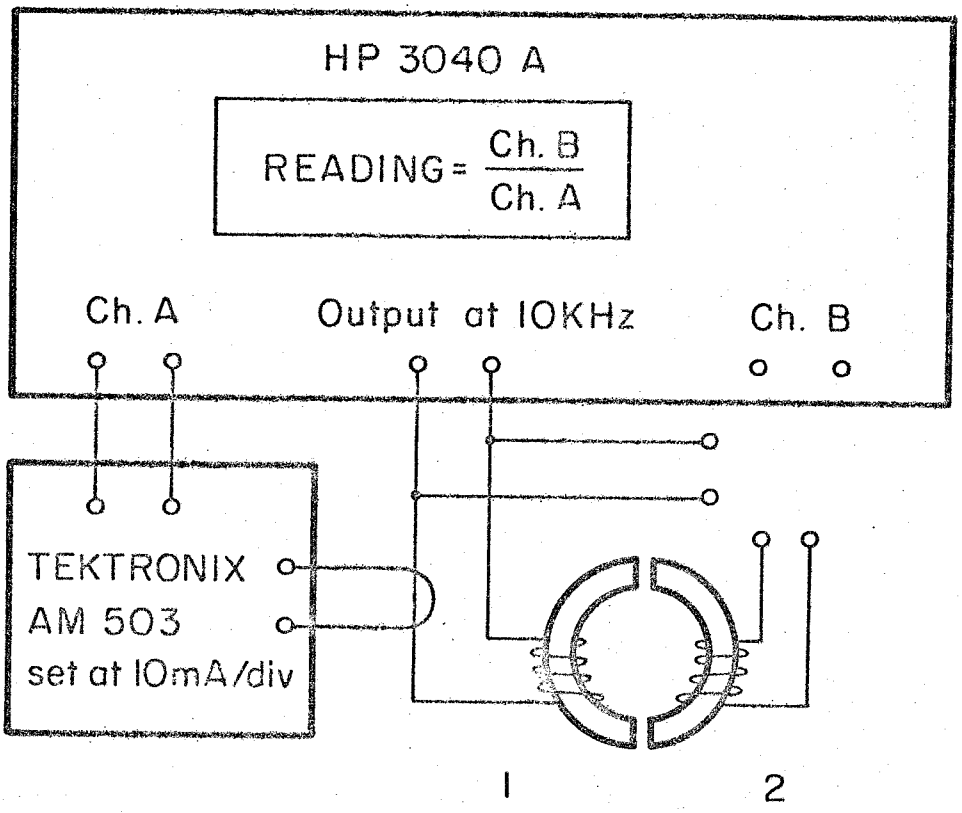

Reading = L_{11} *if Ch.B is connected to winding 1, with winding 2 open.*
= L_{ℓ} *if Ch.B is connected to winding 1, with winding 2 shorted.*
= M_{12} *if Ch.B is connected to winding 2.*

Fig. 10.14 The set-up for the measurement of L_{11}, L_{22}, L_{ℓ} *and* M_{12}.

$$A_{cg} = \frac{M_{12}\left(2\ell_g + \frac{\ell_m}{\mu_r}\right)}{n_1 n_2 \mu_o} \tag{10.19}$$

where $\frac{\ell_m}{\mu_r}$ = 6.7 mil which was determined by the data of M_{12} and A_{cm} at $\ell_g = 0$. The effective cross-section is plotted in Fig. 10.15 with the prediction of the empirical eq. (10.14). It is seen that the empirical equation is a good approximation. The dotted line in Fig. 10.15 is the physical cross-section of the core. The difference between the solid line and the dotted line is the effect of the fringing flux.

Figure 10.16 is a plot of the coupling coefficient derived from the measured quantities L_{11}, L_{22}, M_{12} and that predicted by eq. (10.18). It is seen that the prediction is reasonably good. The dotted straight line is the projected value of the coupling coefficient if the fringing effect were neglected.

From the data of this example, it is observed that the leakage inductances of a two-winding transformer are practically independent of the length of the air gap. The coupling coefficient decreases as the gap increases, but the leakage inductances remain the same. The decrease of the coupling coefficient is explained by the decrease of the mutual flux.

Without the fringing flux, the inverse of the coupling coefficient would be a linear function of the gap length. The "bending

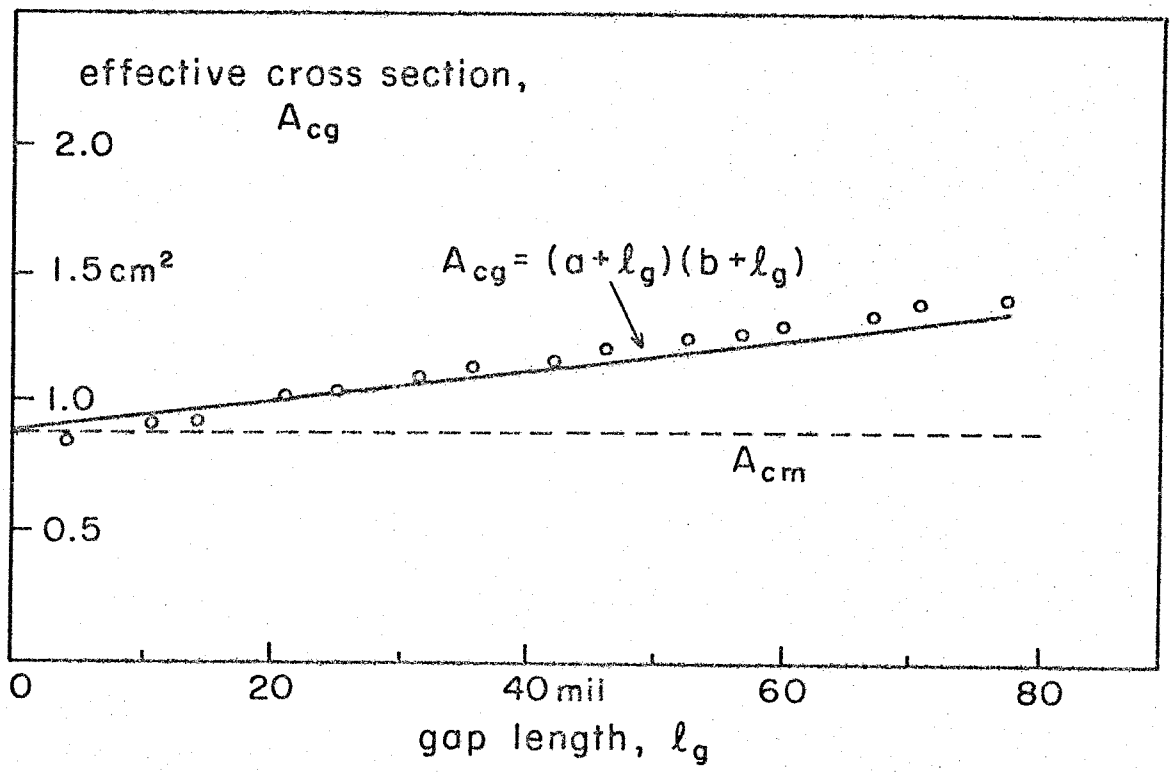

Fig. 10.15 Prediction and experimental data of the effective cross-section A_{cg} vs. the gap length ℓ_g. The dotted line is the physical cross-section of the core A_{cm}.

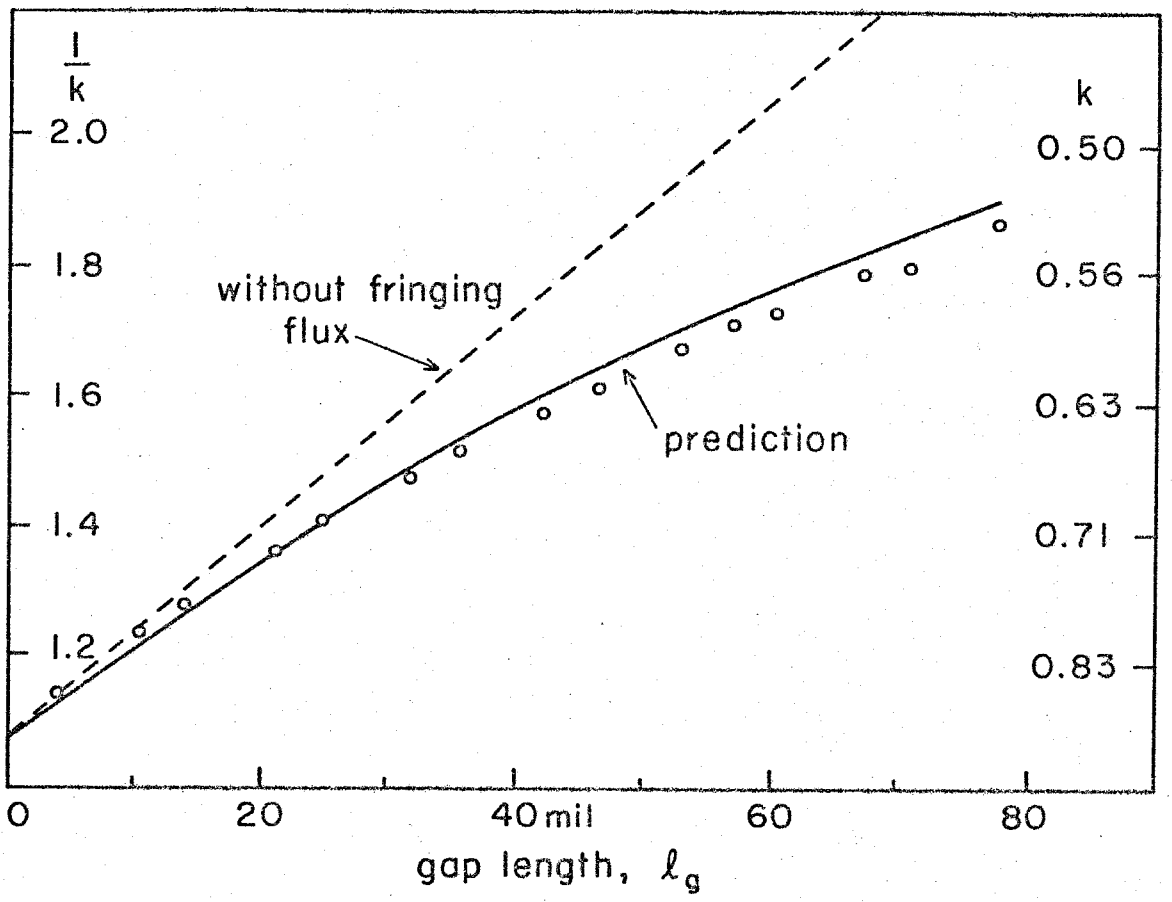

Fig. 10.16 Prediction and experimental data of the coupling coefficient k vs. the gap length ℓ_g. The dotted line is the predicted coupling coefficient if the fringing effect were neglected.

down" effect observed on the 1/k vs. ℓ_g curve is successfully explained by the fringing effect.

CHAPTER 11

CONCLUSIONS

The concept of permeance, which is directly related to the magnetic flux, was used to express the parameters in transformer models. This has the advantage of retaining more physical insight of a physical transformer in its equivalent circuit model. For example, in a three-winding transformer, the effect of the physical layout of winding 2 and 3 on the leakage inductance of winding 1 can be seen from the model directly. The effect of the leakage flux on the effective turns ratio is also explicitly described in the model.

The π-model is recommended whenever applicable because it is simple to use and easy to interpret. It is interesting to see that this model is under-determined, uniquely-determined, and over-determined for the cases of two-winding, three-winding and four-winding transformers, respectively. In the two-winding case, the effective turns ratio can be chosen arbitrarily. But every parameter is uniquely determined in the three-winding case. For a four-winding transformer, the simple π-model is adequate only for tetra-filar, tri-filar and separate-winding situations. The general model has to be used when the π-model is not applicable.

The three-winding π-model was verified as applied to the zero-ripple Ćuk converter in Sec. 10.2. The concept of permeance also helps the understanding of the relationship between coupling

coefficient and the gap length. The fringing flux was found to have substantial effect. It was also observed in this study that the leakage inductances are practically independent of the gap length.

PART III

CROSS-REGULATION OF THE TWO-OUTPUT ĆUK CONVERTER

CHAPTER 12

INTRODUCTION

A multiple-output switching regulator is usually constructed by insertion of an isolation transformer with multiple secondary windings in the switching part of the circuit to split the energy flow to the outputs. Similar output circuits are connected to each of the secondary windings. The "principal" output voltage is directly sensed by the feedback network and regulated to the desired value. The others, or the "slaved" outputs, are not directly regulated, but are fixed with respect to the principal output voltage by the turns ratio of the isolation transformer. This provides a cost-effective method of providing multiple outputs in a switching regulator. However, the slaved outputs usually do not have as good load regulations as does the principal output. The variations of the slaved output voltages due to the changes of the load currents are called cross-regulation.

The Ćuk converter, as shown in Fig. 12.1, introduced at the 1977 PESC [7], was described as having a configuration which provides the basic dc-to-dc conversion property with the smallest number of elements that permit both the input and output currents to be nonpulsating. This basic topology has been extended in a simple and elegant manner to incorporate dc isolation and multiple outputs, with retention of a single switch [19], as shown in Fig. 12.2. Typically, this converter is incorporated in a feedback loop in which only the principal output voltage V_1 is regulated. In this

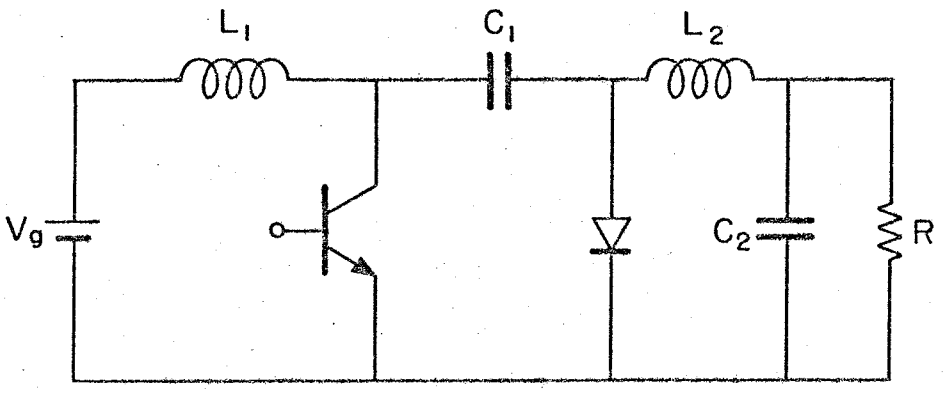

Fig. 12.1 The basic topology of the dc-to-dc Ćuk converter.

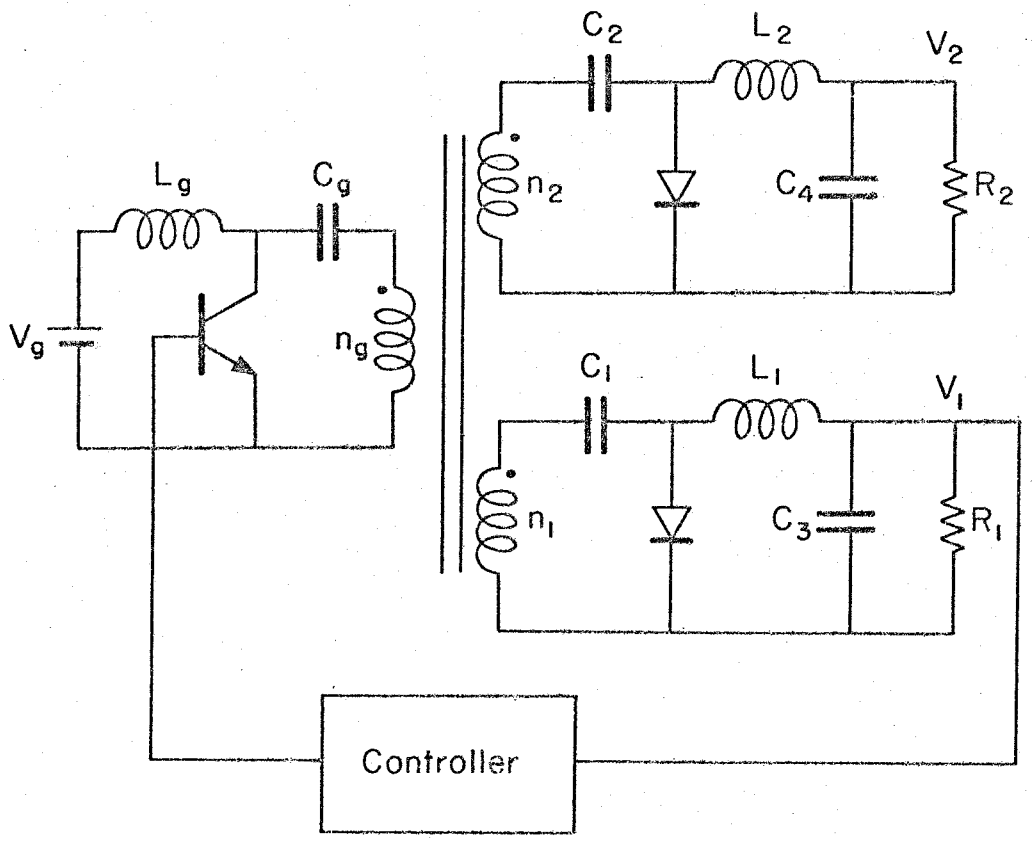

Fig. 12.2 A dc-isolated multiple-output Ćuk converter with principal output voltage V_1 directly regulated.

application, the regulated voltage V_1 remains essentially constant, but the slaved output V_2 can vary substantially with the currents drawn from either output.

The objective of this study is to find out all the causes and their quantitative effects on the cross-regulation of a two-output Ćuk converter operated in the continuous conduction mode.

Imperfect cross-regulation in conventional multiple-output converters results from, among other effects, inductor and transformer winding resistances, unequal diode drops, and leakage inductances of the isolation transformer. In the multiple-output Ćuk converter, the separate coupling capacitances C_1 and C_2 in the circuit of Fig. 12.2 contribute an additional term to the cross-regulation property because of their unequal discharge during the switch ON-interval. This effect is discussed in Chapter 13 with all the elements in the circuit assumed to be ideal. It will be seen that sufficiently large values of the capacitances C_1 and C_2 can be used to make the contribution to the cross-regulation from this effect arbitrarily small compared with the remaining effects. The same analysis is repeated in Chapter 14 with all the non-idealities in the circuit included in the model.

CHAPTER 13

THE EFFECT OF UNEQUAL DISCHARGE OF THE COUPLING CAPACITANCES

In this chapter, emphasis will be concentrated on the effect of unequal discharge of the coupling capacitances on the cross-regulation of a Ćuk converter. All the circuit elements will be assumed ideal and the inductor current ripples will be assumed small compared with their dc levels.

With this assumption, a two-output Ćuk converter can be represented by the model in Fig. 13.1. The steady state input and output currents are modelled by the constant current source. The output currents flow from the ground into the converter because the output voltages are negative. The transistor and the diodes are modelled by ideal switches. Since the isolation transformer is assumed ideal, it can be removed from the model if the state variables and element values are properly adjusted for the turns ratios, as demonstrated in Fig. 13.2 (a)(b). Both Fig. 13.2 (a), (b) are equivalent to Fig. 13.1. For simplicity, the turns ratio of the isolation transformer will be assumed to be 1:1:1 in this chapter, and the model in Fig. 13.3 will be used. The results derived from this chapter can be generalized to arbitrary turns ratio by simple replacements of $V_1 \rightarrow V_1/n_1$, $C_1 \rightarrow n_1^2 C_1$, $I_1 \rightarrow n_1 I_1$, etc.

In Fig. 13.3, let $\langle v_1 \rangle$ be the well-regulated output voltage; then, $\langle v_1 \rangle - \langle v_2 \rangle$ represents the deviation from the desired value at

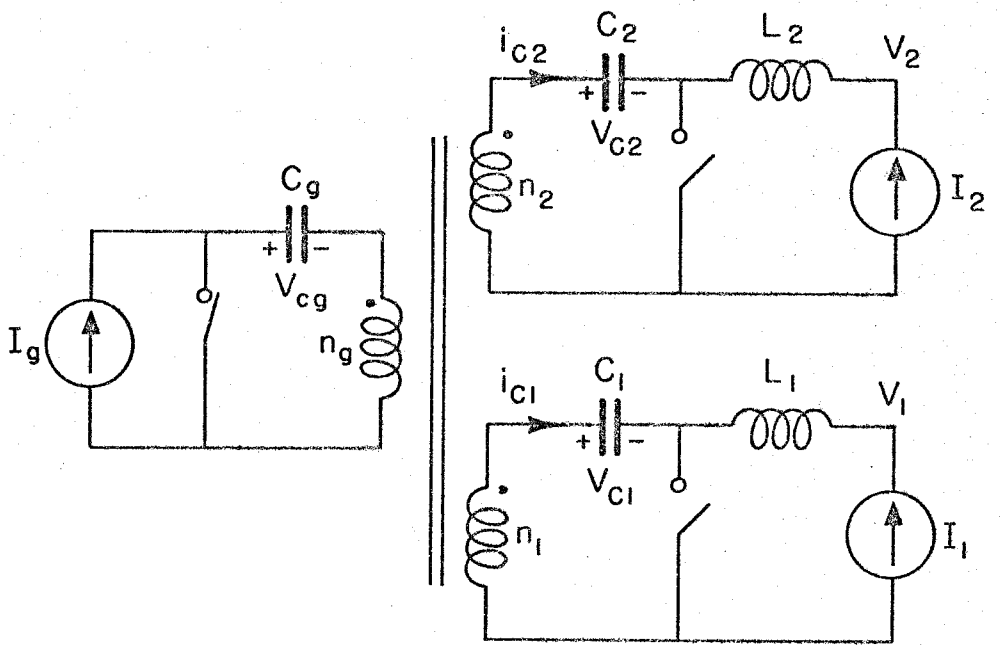

Fig. 13.1 A circuit model for the two-output Ćuk converter in Fig. 12.2, assuming ideal components and negligible ripples on the inductor currents.

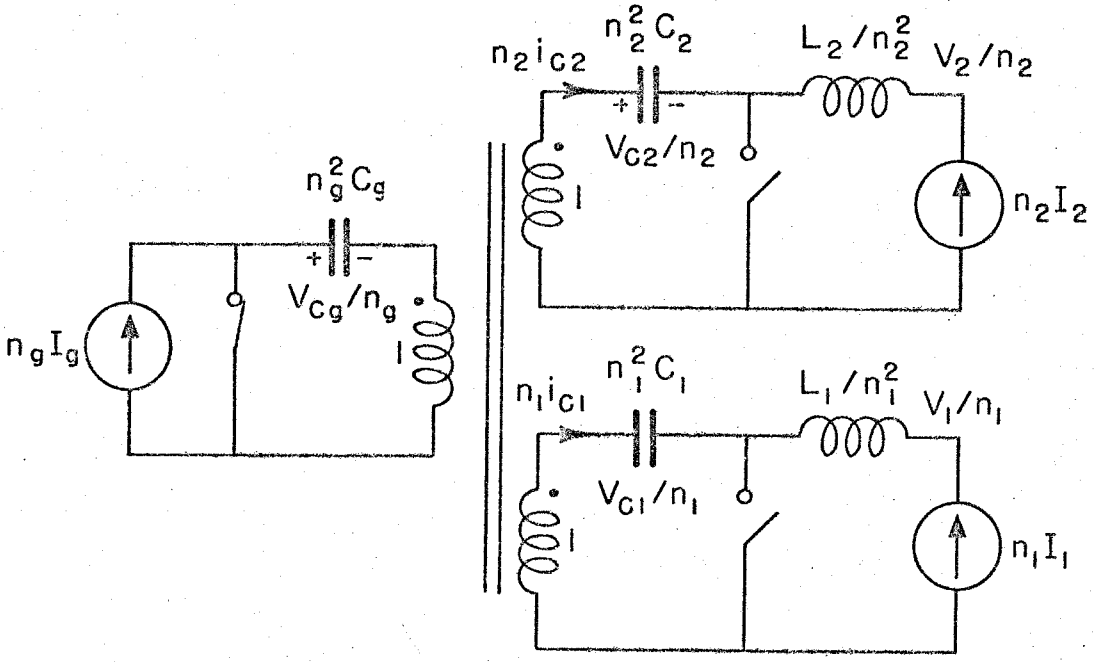

Fig. 13.2(a) The turns ratio of the ideal transformer in Fig. 13.1 can be reduced to 1:1:1 by properly adjusting the values of the components and the corresponding state variables.

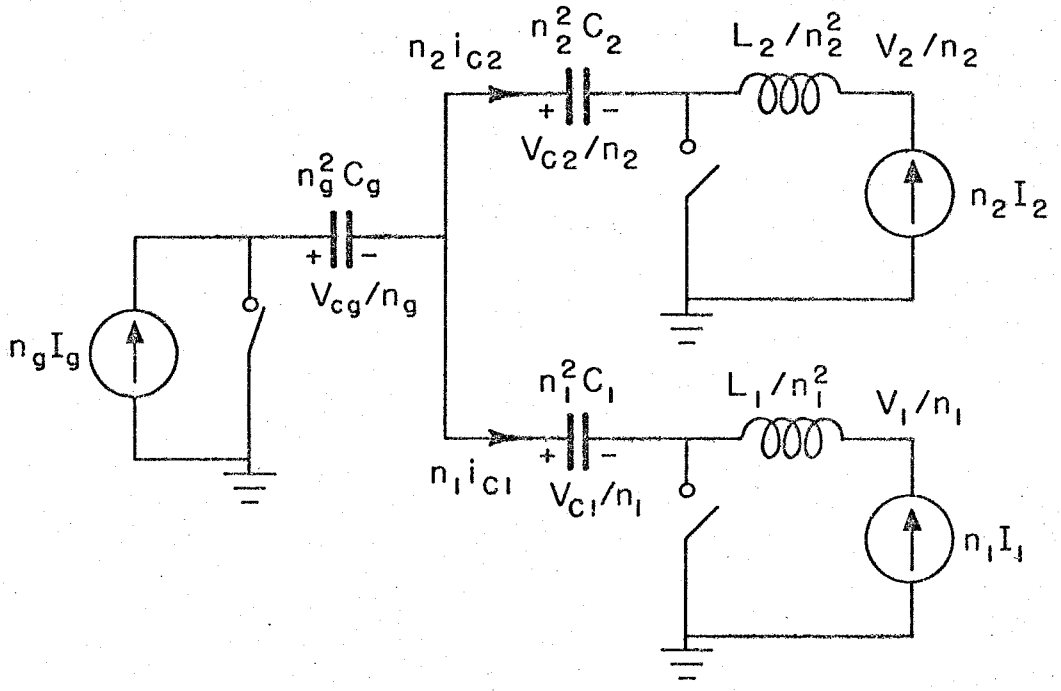

Fig. 13.2(b) *The 1:1:1 ideal transformer in Fig. 13.2(a) can be removed. This circuit model is equivalent to that in Fig. 13.1.*

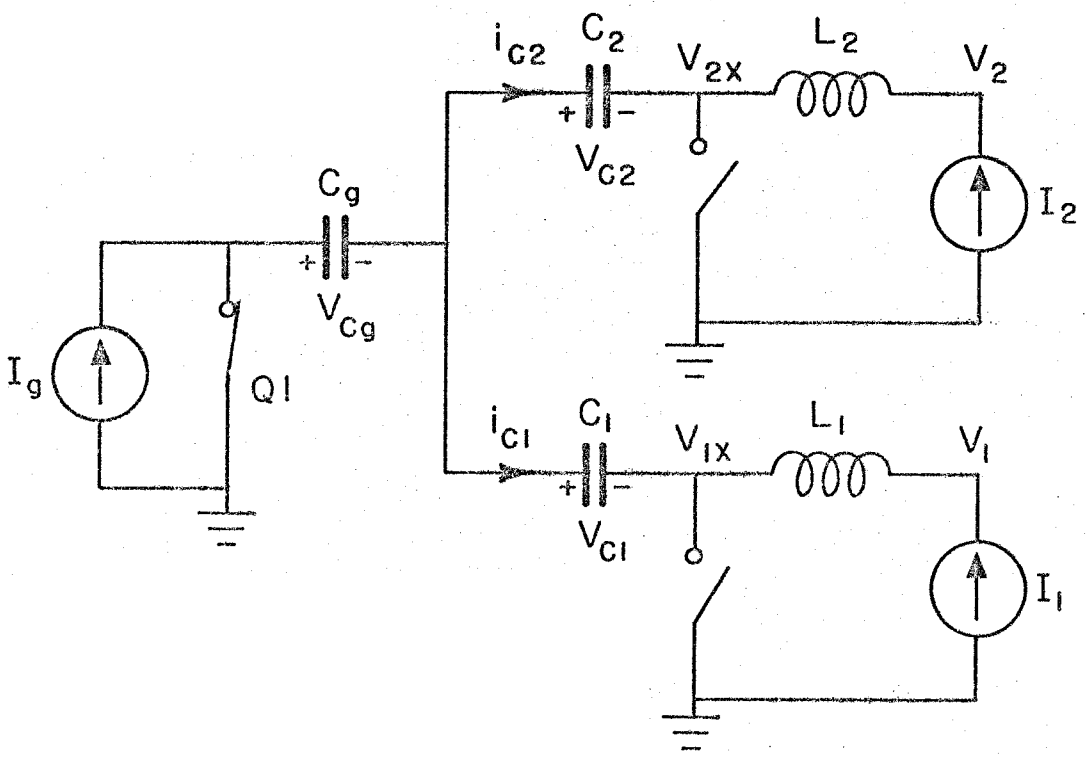

Fig. 13.3 *A simplified model of Fig. 13.1. The transformer turns ratio is assumed to be 1:1:1.*

the slaved output*. Since the average voltage across an inductor is always zero in steady state,

$$\langle v_1 \rangle = \langle v_{1x} \rangle \tag{13.1}$$

and

$$\langle v_2 \rangle = \langle V_{2x} \rangle \tag{13.2}$$

therefore,

$$\begin{aligned} \langle v_1 \rangle - \langle v_2 \rangle &= \langle v_{1x} \rangle - \langle v_{2x} \rangle \\ &= \langle v_{C2} \rangle - \langle v_{C1} \rangle \\ &= \langle v_{C2} - v_{C1} \rangle \\ &= \left\langle \frac{\int_0^t i_{C2} dt'}{C_2} - \frac{\int_0^t i_{C1} dt'}{C_1} \right\rangle \end{aligned} \tag{13.3}$$

Equation (13.3) suggests the procedure to calculate the cross regulation:

(1) Find the capacitor current waveforms, $i_{C1}(t)$ and $i_{C2}(t)$

(2) Construct $v_{C2} - v_{C1}$ from $i_{C1}(t)$ and $i_{C2}(t)$

(3) The cross regulation is equal to the average value of $v_{C2} - v_{C1}$.

Typical $i_{C1}(t)$ and $i_{C2}(t)$ are plotted in Fig. 13.4 with corresponding $v_{C2} - v_{C1}$ plotted in Fig. 13.5. They are explained in the following.

At t=0, when the transistor Q_1 just turns on and the two

* $\langle x(t) \rangle$ represents the dc component of the time dependent quantity $x(t)$.

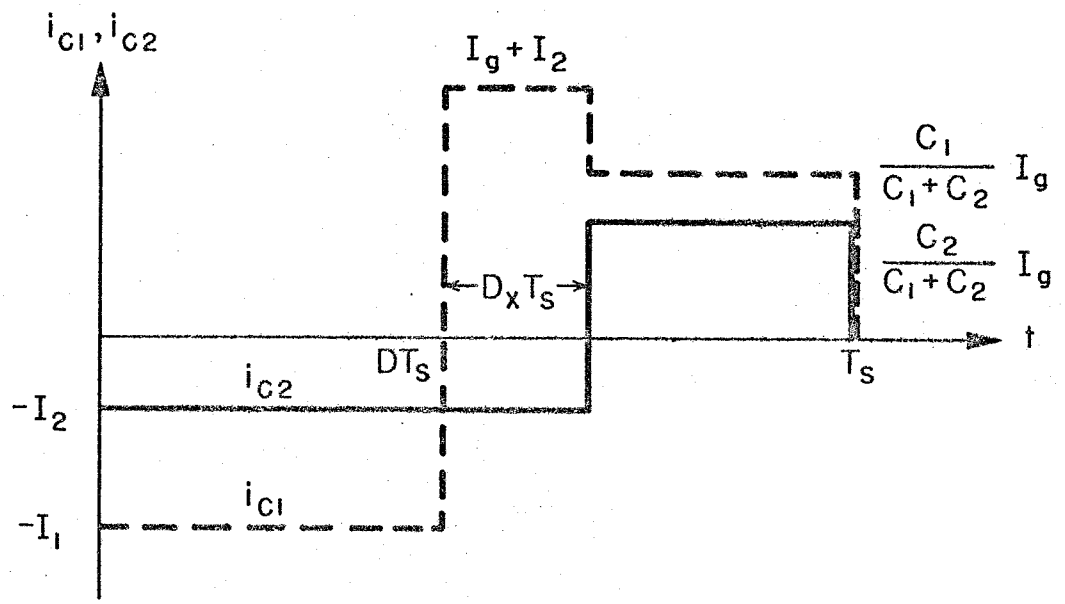

Fig. 13.4 Idealized capacitor current waveforms i_{C1} and i_{C2} in a two-output Ćuk converter.

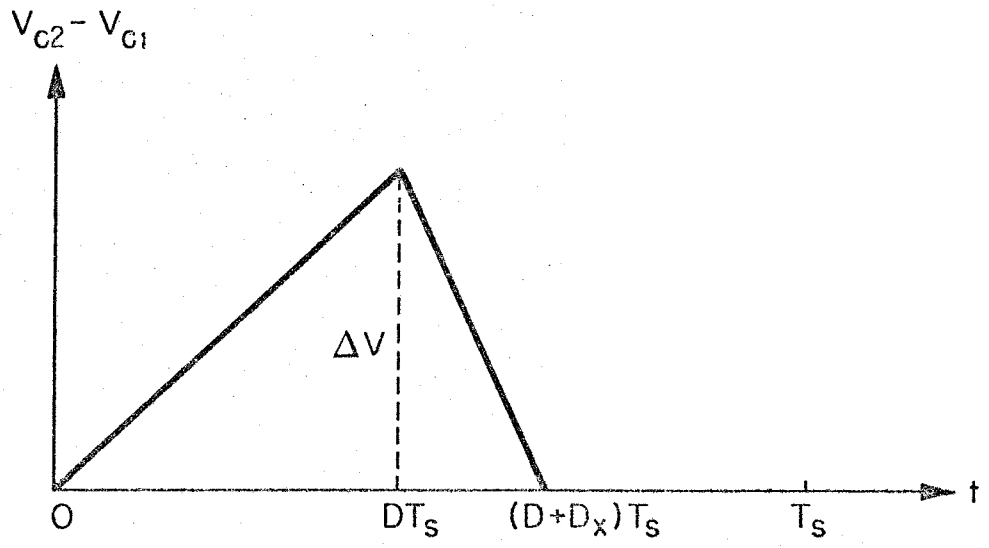

Fig. 13.5 The voltage difference between the two capacitors C_1 and C_2

diodes just turn off, $v_{C1} = v_{C2}$ and the two capacitors start to discharge with load currents $-I_1$ and $-I_2$ repectively. By the end of DT_s, a voltage difference

$$v_{C2} - v_{C1} = \Delta V = \left(\frac{I_1}{C_1} - \frac{I_2}{C_2}\right)DT_s \tag{13.4}$$

has been developed across the two capacitors. If ΔV is positive, diode 1 will turn on as soon as the transistor turns off at $t=DT_s$, but diode 2 will remain off because it is reverse biased by $-\Delta V$. While C_2 continues to be discharged with $-I_2$, C_1 is now charging with I_g+I_2. This helps to reduce the voltage difference $v_{C2} - v_{C1}$ by a rate of $\frac{I_g+I_2}{C_1} + \frac{I_2}{C_2}$ and bring up the voltage across the diode 2 until, D_xT_s later, $v_{C1} = v_{C2}$ and diode 2 turns on. The source current I_g now splits into two paths proportional to the capacitance values so that the voltages across the two capacitors remain equal to the end of the cycle.

The cross regulation can be calculated from the average value of Fig. 13.5:

$$\langle v_1 \rangle - \langle v_2 \rangle = \frac{\Delta V}{2}(D+D_x) \tag{13.5}$$

where

$$\Delta V = \left(\frac{I_1}{C_1} - \frac{I_2}{C_2}\right)DT_s$$

and

$$D_x = \frac{\Delta V}{\left(\frac{I_g + I_2}{C_1} + \frac{I_2}{C_2}\right)T_s}$$

It is seen that the two diodes in a two-output Cuk converter do not turn on simultaneously if the two capacitors are not discharged equally. Its effect on cross-regulation is represented by the area under the triangle of Fig. 13.5. This contributes an extra term to the cross-regulation which does not appear in most other dc-to-dc converters. However, this term can be made very small if the capacitance values are large, as can be seen from eq. (13.5). In fact, it will be seen from the next chapter that if the capacitances C_1, C_2 are large enough, the cross-regulation of a Ćuk converter will be dominated by the non-idealities in the circuit, just as in most other dc-to-dc converters. It should be noticed that the requirement for large capacitances C_1 and C_2 does not limit the dynamics of the converter because the energy transfer capacitor C_g, which is in series with C_1 and C_2, can be made small.

If the inductor current ripples are not small compared with their dc values, Fig. 13.4 and Fig. 13.5 will be modified into Fig. 13.6 and Fig. 13.7 where ΔI_1 is the peak-to-peak current ripple of i_{L1} and I_1 is its dc value. Similar definitions hold for ΔI_2 and ΔI_g. The dotted lines are the approximations made by neglecting the current ripples and using their dc values only. The shaded area of Fig. 13.7 represents the correction terms to eq. (13.5). It can be shown that the shaded area is less than

$$\frac{D^2T_s}{12}\left(\frac{\Delta I_1}{C_1}-\frac{\Delta I_2}{C_2}\right)+\frac{D^2T_s\left(\frac{I_1}{C_1}-\frac{I_2}{C_2}\right)^2}{4\left(\frac{I_2+I_g}{C_1}+\frac{I_2}{C_2}\right)^2}\cdot\left(\frac{\Delta I_g+\Delta I_2}{C_1}+\frac{\Delta I_2}{C_2}\right) \qquad (13.6)$$

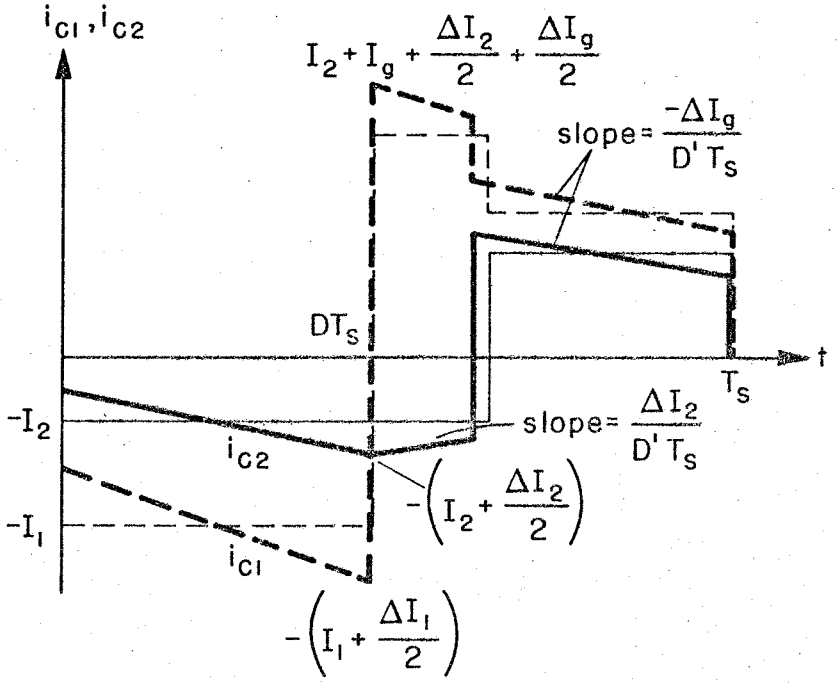

Fig. 13.6 The capacitor current waveforms with their switching ripples included.

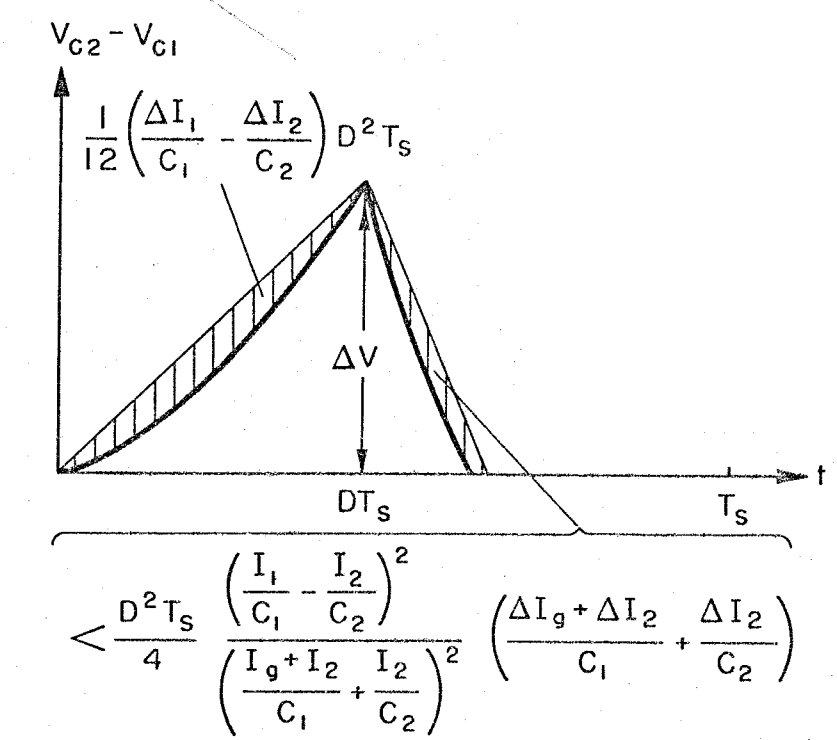

Fig. 13.7 The switching ripples of the capacitor currents have very small effect on the voltage difference between the two capacitors.

which, in most practical cases, is small compared to the value given by eq. (13.5). The inductor current ripples will therefore be neglected in the following chapters and their dc values are used as approximations.

CHAPTER 14

THE EFFECT OF COMPONENT NON-IDEALITIES ON CROSS-REGULATION

Parasitics play important roles in cross-regulation. The output voltages are affected by the parasitics such as the ESR of the capacitors, the winding resistances of the transformer and the inductors, the leakage inductances of the transformer, and diode offset voltage. Among all these parasitics, the leakage inductances of the transformer are the most undesirable. In fact, the converter cannot operate properly when the leakage inductances are too large. In Sec. 14.1, the limitation on the size of the leakage inductances is discussed. The effects of the smaller leakage inductances as well as the other parasitics on the cross-regulation are then investigated in the following sections.

14.1 Limitation on the sizes of the leakage inductances

A three-winding transformer can be modelled by a series leakage inductance and a series winding resistance connected to each winding as discussed in Part II. The effect of leakage inductances on the Ćuk converter during turn-on and turn-off are explained in the following.

As the transistor is being turned off, a large voltage spike is produced across the transistor because the currents are reversing their directions through the leakage inductances, as shown in Fig. 14.1. The magnitude of the voltage across the transistor is

$$v_{CE} = v_{Cg} + v_{Cl} + (v_{\ell g}+v_{\ell l})$$

$$= v_{Cg} + v_{Cl} + \left(\ell_g \frac{\Delta I_{Cg}}{t_{off}} + \ell_l \frac{\Delta I_{Cl}}{t_{off}}\right) \qquad (14.1)$$

where t_{off} is the turn-off time of the transistor

$\Delta I_{Cg}, \Delta I_{Cl}$ are the magnitudes of the currents which reverse direction during turn-off and

ℓ_g, ℓ_l are the leakage inductances of the isolation transformer

For safe operation, the quantity in eq. (14.1) has to be smaller than the max. V_{CEO} allowed, otherwise, a snubber has to be used.

When the transistor is being turned on, a voltage spike appears across the diode in such a direction as to reduce the reverse diode voltage, as can be seen from Fig. 14.2. The diode voltage during the transient is

$$v_{Dl} = -(v_{Cl}+v_{Cg}) + (v_{\ell g}+v_{\ell l})$$

$$= -(v_{Cl}+v_{Cg}) + \left(\ell_g \frac{\Delta I_{Cg}}{t_{on}} + \ell_l \frac{\Delta I_{Cl}}{t_{on}}\right) \qquad (14.2)$$

where t_{on} is the turn-on time of the transistor and

$\Delta I_{Cg}, \Delta I_{Cl}$ are the magnitudes of the currents which reverse direction during the transient.

For normal operation, the quantity in eq. (14.2) is negative so that the diode is off when the transistor is on. However, if the leakage inductances are too large, v_{Dl} in eq. (14.2) can be postive. When this is the case, the diode will remain on with v_{Dl} clamped at

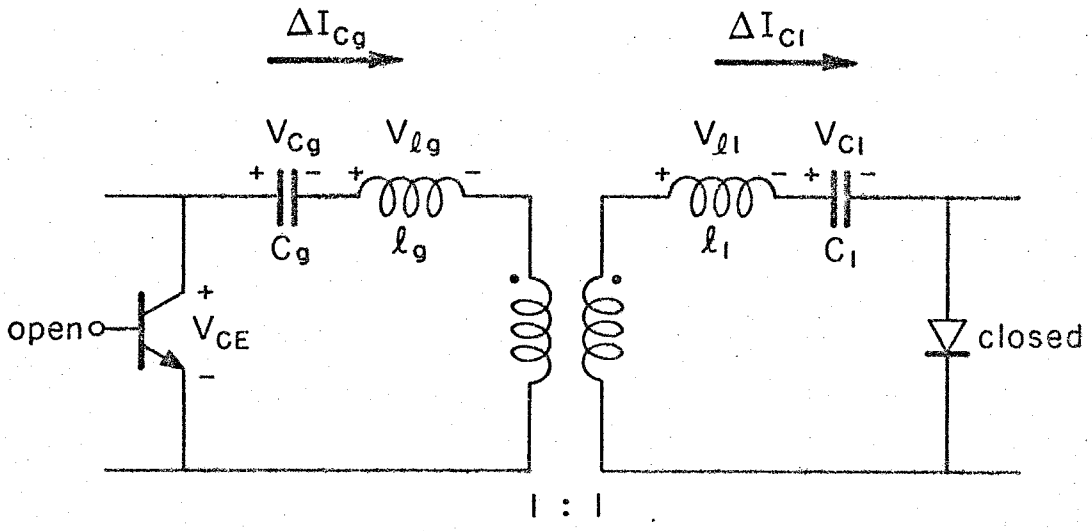

Fig. 14.1 The leakage inductances produce a voltage spike across the transistor during turn-off transient.

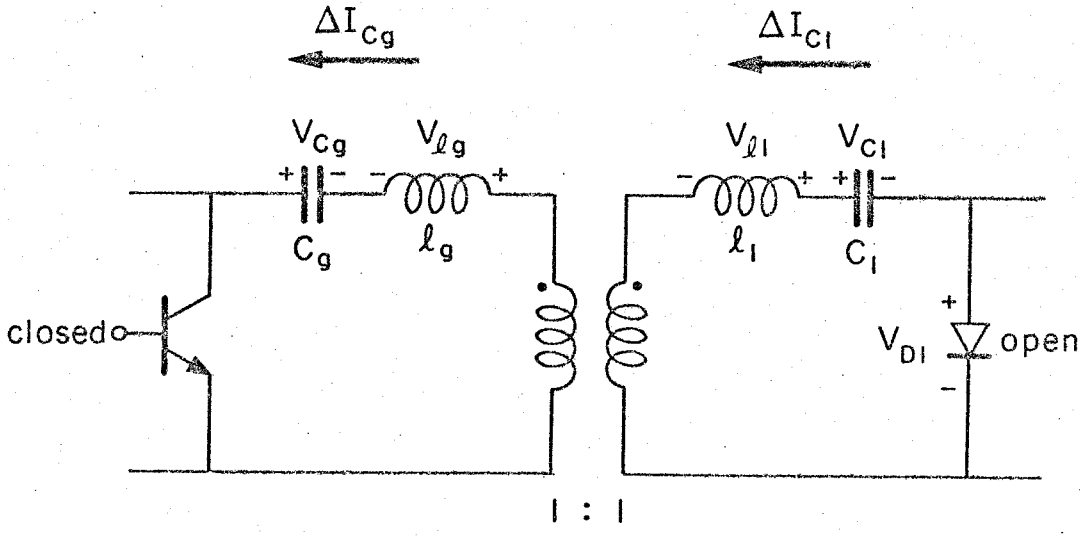

Fig. 14.2 The leakage inductances produce a voltage spike which reduces the back-bias of the diode during transistor turn-on transient.

0.7V even after the transistor is conducting. The length of time when both the transistor and the diode are conducting can be estimated from eq. (14.2) with V_{D1} clamped at 0.7V.

A test circuit, as shown in Fig. 14.3, was built to demonstrate the effect of large leakage inductances. The transformer T was wound on a Ferroxcube ferrite pot core 3019P-L00-3C8. All three windings were made of 70 turns of 26 AWG wire. The magnetizing inductance was measured to be 30 mH and the three leakage inductances are 28 μH, 18 μH, and 5 μH. The waveforms of the diodes are shown in Fig. 14.4. It is seen that diode 1 remains ON for about 2.5 μs after the transistor is fully turned on. The transistor is protected from the big voltage spike during the turn-off transient by a snubber.

In this study of cross-regulation, the leakage inductances will be assumed to be small enough that the converter is operated under normal conditions, i.e., the length of the time when both the transistor and one of the diodes are conducting simultaneously is very small compared with the whole switching period. In other words, the two diodes will be assumed to be turned off simultaneously when the transistor is turned on. Equation (14.2) can be used as a criterion for the validity of this assumption.

14.2 Cross-regulation under the small leakage inductance assumption

With the assumption of small leakage inductances, the effect of parasitics on cross-regulation is now investigated. Figure 14.5(a)

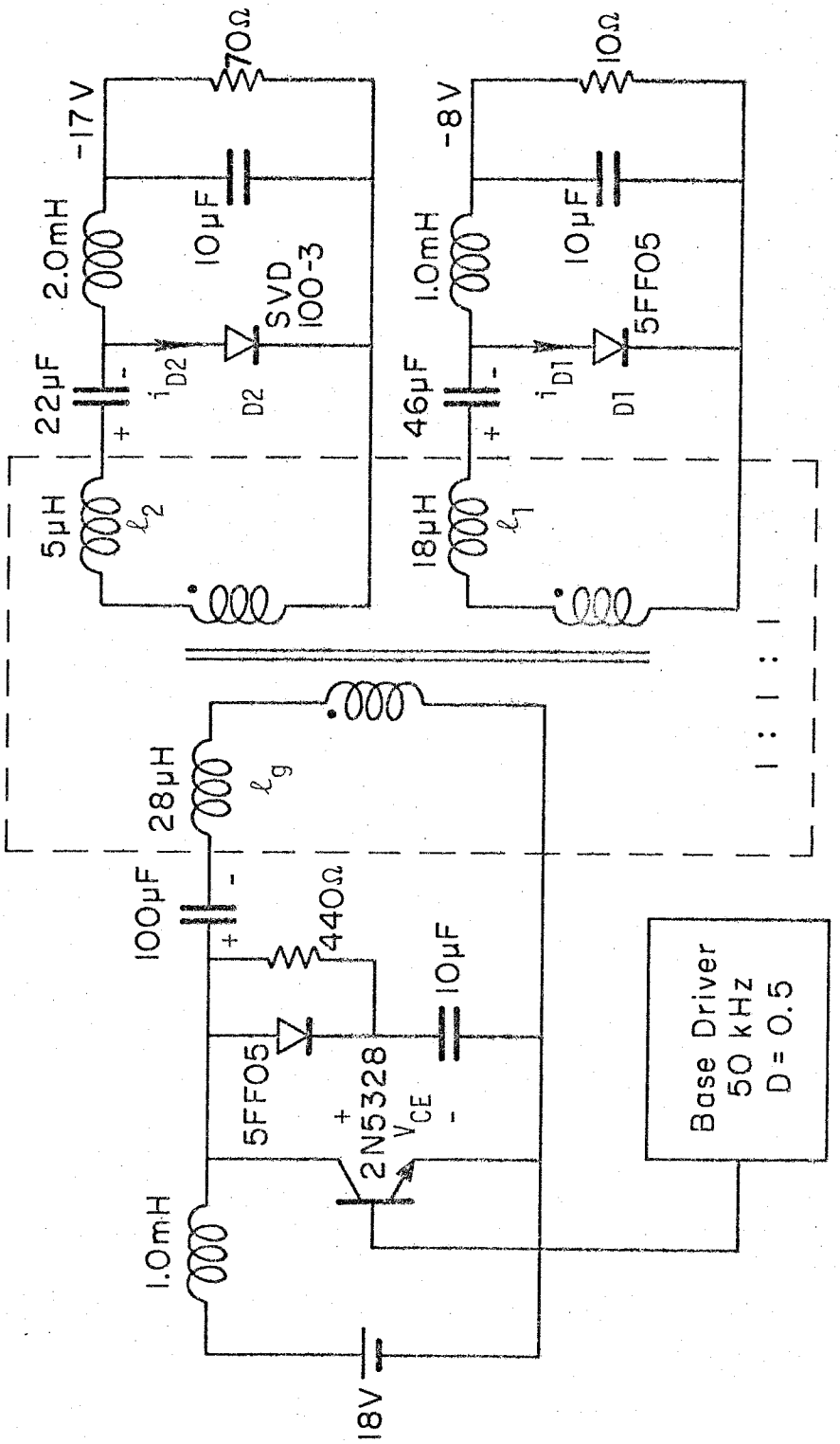

Fig. 14.3 An experimental circuit which shows the effects of large leakage inductances.

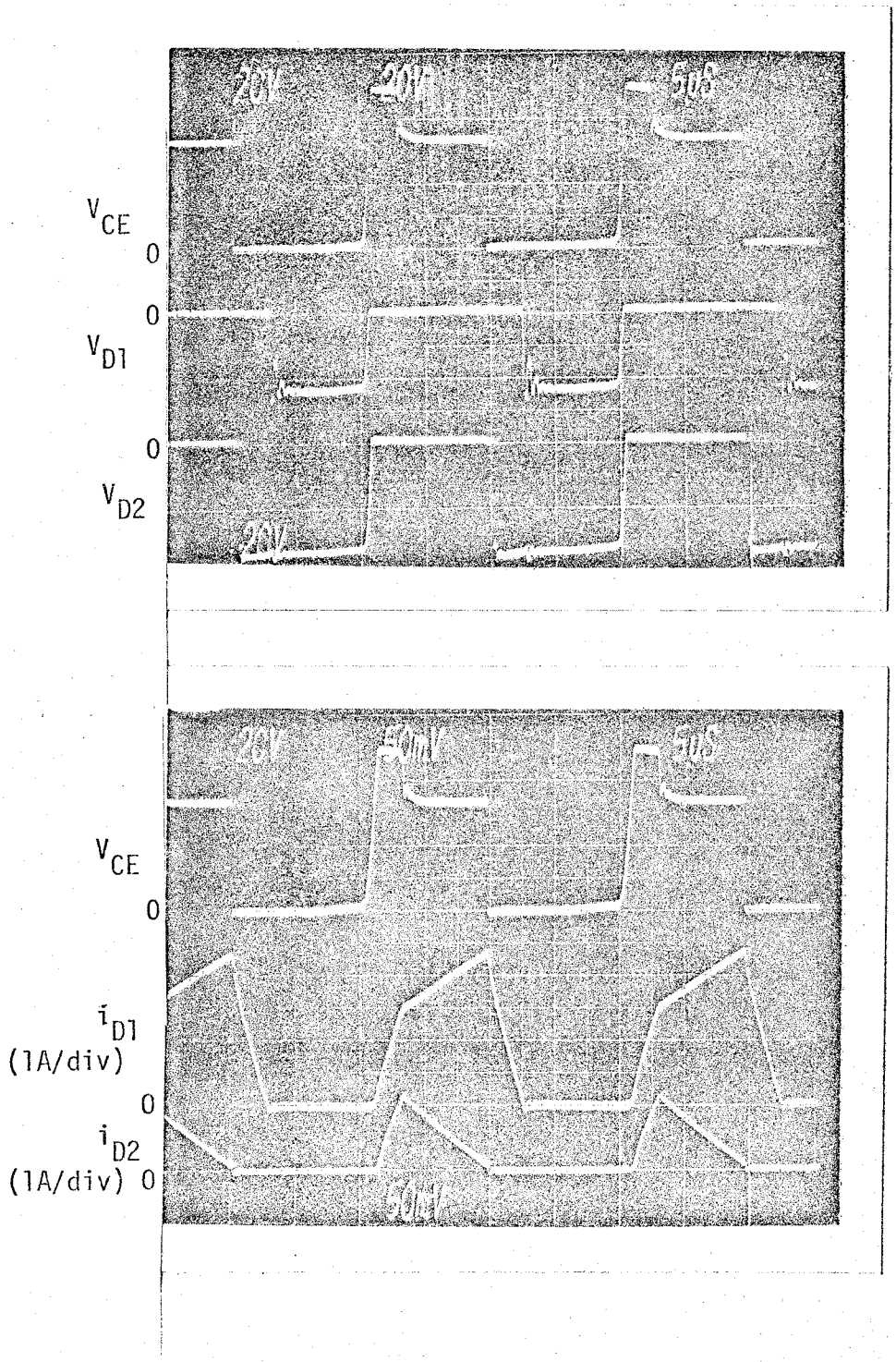

Fig. 14.4 *The voltage and current waveforms of the two diodes in Fig. 14.3.*

is a model of the converter which includes the winding resistances $r_{\ell 1}$ and $r_{\ell 2}$ of the output inductors, the diode offset voltages v_{D1} and v_{D2}, the secondary leakage inductances ℓ_1 and ℓ_2 of the isolation transformer, and the ESRs of the capacitors plus the winding resistances of the transformer r_1 and r_2. Again, the ideal transformer can be removed from the circuit, as shown in Fig. 14.5(b), with circuit element values and state variables properly adjusted for the turns ratio. For simplicity the turns ratio will be assumed to be 1:1:1 as in Fig. 14.6. The result of this section can be generalized to arbitrary turns ratio by simple replacements of $V_1 \rightarrow V_1/n_1$, $i_1 \rightarrow i_1 n_1$, $\ell_1 \rightarrow \ell_1/n_1^2$, $C_1 \rightarrow n_1^2 C_1$, etc.

To separate the effects of output inductor winding resistances and the diode offset voltages from the rest of the parasitics, Fig. 14.6 can be manipulated into Fig. 14.7. Figure 14.7 is equivalent to Fig. 14.6. From Fig. 14.7,

$$\langle v_1 \rangle - \langle v_2 \rangle = \langle v_{C2}' - v_{C1}' \rangle + (v_{D1} - v_{D2}) + (I_1 r_{\ell 1} - I_2 r_{\ell 2}) \qquad (14.3)$$

Note that the average voltages across the ESRs and the inductors, being zero in the steady state, do not appear in eq. (14.3).

To calculate $\langle v_{C2}' - v_{C1}' \rangle$ from the model, it is useful to simplify Fig. 14.7 into Fig. 14.8. Figure 14.7 and Fig. 14.8 are equivalent as far as calculation of v_{C1}' and v_{C2}' is concerned.

The calculation of the cross-regulation of the circuit in Fig. 14.6 has now been separated into three components as shown in eq. (14.3). The first term is the contribution from the series

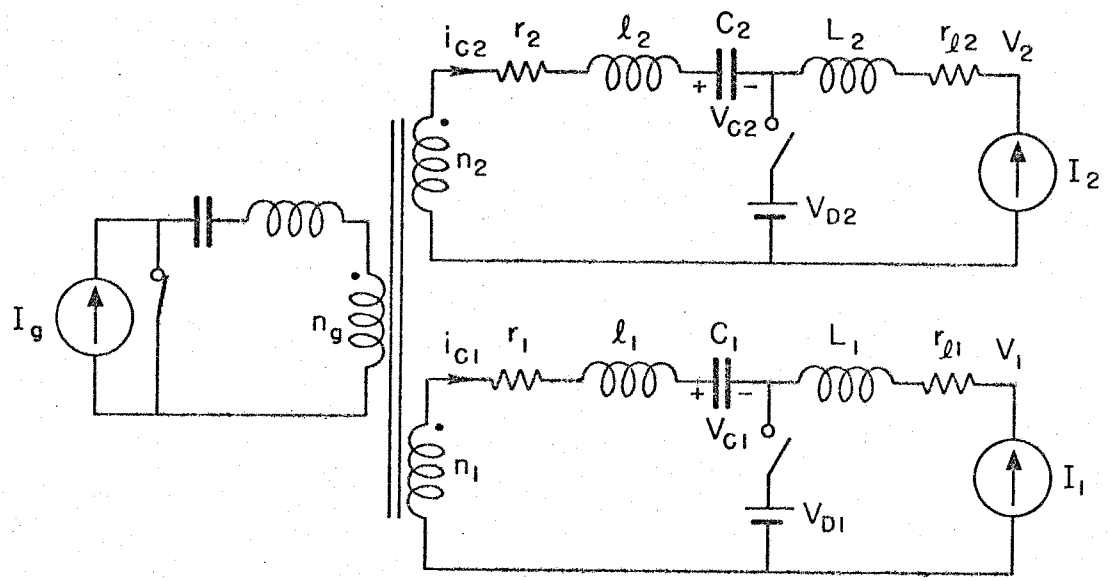

Fig. 14.5(a) The circuit model for a two-output Ćuk converter with component non-idealities included.

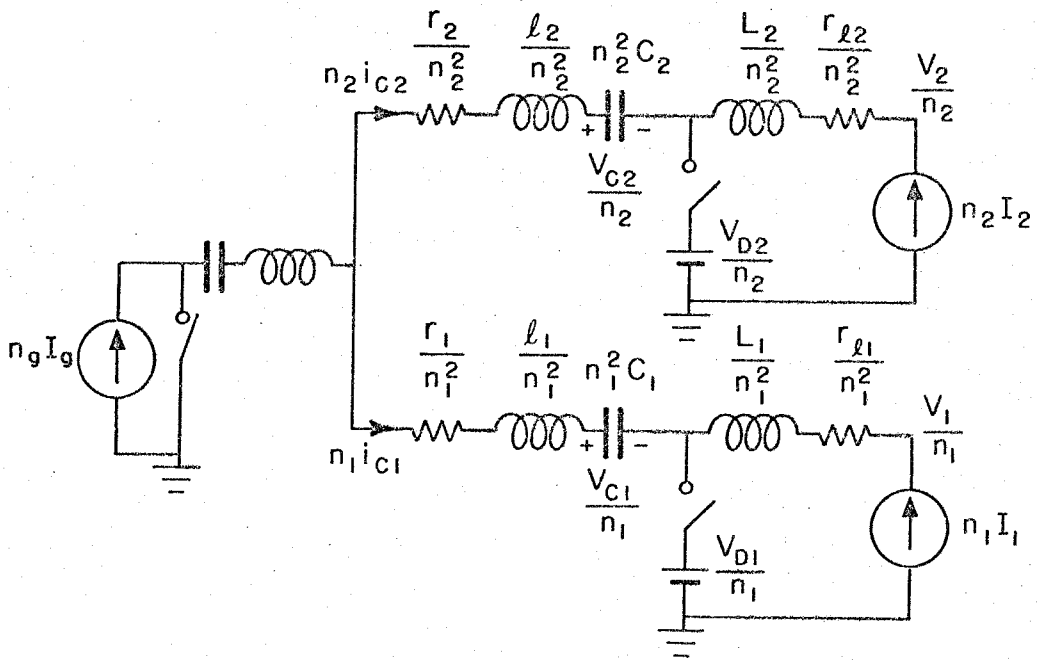

Fig. 14.5(b) The ideal transformer in Fig. 14.5(a) can be removed by properly adjusting the values of the components and their corresponding state variables.

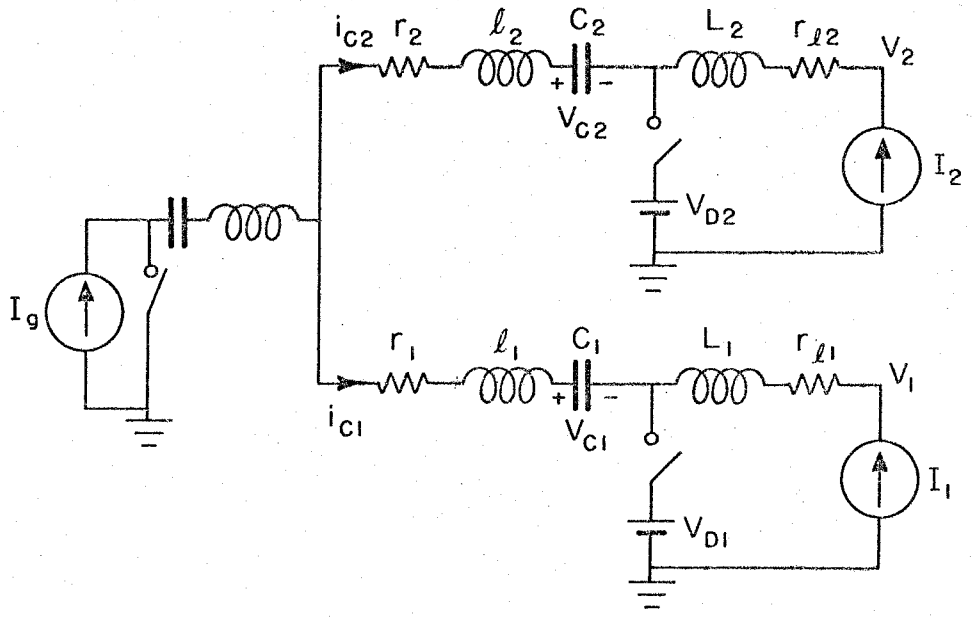

Fig. 14.6 A simplified model of Fig. 14.5(a). The transformer turns ratio is assumed to be 1:1:1.

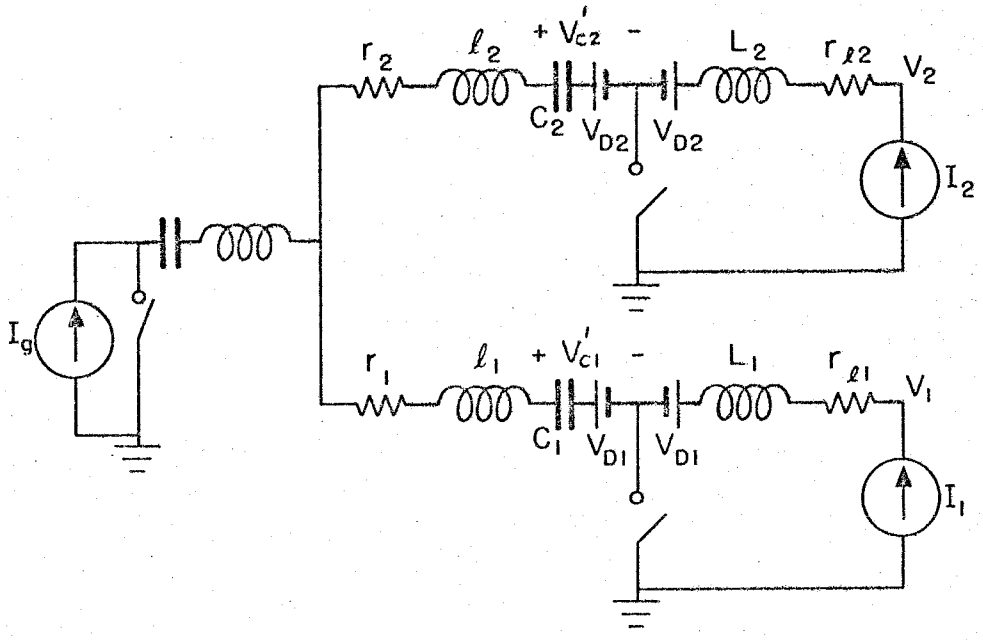

Fig. 14.7 An equivalent circuit model of Fig. 14.6.

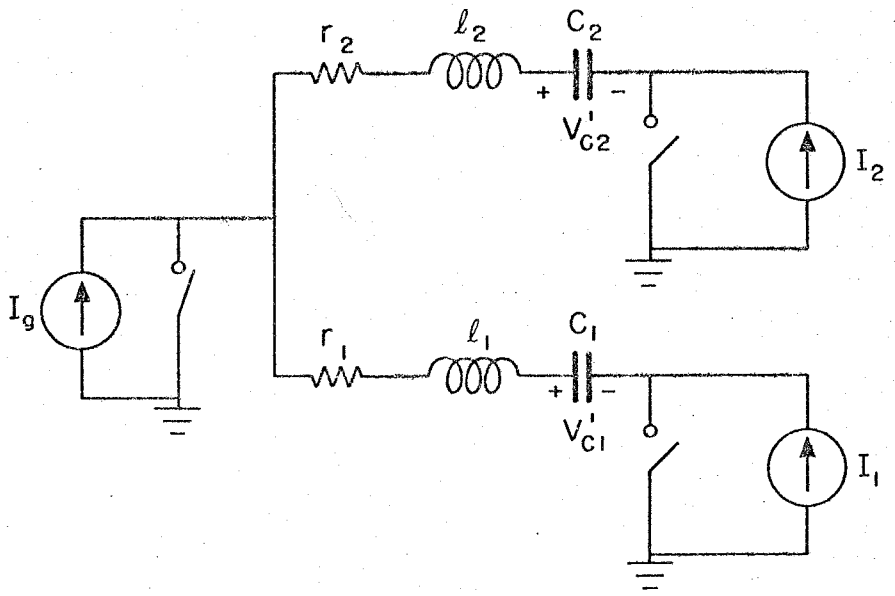

Fig. 14.8 A simplified circuit model which is equivalent to that of Fig. 14.7 as far as calculation of v_{C1}' and v_{C2}' is concerned.

connection of the coupling capacitors, the ESR plus the winding resistance of the transformer and the leakage inductance of the transformer. The second term is the contribution from the diode offset voltages, and the third term is the effect of winding resistances of the output inductors. The last two terms are simple to calculate and easy to understand. The emphasis will now be directed to the first term which will be solved from Fig. 14.8.

The model of Fig. 14.8 is very similar to that of Fig. 13.3 of Chapter 13. Similar procedures will be taken here to calculate the difference of the average voltages of the two coupling capacitors: The capacitor currents will be investigated first. The voltage difference $v_{C2} - v_{C1}$ can then be constructed and its average is the desired first term of eq. (14.3), $\langle v_{C2} - v_{C1} \rangle$.

A typical capacitor current waveform predicted by the model of Fig. 14.8 is shown in Fig. 14.9 with the corresponding $v_{C2}' - v_{C1}'$ plotted in Fig. 14.10. They are explained in the following.

During DT_s when the transistor is conducting, the two diodes are off under the small leakage inductances assumption. The two capacitors are discharged by the load currents, and a voltage difference of

$$\Delta V = \left(\frac{I_1}{C_1} - \frac{I_2}{C_2} \right) DT_s \qquad (14.4)$$

is developed in addition to their initial difference V_o. After the transistor is turned off, the diode 1 will be on and diode 2 may remain off if the voltage difference ΔV of the capacitors is positive. This situation lasts for an interval $D_x T_s$ during which

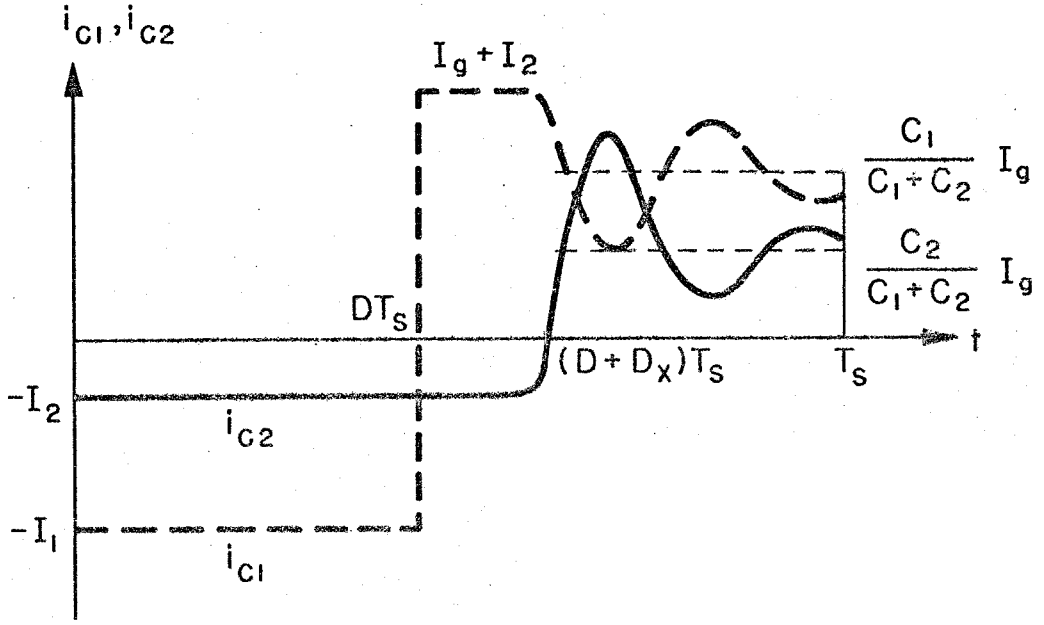

Fig. 14.9 The capacitor current waveforms predicted by the model of Fig. 14.8.

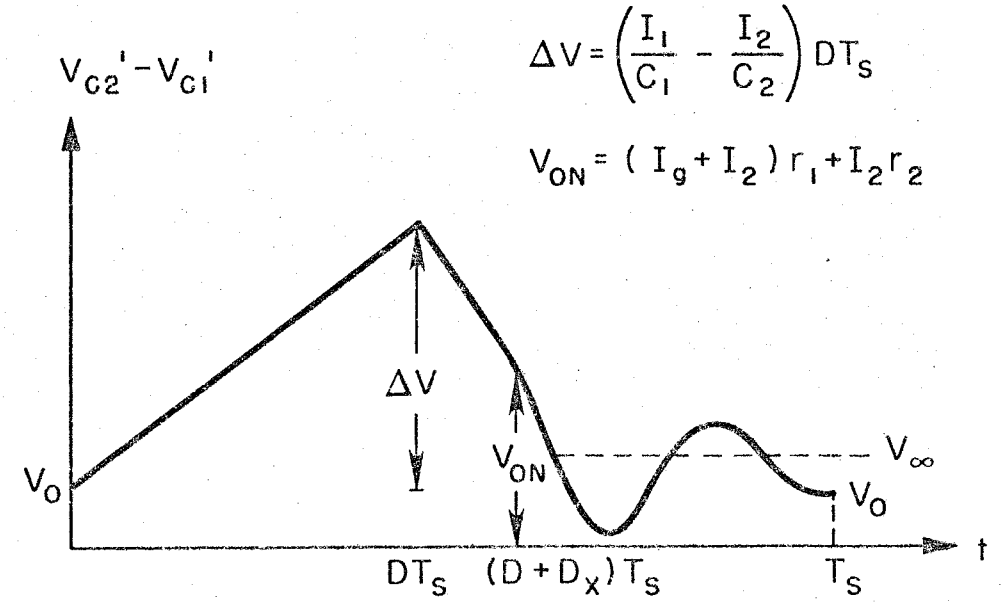

Fig. 14.10 The capacitor voltage difference predicted by the model of Fig. 14.8.

C_1 is charged by I_g+I_2 and C_2 is discharged by I_2. The voltage across diode 2 is brought up from some negative value to zero which occurs when the voltages across the two LRC branches are equal. The capacitor voltage difference at this point is equal to the voltage drop across r_1 and r_2:

$$V_{on} = (I_g+I_2)r_1 + I_2r_2 \tag{14.5}$$

The two diodes then both become conducting and the source current I_g is split into two paths. The current split is governed by the following differential equation:

$$\begin{cases} \dot{i}_{C1}\ell_1 + v_{C1}' + i_{C1}r_1 = \dot{i}_{C2}\ell_2 + v_{C2}' + i_{C2}r_2 \\ i_{C1} + i_{C2} = I_g \end{cases} \tag{14.6}$$

The solutions to eq. (14.6) are of the form:

overdamped ($\alpha > \omega_o$):

$$\begin{cases} i_{C1} = a_1e^{-s_1t} + a_2e^{-s_2t} + \dfrac{C_1}{C_1+C_2} I_g \\ i_{C2} = I_g - i_{C1} \\ v_{C2}' - v_{C1}' = a_3e^{-s_1t} + a_4e^{-s_2t} + \dfrac{C_1r_1-C_2r_2}{C_1+C_2} I_g \end{cases} \tag{14.7}$$

where

$$s_1 = \alpha - \sqrt{\alpha^2-\omega_o^2}$$

$$s_2 = \alpha + \sqrt{\alpha^2-\omega_o^2}$$

$$\alpha = \frac{r_1+r_2}{2(\ell_1+\ell_2)}$$

$$\omega_o^2 = \frac{C_1+C_2}{C_1C_2(\ell_1+\ell_2)}$$

critically damped ($\alpha = \omega_o$):

$$\begin{cases} i_{C1} = (k_1+k_2t)e^{-\alpha t} + \dfrac{C_1}{C_1+C_2} I_g \\ i_{C2} = I_g - i_{C1} \\ v_{C2}' - v_{C1}' = (k_3+k_4t)e^{-\alpha t} + \dfrac{C_1r_1-C_2r_2}{C_1+C_2} I_g \end{cases} \tag{14.8}$$

underdamped ($\alpha < \omega_o$):

$$\begin{cases} i_{C1} = b_1 d^{-\alpha t}\cos(\omega_d t+\theta_1) + \dfrac{C_1}{C_1+C_2} I_g \\ i_{C2} = I_g - i_{C1} \\ v_{C2}' - v_{C1}' = b_2 e^{-\alpha t}\cos(\omega_d t+\theta_2) + \dfrac{C_1r_1-C_2r_2}{C_1+C_2} I_g \end{cases} \tag{14.9}$$

where

$$\omega_d = \sqrt{\omega_o^2-\alpha^2}$$

The average value under the curve of $v_{C2}'-v_{C1}'$ will contribute to the cross-regulation as the first term in eq. (14.3). A complete solution is quite involved and does not provide further insight into the problem. A qualitative discussion is instead given in the following.

14.3 Possibilities of overdamping and underdamping

It is seen from the solutions that the system is underdamped, critically damped or overdamped, depending on the relative sizes of the resistances (r_1+r_2) and r_o, where $r_o \equiv \sqrt{\dfrac{(C_1+C_2)(\ell_1+\ell_2)}{C_1C_2}}$

is the characteristic resistance of the two leakage inductances in series with the two coupling capacitances. A test circuit as shown in Fig. 14.11 is constructed to demonstrate this effect. The transformer T_1 was wound on a Magnetics 52133-1F Supermalloy core with winding 1 and winding 2 bifilar on one side of the core and a single layer primary winding on the other side of the core. This arrangement produces a relatively large leakage inductance of 7.5 μH on the primary side and small leakage inductances of 0.3 μH on the bifilar windings. All three windings were made of 18 turns of 26 AWG wire which produced a 0.14Ω resistance on each winding. The capacitor current waveforms together with the equivalent circuit models under three cases are shown in Fig. 14.12. Figure 14.12(a) is a typical waveform of the underdamped case. Diode 2 remains OFF until 2 μs after diode 1 is conducting. Notice that the final values of i_{C1} and i_{C2} are equal as predicted by eq. (14.9), and the oscillation frequency is close to the expected value. Figure 14.12(b) is the waveform of the same circuit as used in Fig. 14.12(a) except that the transformer primary winding is exchanged with the winding 2. This increases the value of $\ell_1+\ell_2$ from 0.6 μH to 7.8 μH. By comparison of Fig. 14.12(b) with Fig. 14.12(a), it is clear that the damping time constant $1/\alpha$ is increased and the oscillation frequency ω_d is reduced, as expected from eq. (14.9). Notice that i_{C1} can go negative as long as the diode current is positive. Again, the two capacitor currents are approaching the same final value because of the same capacitance values. Figure 14.12(c)

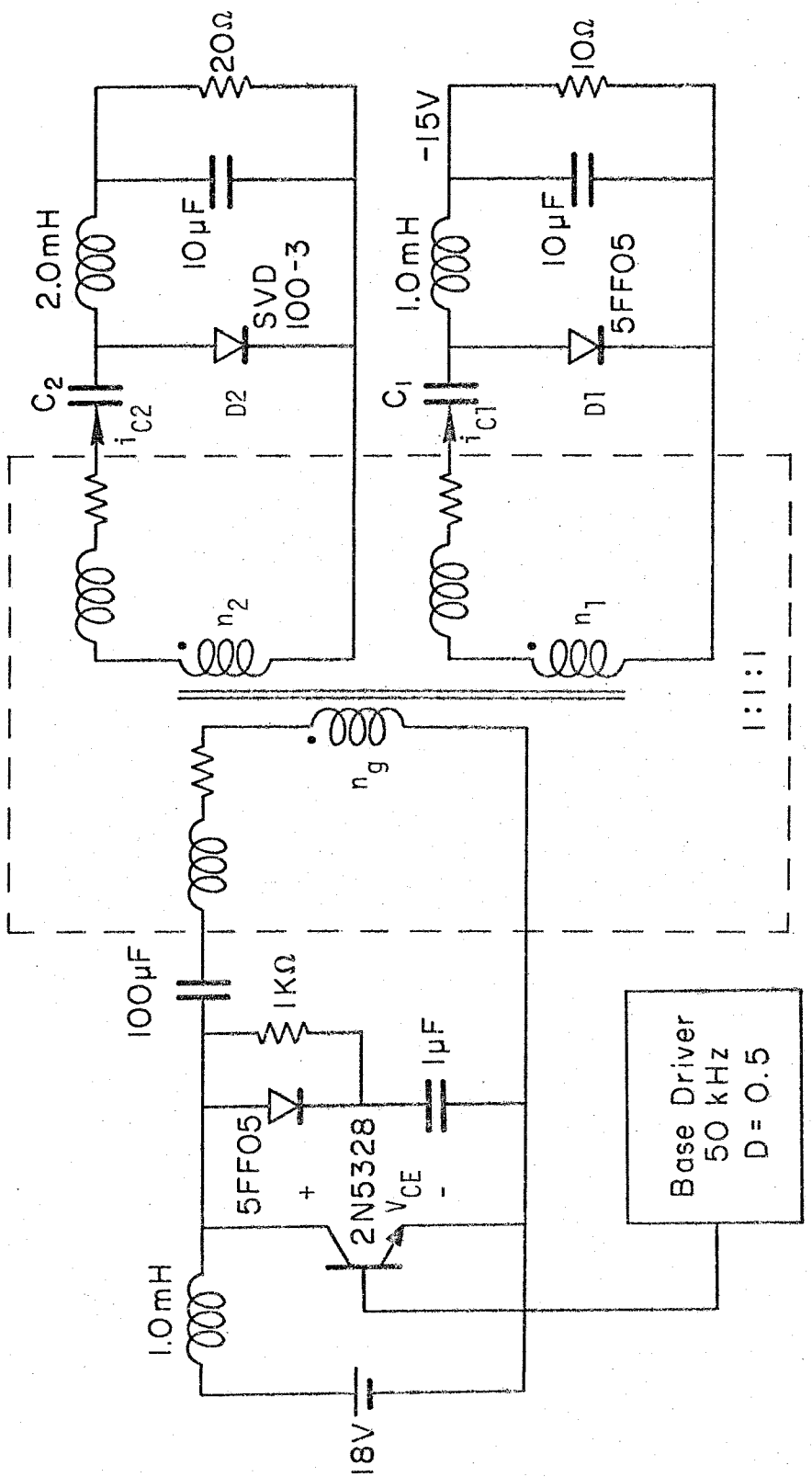

Fig. 14.11 An experimental circuit which shows that the system can be either underdamped or overdamped depending on the relative size of $r_1 + r_2$ *and* $\sqrt{(C_1 + C_2)(\ell_1 + \ell_2)/C_1C_2}$.

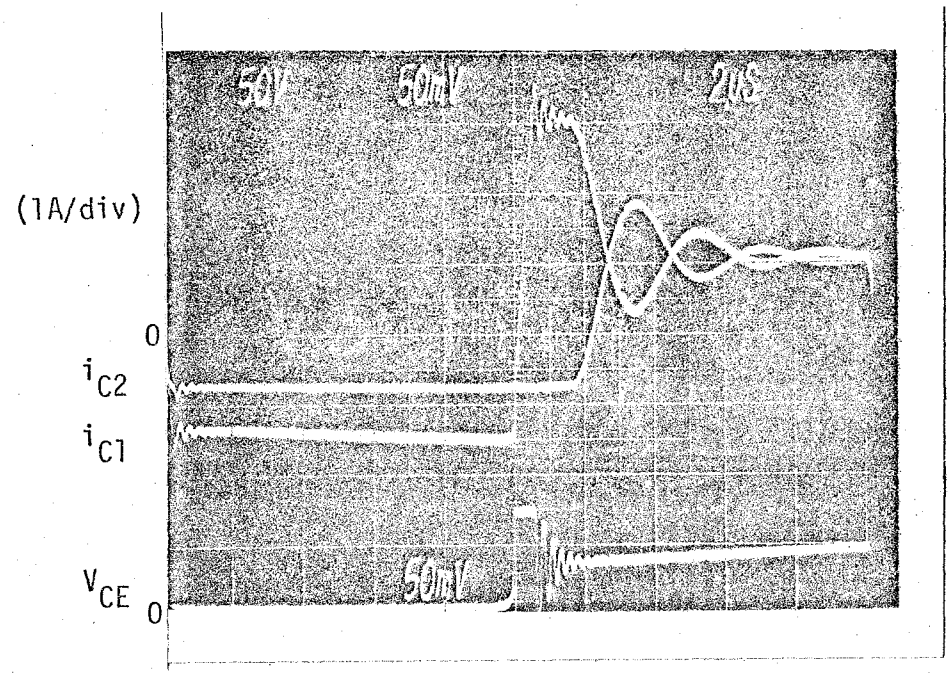

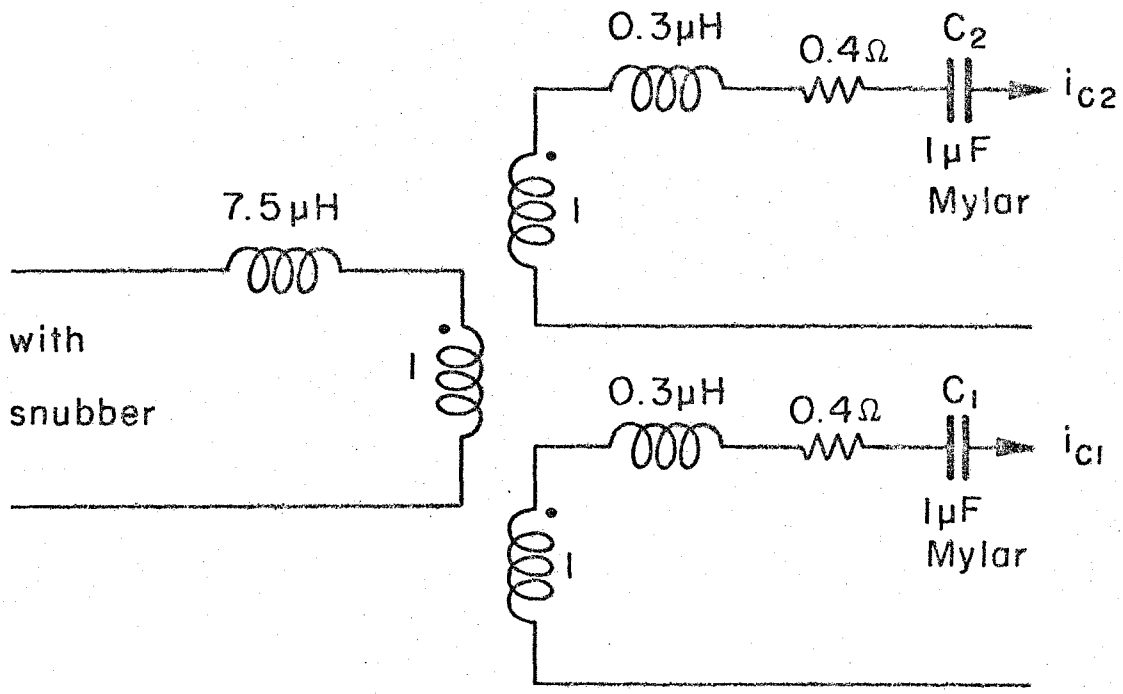

a) Underdamped

Fig. 14.12(a) The observed underdamped capacitor current waveforms and the component values used.

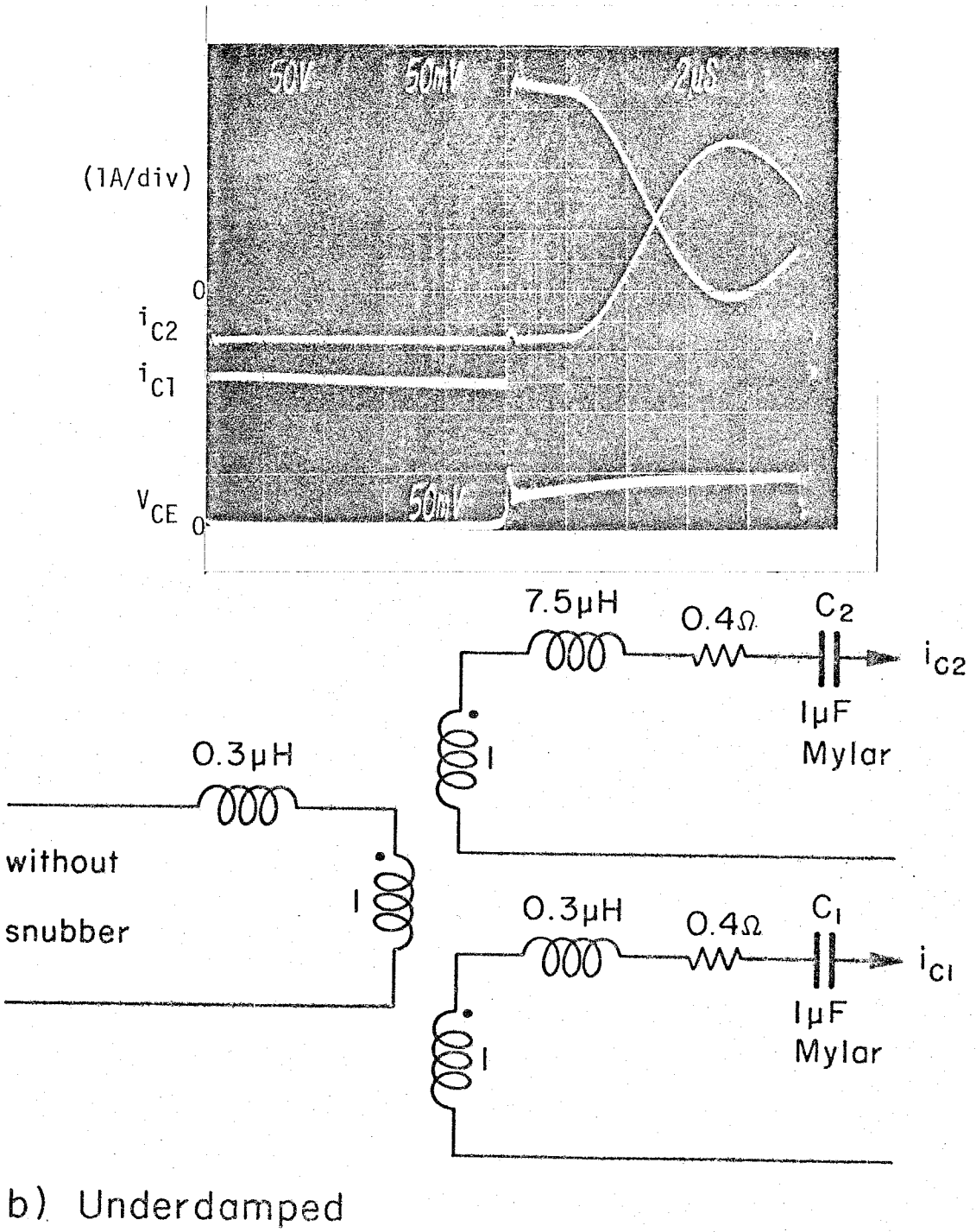

b) Underdamped

Fig. 14.12(b) *The frequency of oscillation of the waveforms in Fig. 14.12(a) was reduced when the leakage inductance ℓ_1 was increased.*

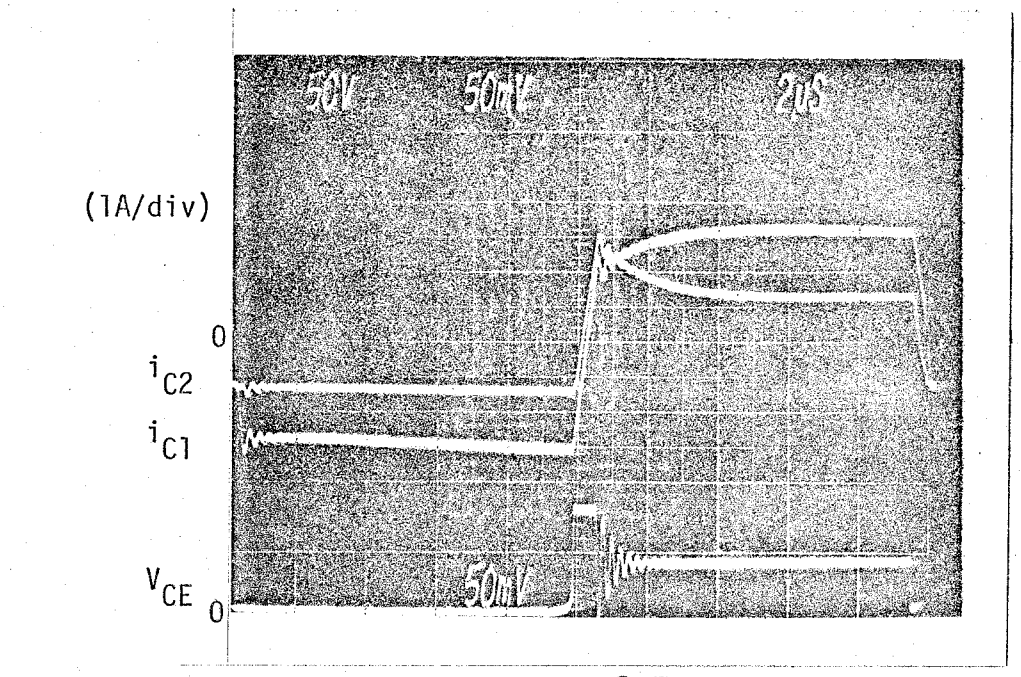

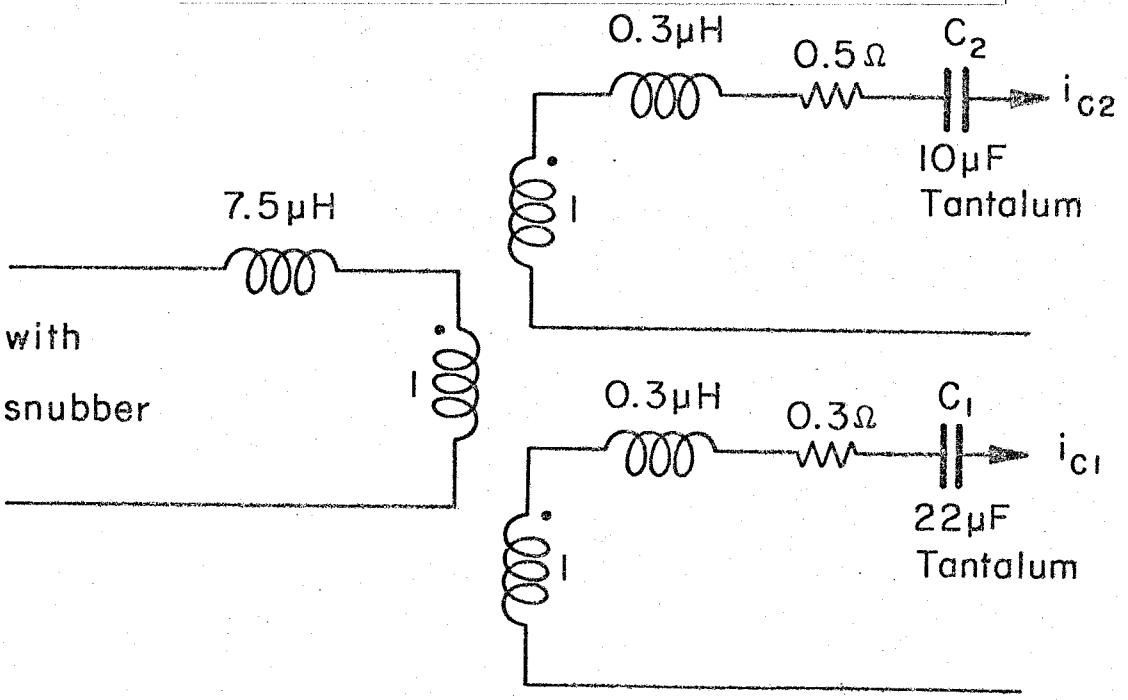

c) Overdamped

Fig. 14.12(c) The system was overdamped when the values of the capacitances C_1 and C_2 were increased.

shows that the system can be operated in the overdamped case if the capacitance values are increased. The circuit for Fig. 14.12(c) is identical to that for Fig. 14.12(a) except that the two capacitors C_1 and C_2 are increased from 1 μF to 22 μF and 10 μF, respectively. This reduces the value of the characteristic resistance $r_o = \sqrt{(C_1+C_2)(\ell_1+\ell_2)/C_1C_2}$ and the system is overdamped. The final value of i_{C1} is about twice that of i_{C2} because C_1 is twice the value of C_2. Notice that the two diodes turn on simultaneously. This is another effect of increasing the capacitance values. It is seen from Fig. 14.10 that the voltage difference between the two capacitors ΔV is reduced when C_1 and C_2 are increased. If the two capacitors are large enough, the peak of the capacitor voltage difference $v_{C2}'-v_{C1}'$ at $t=DT_s$ may be smaller than V_{on}. In this case, the two diodes turn on simultaneously. In other words, the unequal discharge of the two capacitors in a two-output Ćuk converter usually cause one diode to turn on before the other. However, if the voltage difference resulting from the unequal discharge is smaller than the sum of the voltage drops on the ESRs of the capacitors and the winding resistances of the transformer, the two diodes still turn on simultaneously. This is apparently the more desirable case, not only because the two diodes have the same duty ratio but also because it means closer cross-regulation. Figure 14.13 is a reduced version of Fig. 14.10. It is seen that the cross-regulation $\langle v_{C2}'-v_{C1}' \rangle$ is always smaller than

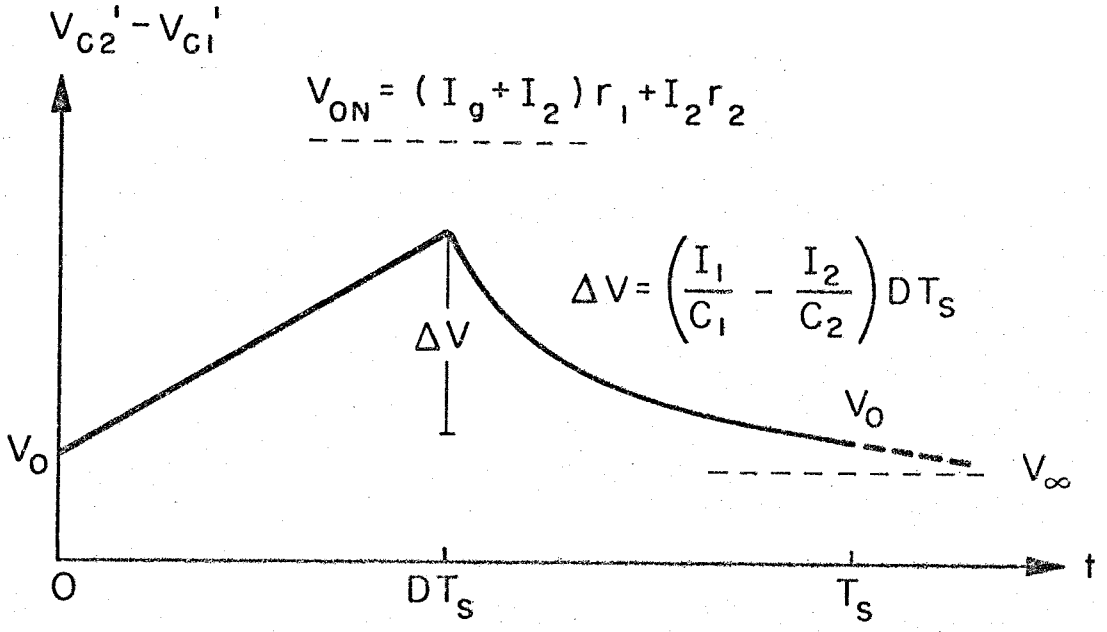

Fig. 14.13 The waveform of the voltage difference between the two capacitors if the two diodes turn on simultaneously.

$V_{on} = (I_g+I_2)r_1+I_2r_2$. Some qualitative results can be drawn from inspection of Fig. 14.13. The cross-regulation can be improved by reduction of the voltage difference between the two capacitors ΔV, the final value of the voltage difference V_∞ and the time constants of the exponential curve during $D'T_s$. These can be achieved by increase in the sizes of the coupling capacitors C_1 and C_2, and reduction of the sizes of the ESRs and leakage inductances.

14.4 Cross-regulation in overdamped condition

Since it is always possible to increase the capacitor sizes to force the system into the overdamped operation and cause the two diodes to turn on simultaneously, with the benefit of close cross-regulation, the case shown in Fig. 14.13 will be solved in detail in the following.

During DTs, the waveform of Fig. 14.13 is just a straight line. During $D'T_s$, the waveform can be described by the following equation:

$$\ell_1 \dot{i}_{C1} + i_{C1}r_1 + v_{C1}' = \ell_2 \dot{i}_{C2} + i_{C2}r_2 + v_{C2}' \tag{14.10}$$

$$\dot{v}_{C1}' = i_{C1}/C_1 \tag{14.11}$$

$$\dot{v}_{C2}' = i_{C2}/C_2 \tag{14.12}$$

$$i_{C1} + i_{C2} = I_g - mt \tag{14.13}$$

where $-m$ is the down slope of the input inductor current

$$\int_0^{D'T_s} i_{C1}(t)dt = I_1 DT_s \tag{14.14}$$

Equations (14.10) through (14.13) can be combined into

$$\ddot{i}_{C1} + 2\alpha\dot{i}_{C1} + \omega_o^2 i_{C1} = \omega_o^2 \frac{C_1}{C_1+C_2}(I_g - mt - mr_2C_2) \tag{14.15}$$

and

$$\ddot{v} + 2\alpha\dot{v} + \omega_o^2 v = \omega_o^2 \frac{1}{C_1+C_2}[(C_2r_1 - C_1r_2)(I_g - mt) - m(\ell_1C_1 - \ell_2C_2)] \tag{14.16}$$

where

$$\alpha = \frac{r_1+r_2}{2(\ell_1+\ell_2)}$$

$$\omega_o^2 = \frac{C_1+C_2}{C_1C_2(\ell_1+\ell_2)}$$

$$v \equiv v_{C2}' - v_{C1}'$$

Those terms with coefficient m on the right-hand side of eqs. (14.15), (14.16) are the effect of the slope of the inductor current. They will be neglected in the following analysis because they are usually small. The initial condition $i_{C1}(0)$ can be evaluated by consideration of the transient when the transistor turns off during the interval t_{off}. As a first-order approximation, it can be assumed that the voltages across the two leakage inductances ℓ_1 and ℓ_2 are equal during the transient, because the voltages across the resistors r_1 and r_2, and the voltage difference on the two capacitors C_1 and C_2 are relatively small. Therefore,

$$\ell_1 \cdot \frac{i_{C1}(0) + I_1}{t_{off}} = \ell_2 \cdot \frac{I_g - i_{C1}(0) + I_2}{t_{off}} \tag{14.17}$$

or

$$i_{C1}(0) = \frac{\ell_2(I_g+I_2) - \ell_1 I_1}{\ell_1 + \ell_2} \tag{14.18}$$

Equations (14.14) and (14.18) can be used as two boundary conditions to solve eqs. (14.15) and (14.16) completely:

$$i_{C1}(t) = ae^{-s_1 t} + be^{-s_2 t} + \frac{C_1}{C_1+C_2} I_g \tag{14.19}$$

where

$$a = i_{C1}(0) - \frac{C_1}{C_1+C_2} I_g - b$$

$$b = \frac{\frac{s_2 C_1 C_2}{C_1+C_2}\Delta V - \left[i_{C1}(0) - \frac{C_1}{C_1+C_2} I_g\right]\left(\frac{s_2}{s_1}\right)\left(1-e^{-s_1 D' T_s}\right)}{\left(1-e^{-s_2 D' T_s}\right) - \left(\frac{s_2}{s_1}\right)\left(1-e^{-s_1 D' T_s}\right)}$$

$$s_1, s_2 = \frac{r_1+r_2}{2(\ell_1+\ell_2)}\left[1 \pm \sqrt{1 - \frac{(C_1+C_2)(\ell_1+\ell_2)}{C_1 C_2 (r_1+r_2)^2}}\right]$$

$$\Delta V = \left(\frac{I_1}{C_1} - \frac{I_2}{C_2}\right) D T_s$$

and

$$v_{C2}' - v_{C1}' = ce^{-s_1 t} + de^{-s_2 t} + \frac{C_1 r_1 - C_2 r_2}{C_1+C_2} I_g \tag{14.20}$$

where

$$c = \frac{\frac{-s_2}{s_1}\Delta V + \left[\frac{C_1+C_2}{C_1 C_2} i_{C1}(0) - \frac{I_g}{C_2}\right]\left(\frac{1}{s_1}\right)\left(1-e^{-s_2 D' T_s}\right)}{\left(1-e^{-s_2 D' T_s}\right) - \left(\frac{s_2}{s_1}\right)\left(1-e^{-s_1 D' T_s}\right)}$$

$$d = \frac{\Delta V - \left[\frac{C_1+C_2}{C_1C_2} i_{C1}(0) - \frac{I_g}{C_2}\right]\left(\frac{1}{s_1}\right)\left(1-e^{-s_1 D'T_s}\right)}{\left(1-e^{-s_2 D'T_s}\right) - \left(\frac{s_2}{s_1}\right)\left(1-e^{-s_1 D'T_s}\right)}$$

With eq.(14.20), the cross-regulation can be evaluated by taking the average value of the curve in Fig. 14.13 and adding the effects of diode offset voltage and the resistances of the output inductors, as shown in eq. (14.3). With the assumption that $e^{-s_1 D'T_s} \ll e^{-s_2 D'T_s}$, the result is

$$\langle v_1 \rangle - \langle v_2 \rangle$$

$$\simeq \frac{\Delta V}{2} D + V_\infty + \left(v_{D1} - v_{D2}\right) + \left(I_1 r_{\ell 1} - I_2 r_{\ell 2}\right)$$

$$+ \left\{ \begin{array}{l} s_1 \Delta V \cdot \left[1-(s_2/s_1)^2 - (1-s_2T_s)e^{-s_2 D'T_s}\right] \\ - \left[(C_1+C_2) i_{C1}(0)/C_1C_2 - I_g/C_2\right]\left[1-(s_2/s_1) - (1-s_2/s_1-s_2T_s)e^{-s_2 D'T_s}\right] \end{array} \right\}$$

$$\Big/ \; s_1 s_2 T_s \left[1-(s_2/s_1)-e^{-s_2 D'T_s}\right] \qquad (14.21)$$

where

$$\Delta V = \left(\frac{I_1}{C_1} - \frac{I_2}{C_2}\right) DT_s$$

$$V_\infty = \frac{C_1 r_1 - C_2 r_2}{C_1+C_2} I_g$$

$$i_{C1}(0) = \frac{\ell_2 (I_g+I_2) - \ell_1 I_1}{\ell_1 + \ell_2}$$

$$I_g = (I_1+I_2)\frac{D}{D'}$$

The first term on the right side of eq. (14.21) comes from the unique effect of unequal discharge of the energy transfer capacitances C_1 and C_2 in the Ćuk converter. It is seen that by increasing the values of the capacitances C_1 and C_2 , this first term may be made small compared with the effects of circuit non-idealities which are common to most dc-to-dc converters.

If the turns ratio of the isolation transformer is not 1:1:1, the result in eq. (14.21) can be modified by the replacement $v_1 \rightarrow v_1/n_1$, $i \rightarrow i_1 n_1$, $\ell_1 \rightarrow \ell_1/n_1^2$, $C_1 \rightarrow n_1^2 C_1$ etc. Notice that the diode offset voltage term would contribute $v_{D2}-(n_2/n_1)v_{D1}$ to the deviation of the slaved output $\langle v_2 \rangle - (n_2/n_1)\langle v_1 \rangle$. If n_2/n_1 is large, the diode offset voltage term can be very important. The transformer turns ratio has to be trimmed to compensate this term.

The circuit shown in Fig. 14.14 was constructed to verify the prediction of the cross-regulation eq. (14.21) under the overdamped case. The power switch of the test circuit was operated at 20kHz with duty ratio D=0.5. The output voltage V_1 was fixed at -15V, and the difference between V_2 and V_1 was measured. The parasitics in the

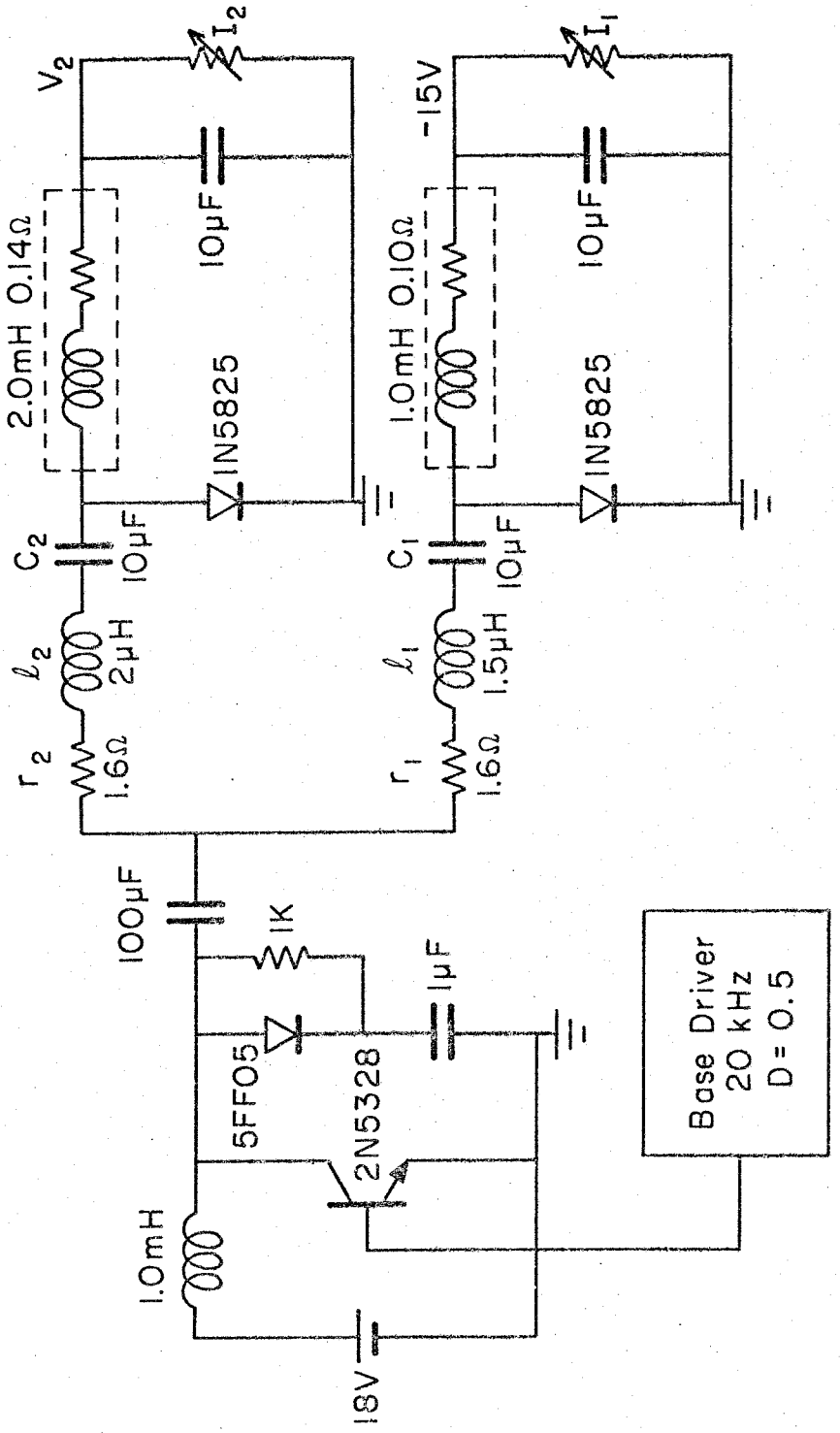

Fig. 14.14 An experimental circuit used to verify the prediction of the cross-regulation.

circuit are all artificial so that their values can be better controlled. External inductances ℓ_1 and ℓ_2 were used to simulate the leakage inductances of the isolation transformer. Since the system is overdamped and the two diodes turn on simultaneously, eq. (14.21) can be applied. Figure 14.15 is the prediction and the experimental data of the self-regulation of the output V_2 when the load current I_2 varies from 0.2A to 1.0A, with I_1 fixed at 0.6A. Figure 14.16 is the prediction and the experimental data of the cross-regulation of V_2 when the load current I_1 varies from 0.2A to 2A, with I_2 fixed at 0.5A. Since the turns ratio is 1:1:1, the effect of the diode offset voltage was not included in the prediction. The data agree quite well with the prediction. Note that C_1 and C_2 are only 10 μF. The cross-regulation can be easily improved by increasing the values of these two capacitances.

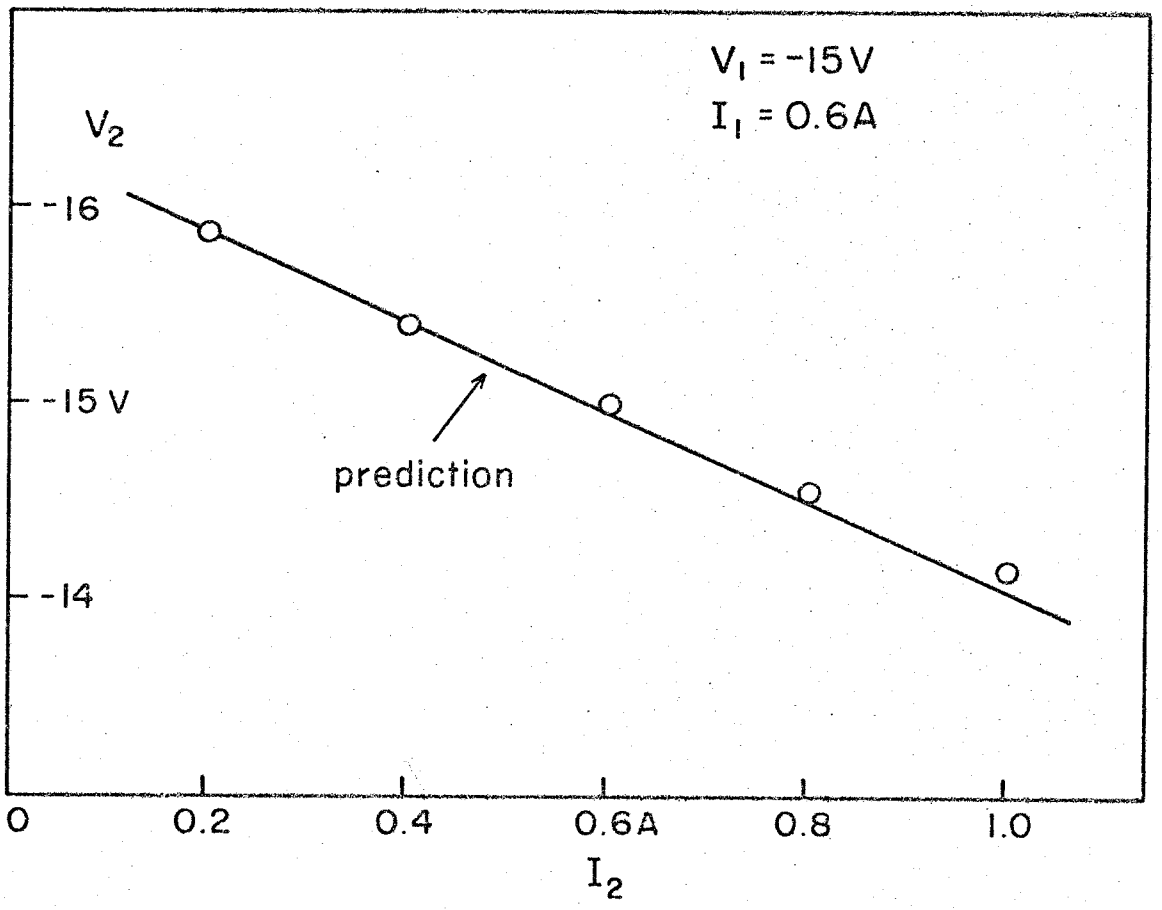

Fig. 14.15 Prediction and experimental data of the self-regulation of the circuit in Fig. 14.14.

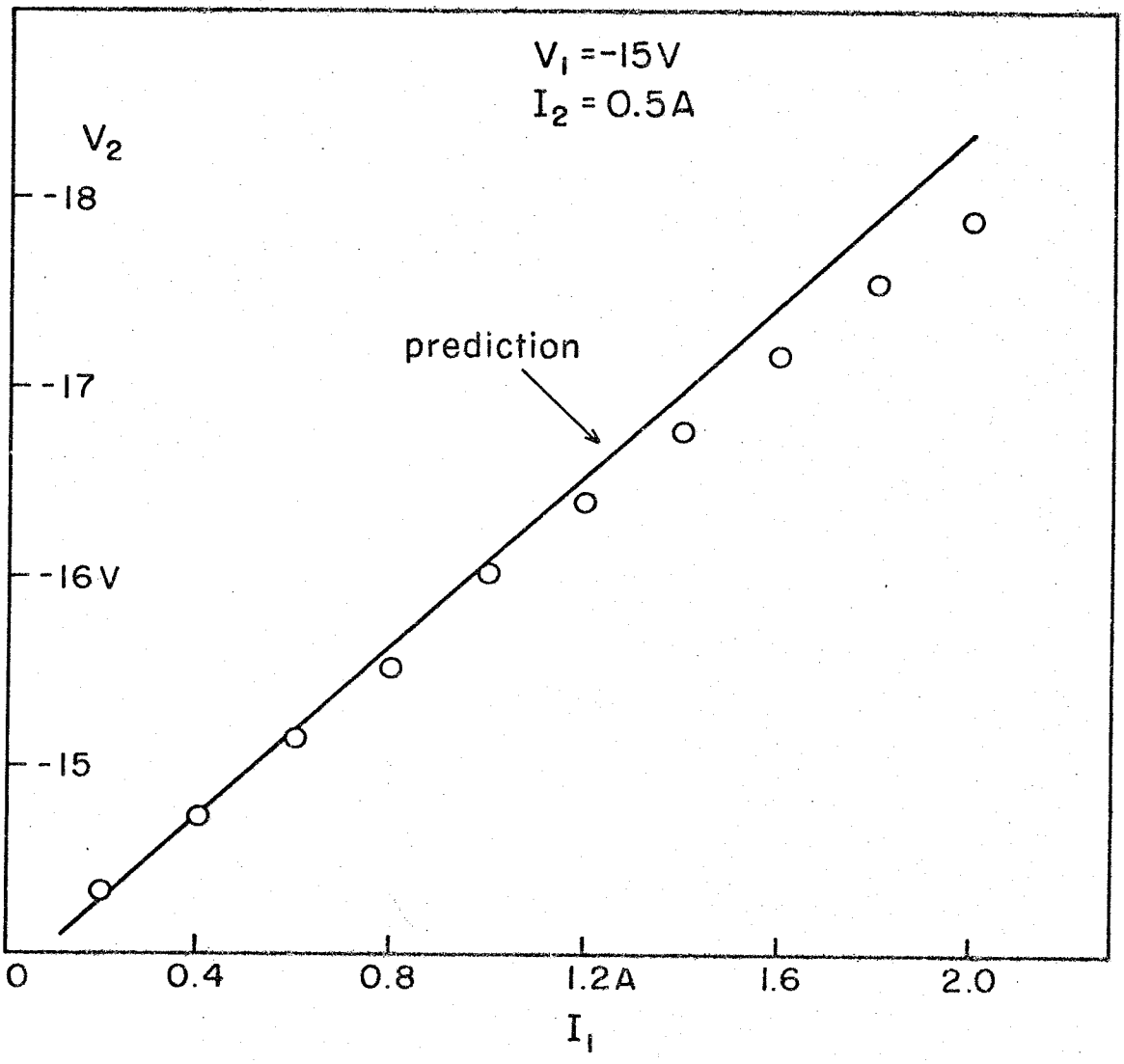

Fig. 14.16 Prediction and experimental data of the cross-regulation of the circuit in Fig. 14.14.

CHAPTER 15

CONCLUSIONS

The imperfect cross-regulation of a switching regulator usually results from the non-idealities in the circuit, such as winding resistances of the inductors and transformers, the ESRs of the capacitors, the offset voltages of the diodes, and the leakage inductances of the isolation transformer. In the case of the multiple-output Ćuk converter, the unequal discharge rates on the coupling capacitors contribute an extra term to the cross-regulation. This problem was discussed in Chapter 13, and it was shown that this effect can be made arbitrarily small by increasing the sizes of the coupling capacitors on the secondary side of the isolation transformer. It was also pointed out that the sizes of these capacitors do not limit the dynamics of the regulator because the coupling capacitor on the primary side of the transformer can be made small.

The effects of the leakage inductances, the winding resistances, the ESRs, and the diode offset voltages, together with the effect of the coupling capacitors were discussed in Chapter 14. It was shown that the effects of the diode offset voltages and the winding resistances of the output inductors can be important if the turns ratio of the transformer is large. In that case, the turns ratio has to be pre-adjusted for good regulations on the slaved outputs.

The leakage inductances of the isolation transformer can be

the most important parasitics in the operation of the multiple-output Ćuk converter. The leakage inductances cause a big spike across the transistor when the transistor is turning off, and prohibit the diodes from turning off simultaneously when the transistor is turning on. A criterion was given in Sec. 14.1 and the leakage inductances were assumed to be smaller than these values so that the diodes practically turn off simultaneously. It was also shown that the diodes will turn on simultaneously if the coupling capacitors are large enough.

The ultimate goal of close regulation can be achieved by minimizing the average value of the voltage difference between the two coupling capacitors. This can be realized by increasing the sizes of these two capacitors so that the voltage difference developed during the transistor ON time is small. This difference will die out toward its final value with a faster time constant if the coupling capacitors are large and the leakage inductances are small. Finally, the final value will be small if the ESRs are small or if they match the values of the capacitances.

REFERENCES

[1] R. D. Middlebrook and Slobodan Ćuk, "A General Unified Approach to Modelling Switching-Converter Power Stages," IEEE Power Electronics Specialists Conference, 1976 Record, pp. 18-34, (IEEE Publication 76CH1084-3 AES); also International J. of Electronics, vol. 42, no. 6, pp. 521-550, June 1977.

[2] Slobodan Ćuk and R. D. Middlebrook, "A General Unified Approach to Modelling Switching Dc-to-Dc Converters in Discontinuous Conduction Mode," IEEE Power Electronics Specialists Conference, 1977 Record, pp. 36-57, (IEEE Publication 77CH 1213-8 AES).

[3] R. D. Middlebrook, "A Continuous Model for the Tapped-Inductor Boost Converter," IEEE Power Electronics Specialists Conference, 1975 Record, pp. 63-79 (IEEE Publication 75 CHO 965-4-AES).

[4] R. D. Middlebrook, "Input Filter Considerations in Design and Application of Switching Regulators," IEEE Industry Applications Society Annual Meeting, 1976 Record, pp. 366-382 (IEEE Publication 76CH1122-1-IA).

[5] R. Haynes, T. K. Phelps, J. A. Collins, and R. D. Middlebrook, "The Venable Converter: A New Approach to Power Processing," IEEE Power Electronics Specialists Conference, 1976 Record, pp. 92-103, (IEEE Publication 76CH1084-3 AES).

[6] R. D. Middlebrook, "Design Techniques for Preventing Input-Filter Oscillations in Switched-Mode Regulators," Proc. Fifth National Solid-State Power Conversion Conference (Powercon 5), pp. A3.1-A3.16, May 1978.

[7] Slobodan Ćuk and R. D. Middlebrook, "A New Optimum Topology Switching Dc-to-Dc Converter," IEEE Power Electronics Specialists Conference, 1977 Record, pp. 160-179 (IEEE Publication 77CH 1213-8 AES).

[8] Slobodan Ćuk, "Discontinuous Inductor Current Mode in the Optimum Topology Switching Converter," IEEE Power Electronics Specialists Conference, 1978 Record, pp. 105-123 (IEEE Publication 78CH1337-5 AES).

[9] Slobodan Ćuk and Robert W. Erickson, "A Conceptually New High-Frequency Switched-Mode Amplifier Technique Eliminates Current Ripple," Proc. Fifth National Solid-State Power Conversion Conference (Powercon 5), pp. G3.1-G3.22, May 1978.

[10] R. D. Middlebrook, "Modelling and Design of the Ćuk Converter," Proc. Sixth National Solid-State Power Conversion Conference (Powercon 6), pp. G3.1-G3.14, May 1979.

[11] Loman Rensink, Art Brown, Shi-Ping Hsu, and Slobodan Ćuk, "Design of a Kilowatt Off-Line Switcher Using a Ćuk Converter," Proc. Sixth National Solid-State Power Conversion Conference (Powercon 6), pp. H3.1-H3.26, May 1979.

[12] Shi-Ping Hsu, Art Brown, Loman Rensink, and R. D. Middlebrook, "Modelling and Analysis of Switching Dc-to-Dc Converters in Constant-Frequency Current-Programmed Mode," IEEE Power Electronics Specialists Conference, 1979 Record.

[13] D. M. Wiberg, State Space & Linear Systems, Schaum's outline series, McGraw-Hill, 1971.

[14] Slobodan Ćuk, "Switching Dc-to-Dc Converter with Zero Input or Output Current Ripple," IEEE Industry Applications Society Annual Meeting, 1978 Record, pp. 1131-1146,(IEEE Publication 78CH1346-6IA).

[15] M. Clique, A. J. Fossard, "Design of Feedback Laws for DC-DC Converters Using Modern Control Theory," IEEE Power Electronics Specialists Conference, 1978 Record, pp. 2-11 (IEEE Publication 78CH1337-5 AES).

[16] A. G. Ganz, "A Simple, Exact Equivalent Circuit for the Three-Winding Transformer", IRE Transactions on Component Parts, CP-9 #4, Dec. 1962, pp. 212-213.

[17] M.I.T. Staff, Magnetic Circuits and Transformers, The M.I.T. Press, 1943.

[18] Loman Rensink, "Switching Regulator Configurations and Circuit Realizations," Ph.D. thesis, California Institute of Technology, Pasadena, California, 1980.

[19] R. D. Middlebrook and Slobodan Ćuk, "Isolation and Multiple Output Extensions of a New Optimum Topology Switching Dc-to-Dc Converter," IEEE Power Electronics Specialists Conference, 1978 Record, pp. 256-264 (IEEE Publication 78CH1337-5 AES).